FEDERAL UNIVERSITY OF UBERLÂNDIA
School of Chemical Engineering
Graduate Program in Chemical Engineering

Evaluation of fluid rheology and pore space characteristics in the inner and external cake formation in overbalanced drilling operations

Nara Brandão Costa Santos

Uberlândia - MG

2021

FEDERAL UNIVERSITY OF UBERLÂNDIA
School of Chemical Engineering
Graduate Program in Chemical Engineering

Evaluation of fluid rheology and pore space characteristics in the inner and external cake formation in overbalanced drilling operations

Nara Brandão Costa Santos

Advisor: João Jorge Ribeiro Damasceno

Co-advisor: Fábio de Oliveira Arouca

Doctoral exam presented to the Graduate Program in Chemical Engineering at the Federal University of Uberlândia in partial fulfillment of the requirements for the degree of Doctor in Chemical Engineering.

Uberlândia – MG

2021

Dados Internacionais de Catalogação na Publicação (CIP)
Sistema de Bibliotecas da UFU, MG, Brasil.

S237e
2021

Santos, Nara Brandão Costa, 1987-
Evaluation of fluid rheology and pore space characteristics in the inner and external cake formation in overbalanced drilling operations [recurso eletrônico] / Nara Brandão Costa Santos. - 2021.

Orientador: João Jorge Ribeiro Damasceno.
Coorientador: Fábio de Oliveira Arouca.
Tese (Doutorado) - Universidade Federal de Uberlândia, Programa de Pós-Graduação em Química.
Modo de acesso: Internet.
Disponível em: http://doi.org/10.14393/ufu.te.2021.5549
Inclui bibliografia.

1. Química. I. Damasceno, João Jorge Ribeiro, 1957-, (Orient.). II. Arouca, Fábio de Oliveira, 1977-, (Coorient.). III. Universidade Federal de Uberlândia. Programa de Pós-Graduação em Química. IV. Título.

CDU: 54

Glória Aparecida
Bibliotecária - CRB-6/2047

UNIVERSIDADE FEDERAL DE UBERLÂNDIA
Coordenação do Programa de Pós-Graduação em Engenharia Química
Av. João Naves de Ávila, 2121, Bloco 1K, Sala 206 - Bairro Santa Mônica, Uberlândia-MG, CEP 38400-902
Telefone: (34)3239-4249 - www.ppgeq.feq.ufu.br - secppgeq@feq.ufu.br

ATA DE DEFESA - PÓS-GRADUAÇÃO

Programa de Pós-Graduação em:	Engenharia Química				
Defesa de:	Tese de Doutorado, 04/2021 PPGEQ				
Data:	27 de agosto de 2021	Hora de início:	9:00	Hora de encerramento:	11:45
Matrícula do Discente:	11713EQU004				
Nome do Discente:	Nara Brandão Costa Santos				
Título do Trabalho:	Evaluation of fluid rheology and pore space characteristics in the inner and external cake formation in overbalanced drilling operations.				
Área de concentração:	Desenvolvimento de processos químicos				
Linha de pesquisa:	Processos de Separação				
Projeto de Pesquisa de vinculação:	Otimização da separação sólido-líquido na perfuração de poços de petróleo e gás e modelagem e simulação numérica de escoamentos de fluidos em seções anulares				

Reuniu-se por meio de webconferência, a Banca Examinadora, designada pelo Colegiado do Programa de Pós-graduação em Engenharia Química, assim composta: Professores Doutores: Bruno Arantes Moreira - FAEN/UFGD; Eduardo Hiromitsu Tanabe - DEQ/UFSM; Fran Sérgio Lobato - FEQUI/UFU; Claudio Roberto Duarte - PPGEQ/UFU; Fábio de Oliveira Arouca - PPGEQ/UFU, coorientador e João Jorge Ribeiro Damasceno - PPGEQ/UFU, orientador da candidata.

Iniciando os trabalhos o presidente da mesa, Prof. Dr. João Jorge Ribeiro Damasceno, apresentou a Comissão Examinadora e a candidata, agradeceu a presença do público, e concedeu à Discente a palavra para a exposição do seu trabalho. A duração da apresentação da Discente e o tempo de arguição e resposta foram conforme as normas do Programa.

A seguir o senhor(a) presidente concedeu a palavra, pela ordem sucessivamente, aos(às) examinadores(as), que passaram a arguir o(a) candidato(a). Ultimada a arguição, que se desenvolveu dentro dos termos regimentais, a Banca, em sessão secreta, atribuiu o resultado final, considerando o(a) candidato(a):

aprovada.

Esta defesa faz parte dos requisitos necessários à obtenção do título de Doutor.

O competente diploma será expedido após cumprimento dos demais requisitos, conforme as normas do Programa, a legislação pertinente e a regulamentação interna da UFU.

Nada mais havendo a tratar foram encerrados os trabalhos. Foi lavrada a presente ata que após lida e achada conforme foi assinada pela Banca Examinadora.

Documento assinado eletronicamente por **João Jorge Ribeiro Damasceno**, **Professor(a) do Magistério Superior**, em 27/08/2021, às 11:53, conforme horário oficial de Brasília, com fundamento no art. 6º, § 1º, do Decreto nº 8.539, de 8 de outubro de 2015.

Documento assinado eletronicamente por **Fabio de Oliveira Arouca**, **Professor(a) do Magistério Superior**, em 27/08/2021, às 11:54, conforme horário oficial de Brasília, com fundamento no art. 6º, § 1º, do Decreto nº 8.539, de 8 de outubro de 2015.

Documento assinado eletronicamente por **Claudio Roberto Duarte**, **Professor(a) do Magistério Superior**, em 27/08/2021, às 11:54, conforme horário oficial de Brasília, com fundamento no art. 6º, § 1º, do Decreto nº 8.539, de 8 de outubro de 2015.

Documento assinado eletronicamente por **Fran Sergio Lobato**, **Professor(a) do Magistério Superior**, em 27/08/2021, às 11:55, conforme horário oficial de Brasília, com fundamento no art. 6º, § 1º, do Decreto nº 8.539, de 8 de outubro de 2015.

Documento assinado eletronicamente por **Bruno Arantes Moreira**, **Usuário Externo**, em 27/08/2021, às 11:55, conforme horário oficial de Brasília, com fundamento no art. 6º, § 1º, do Decreto nº 8.539, de 8 de outubro de 2015.

Documento assinado eletronicamente por **Eduardo Hiromitsu Tanabe**, **Usuário Externo**, em 27/08/2021, às 11:58, conforme horário oficial de Brasília, com fundamento no art. 6º, § 1º, do Decreto nº 8.539, de 8 de outubro de 2015.

A autenticidade deste documento pode ser conferida no site https://www.sei.ufu.br/sei/controlador_externo.php?acao=documento_conferir&id_orgao_acesso_externo=0, informando o código verificador **3005144** e o código CRC **D4A6EC7D**.

Acknowledgments

I would like to thank God and my guardian angel for guiding and lighting my paths.

I would like to thank my family and friends for supporting my decisions and always being kind to me.

I would like to thank Professors Damasceno and Fábio for the opportunity for me to be a team member of LabSep and for their teachings.

I would like to thank Dr. Masoud for the opportunity for me to be a visiting scholar at KU.

I would like to thank Arsalan for his attention, dedication to my learning, and introduction to the porous media community.

I would like to thank the undergraduate and graduate students in the laboratory for their effort to help me with the experimental stage and daily time. A special thank you to Flávia.

I would like to thank the Professors of the committee members, Fran Sérgio, Cláudio Duarte, Bruno Moreira, and Eduardo Tanabe, for providing valuable suggestions. I appreciate the help and attention of Professor Fran Sérgio in the numerical optimization stage.

I would like to thank the members of the Chemical Engineering Department from UFU and the Chemical and Petroleum Engineering Department from KU.

I would like to thank CapesPrInt (Brazil) and UFU/CapesPrInt (Brazil) (88881.311515/2018-01) for the financial grant of the exchange Program. Capes (Brazil), CNPq (Brazil), Fapemig (Brazil), Petrobras (Brazil), Chemical Engineering Department FEQ/UFU (Brazil) for the financial support, and American Chemical Society Petroleum Research Fund (ACS PRF#59089-DNI9) for partially supporting this research.

“Ad astra per aspera”

To my mother Rosana, my father Sérgio, and my brother Vitor.

Table of contents

Figures

Tables

Nomenclature

A	cross-sectional filter area	$M^0L^2T^0$
c	Ergun coefficient	$M^0L^0T^0$
C	mass concentration of solid	$M^0L^0T^0$
d_p	diameter of the pore	$M^0L^1T^0$
d'_p	diameter of the particle in the RRB model	$M^0L^1T^0$
$d_{0.632}$	cutting diameter in the RRB model	$M^0L^1T^0$
g	gravitational force	$M^0L^1T^{-2}$
I	identity tensor	$M^0L^0T^0$
I'	X-ray beam after passing through the sample	$M^0L^2T^0$
I'_0	X-ray beam before passing through the sample	$M^0L^2T^0$
K	permeability	$M^0L^2T^0$
K_c	cake permeability	$M^0L^2T^0$
K_m	medium permeability	$M^0L^2T^0$
l_c	cake thickness	$M^0L^1T^0$
l_m	medium length	$M^0L^1T^0$
m	consistency index of the power-law rheological model	$M^1L^1T^n$
m'	resistive force	$M^1L^1T^{-2}$
m^*	total resistive force	$M^1L^1T^{-2}$
M	mass of solids in the cake	$M^1L^0T^0$
n	behavior index of the power-law rheological model	$M^0L^0T^0$
n'	parameter in RRB model	$M^0L^0T^0$
P_c	capillary pressure	$M^1L^{-1}T^{-2}$
q	superficial velocity	$M^0L^1T^{-1}$
Re_i	interstitial Reynolds number	$M^0L^0T^0$
Re_{gen}	generalized Reynolds number	$M^0L^0T^0$
Re_k	modified Reynolds number	$M^0L^0T^0$
R_m	filter medium resistance	$M^0L^{-1}T^0$
r	capillary radius	$M^0L^1T^0$
S	saturation	$M^0L^0T^0$
t	time	$M^0L^0T^1$
t'	structural factor of the porous media	$M^0L^0T^0$
T	tension tensor that acts in the fluid phase	$M^0L^0T^0$
$T^{"}$	constitutive part of the tensor	$M^1L^{-1}T^{-2}$
u	interstitial velocity	$M^0L^1T^{-1}$
V	filtrate volume	$M^0L^3T^0$
X	cumulative fraction of solids in RRB model	$L^0M^0T^0$
α	specific cake resistance	$M^{-1}L^1T^0$
β	non-Darcy flow coefficient	$M^0L^{-1}T^0$
ΔP	pressure drop	$M^1L^1T^{-2}$
ε	medium porosity	$M^0L^0T^0$
ε_c	cake porosity	$M^0L^0T^0$
μ	fluid viscosity	$M^0L^{-1}T^{-3}$

μ_{ap}	apparent viscosity	$M^0L^{-1}T^{-3}$
μ'	local linear attenuation coefficient	$M^0L^{-1}T^0$
ρ	specific mass of the fluid	$M^1L^{-3}T^0$
p_{fil}	specific mass of the filtrate	$M^1L^{-3}T^0$
ρ_s	specific mass of the solid	$M^1L^{-3}T^0$
σ	interfacial tension	$M^1L^0T^{-2}$
γ	shear rate	$M^0L^0T^{-1}$
γ^*	distension rate	$M^0L^0T^{-1}$
τ	shear stress	$M^1L^1T^{-2}$

$CaCO_3$	Calcium Carbonate
CO_2	Carbon Dioxide
N_2	Nitrogen
OF	objective function
XG	Xanthan Gum

ABSTRACT: The increase in energy demand has been improving the extraction techniques of energy resources. In the oil industry, understanding the behavior of drilling fluids in the inner and external cake formation and the inner cake displacement during flow back (i.e., oil extraction) is important because these situations may impact formation damage and, subsequently, cause financial and environmental risks. To address this issue, this Study investigated the effect of fluid rheology and pore space characteristics in the formation of filtered cake in overbalanced drilling operations. Study 1A aimed to evaluate the change in the media permeability by polymer retention and the effect of viscous and inertial forces during polymer flow. The flow of xanthan gum (XG) 0.2 and 0.4% (m/m) through 50 and 120 μm ceramic filters was analyzed as a function of pressure drop by high-temperature, high-pressure (HTHP) filter press. Study 1B aimed to evaluate the properties of external cakes and the change in the medium permeability by polymer retention and the clogging of pores by small solid particles. Suspensions of calcium carbonate ($CaCO_3$) 5% (v/v) in XG solutions were filtered, similar to Study 1A, and a model to estimate the medium and the external cake permeabilities was proposed. Study 2A aimed to analyze inner cake formation and its displacement by mineral oil at pore levels. XG 0.2 and 0.4% (m/m) was injected through miniature carbonate core plugs, followed by oil injections at different flow rates and pore fluid occupancy imaging using a Heliscan micro-CT system. Study 2A also proposed a novel methodology to eliminate the partial volume effect and to account for the porosity from micropores. Study 2B aimed to investigate the impact of the initial saturation of the core in the formation of inner filter cakes. XG 0.2 % (m/m) was injected through similar carbonate cores as in Study 2A with different wetting and non-wetting saturations. Then the pore fluid occupancy and phase saturation were imaged using the same experimental apparatus of Study 2A. The main findings show that Darcy's law best characterized the XG flow in Study 1A. Polymer retention was noticed by the decrease in the medium permeability and the filtrate consistency index. As the pressure drop increased, the difference in the permeability of the media shortened as a function of pressure. In Study 1B, the medium and cake permeabilities decreased as the pressured drop increased. The cakes presented compressibility, and the ones formed by XG 0.4% (m/m) showed higher permeability and porosity values. The suspension filtrate presented lower values of consistency index and higher values of behavior index than the suspension before filtration. In Study 2A, the number of pores occupied by XG in the centers decreased, and the oil resided in the large and intermediate regions while cycles of oil injections were performed. Polymer retention was observed in the inlet face of cores 1 and 2. The well-connected pore space influenced the fluid phase mobility in both cores. While the fluid flow was favored in core 1, it was hindered in core 2. In Study 2B, higher initial wetting saturation favored an increase in XG saturation after its injection. The invaded XG disconnected most of the previous oil clusters that became trapped in the pore space. So, the studies presented in this thesis intend to expand further the knowledge of rock-fluid interaction and the formation of filter cakes during overbalanced drilling operations to minimize formation damage by fluid loss.

Keywords: xanthan gum flow; porous media; permeability; filter cake; HTHP filter press; micro-CT.

RESUMO: O aumento da demanda energética tem impulsionado a melhoria das técnicas de extração dos recursos energéticos. Na indústria petrolífera, o entendimento do comportamento dos fluidos de perfuração na formação das tortas interna e externa de filtração e o posterior deslocamento da torta interna durante a extração do óleo é importante pois essas ocorrências impactam a avaliação dos danos à formação e, consequentemente, os riscos financeiros e ambientais da perfuração. Para isso, investigou-se o efeito da reologia do fluido e das características do meio poroso na formação de tortas em operações de perfuração do tipo *overbalanced*. No Estudo 1A objetivou-se avaliar a alteração a permeabilidade de meios porosos devido a retenção polimérica, e os efeitos das forças inerciais e viscosas durante o escoamento polimérico. Os escoamentos de Goma Xantana (GX) 0,2 e 0,4% (m/m) através de meios porosos de 50 e 120 μm foram analisados em função da queda de pressão em filtro de elevada pressão e temperatura (HTHP). No Estudo 1B objetivou-se avaliar as propriedades das tortas externas e a alteração da permeabilidade dos meios porosos devido à retenção polimérica e ao entupimento dos poros por sólidos finos. Suspensões de Carbonato de Cálcio ($CaCO_3$) 5% (v/v) em soluções de GX foram filtradas em testes similares ao Estudo 1A e um modelo para estimar as permeabilidades da torta externa e do meio poroso após a filtração foi proposto. No Estudo 2A objetivou-se analisar a formação da torta interna de filtração e seu posterior deslocamento por óleo mineral em escala de poro. GX 0,2 e 0,4% (m/m) foram injetadas em pequenas amostras de rocha carbonática, seguidas pela injeção de diferentes vazões volumétricas de óleo e pelo imageamento da ocupação dos poros pelos fluidos utilizando o sistema Heliscan de micro-CT. Além disso, novas metodologias para eliminar o efeito de volume parcial e contabilizar a porosidade proveniente dos micro poros foram apresentadas. No Estudo 2B objetivou-se investigar o impacto da saturação inicial da rocha na formação da torta interna de filtração. GX 0,2% (m/m) foi injetada em amostra carbonática com diferentes saturações iniciais de fases molhável e não-molhável, e o imageamento da ocupação dos poros e da saturação das fases foi similar ao Estudo 2A. Os resultados do Estudo 1A mostraram que o escoamento de GX foi melhor descrito pela Lei de Darcy. A retenção polimérica foi evidenciada pelo decréscimo da permeabilidade dos meios porosos e do índice de consistência do filtrado. A diferença entre as permeabilidades dos meios foi diminuída em condições de elevada pressão. No Estudo 1B as permeabilidades da torta e dos meios porosos diminuíram com o aumento da queda de pressão. As tortas apresentaram compressibilidade e as formadas pelas suspensões de GX 0,4% (m/m) apresentaram os maiores valores de permeabilidade e porosidade. O filtrado das suspensões apresentaram menores valores de índice de consistência e maiores valores de índice de comportamento em relação às suspensões antes da filtração. No Estudo 2A o número de poros ocupados por GX no centro diminuiu e o óleo ocupou regiões de tamanhos maiores e intermediários à medida em que foi injetado. Retenção polimérica foi observada na região de injeção do fluido nas amostras 1 e 2. A conectividade do espaço poroso influenciou a mobilidade da fase fluida em ambas as amostras rochosas. O escoamento dos fluidos foi favorecido na amostra 1 e dificultado na 2. No Estudo 2B, elevadas saturações da fase molhável favoreceram o aumento da saturação de GX após a injeção polimérica. A invasão de GX ocasionou a desconexão dos *clusters* de óleo que ficaram trapeados no meio poroso. Dessa forma, os estudos apresentados nessa tese pretendem ampliar o conhecimento sobre a interação rocha-fluido e a formação das tortas de filtração durante as perfurações *overbalanced* para minimizar o dano as formações devido a perda de filtrado.

Palavras chave: escoamento de Goma Xantana; meios porosos; permeabilidade; torta de filtração; filtração HTHP; micro-CT

1. Introduction

The growing energy demand has been driving the discovery and improvement of the extraction of energy resources. Most of the world and Brazilian energy matrix is composed of non-renewable resources, with oil being its main component (International Energy Agency, 2020). In the Brazilian scenario, the pre-salt fields store large and potential oil reservoirs with good growth perspectives (Goldemberg et al., 2014). In this context, ensuring the assertiveness and efficiency of drilling projects play an important role in supporting long-term investment decisions in oil exploration.

In the oil industry, drilling a well is an expensive financial step. At this stage, formation damage might occur, and it is one of the most relevant factors that should be addressed and mitigated (Muñoz, García-Verdugo, and San-Martín, 2015; Goldemberg et al., 2014). Formation damage refers to the impairment of the reservoir by adverse processes, like the seepage of drilling mud into the rock around the well (Shamsi, Norouzi-Apourvai, and Jafari, 2019; Zhao et al., 2019; Civan, 2007). Mitigating formation damage reduces the economic costs and environmental impacts of drilling operations. For that, one should investigate how formation damage happens during a drilling operation and, later, how it interacts with the reservoir fluid once the well is put back under production. In this study, the former question deals with fluid loss and the subsequent formation and arrangement of the inner and external filter cakes.

The drilling fluid pressure is set above the reservoir pore pressure in an overbalanced drilling operation, resulting in external and inner filter cakes. If the drilling cuttings and sealing agents are larger than the reservoir pores, they accumulate on the wellbore surface, building the external cake. Otherwise, they migrate through the reservoir pores, and with the mud filtrate, they form the inner filter cake. The created cake controls fluid loss, reducing the contamination of reservoir fluids and pore-level blockage of the fluid pathways during production (Civan, 2007; Asme, 2005). Figure 1.1 illustrates an overbalanced drilling operation and the inner and external filter cakes.

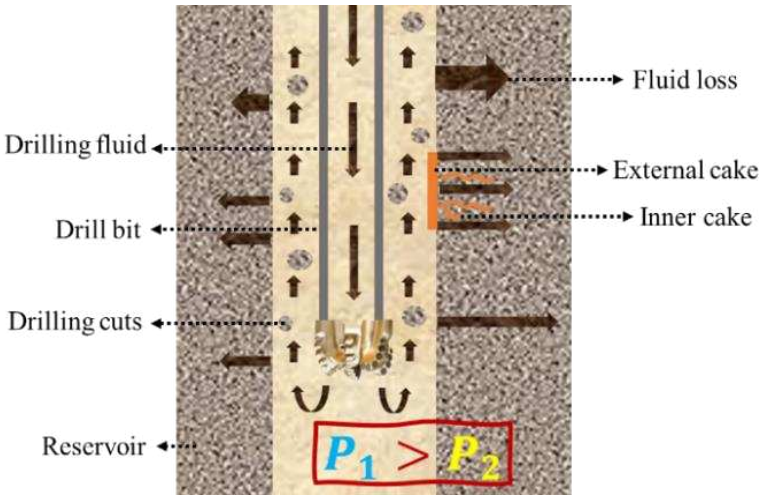

Figure 1.1: Schematic illustration of an overbalanced drilling operation (P1>P2) and the formation of inner and external cakes.

The interplay of the rock-fluid controls the formation and removal of the cakes. Petrophysical properties like porosity, permeability, pore size, connected porosity, and wettability can be mentioned on the rock side. On the fluid side, in turn, its rheological behavior under high shear rate, pressure, temperature, polymer retention on the rock surface, and particle size distribution of its solids can be highlighted (Ramézani et al., 2015; Petri and Queiroz, 2010; Sochi, 2010; Liu and Civan, 1995).

The fluid loss control includes not only controlling the filtrate volume per area and time. The quality of the resulting filter cake in the wellbore is also an important parameter to be evaluated. Thin mud cakes with low permeability usually strengthen the wellbore. However, thick mud cakes can cause operational problems like high torque and drag. Several studies have been evaluating the cake properties such as thickness, compressibility, lubricity, and particle size distribution (Salehi et al., 2015; Chesser et al., 1994). Core flooding experiments are one of the most applied experimental methodologies to track the fluid flow through a porous structure. On a macro scale, High Temperature, High Pressure (HTHP) filter press has been used to reproduce overbalanced conditions and cake formation (Ramézani et al., 2015; Ferraz, 2014; Oliveira Junior, 2014; Calabrez, 2013).

The invasion of mud filtrate also impacts the measurement of reliable data from boreholes such as fluid saturation, porosity, and formation pressure. It is because most of the borehole measurements are performed during the drilling stage (Schroeder and Torres-Verdín, 2019; Dandekar, 2013). The depth of the inner cake can be represented by a polymer front propagation that allocates in the reservoir pores. Polymer adsorption, mechanical entrapment, and hydrodynamic retention are three main polymer retention mechanisms that affect the physical interaction between the polymer molecules and solid surface (Agi et al., 2018; Manichand and Seright, 2014; and Sorbie, 1991).

At pore levels, the non-destructive technique of X-ray micro-computed tomography (X-ray micro-CT) has been used for three-dimensional (3D) visualization of pore space and fluid occupancies at different saturations. Schroeder and Torres-Verdín (2019) visualized and quantified the spatial and temporal distributions of the radial flow of water and synthetic oil-based filtrate and filter cake thickness in sandstone cores. Khishvand et al. (2016) investigated the residual oil saturation in sandstone and carbonate rock samples using unsteady-state drainage and imbibition flow cycles by changing brine flow rates. Drainage occurs when the non-wetting phase displaces the wetting phase, and imbibition corresponds to the opposite displacement mechanism (Blunt, 2017).

Despite the vast publication about the formation of drilling cakes and fluid flow through porous media, to the best of our knowledge, there is still a gap regarding the qualitative and quantitative experimental analyses of displacement imaging of non-Newtonian fluid flow and estimation of external cake permeability as a function of pressure drop and polymer retention. Most studies have used simple porous media customized in the laboratory to perform flow tests, which may simplify

the real complexity of a reservoir structure. Others have used Newtonian solutions instead of non-Newtonian ones, like real mud composition. Other studies have performed tests within narrow pressure ranges, limiting the pressure range in relation to the field. Thus, to overcome these restrictions, this study used non-Newtonian solutions and suspensions flowing through both real cores and accurately customized ones considering a wide range of pressure drops.

1.1 Research aim

This thesis aimed to investigate the effect of fluid rheology and pore space characteristics on inner and external cake formation. To address this issue, it was first designed two approaches, Studies 1 and 2, which evaluated the fluid flow from a macro and pore-scale perspective, respectively. Each study was subdivided into A and B to focus on specific research topics.

Study 1A focused on changing medium permeability using different polymer solutions and the balance between viscous and inertial forces during the flow. Study 1B focused on the flow of polymer suspensions and their impact on changing medium permeability. Also, Study 1B estimated the permeability of the external cake as a function of flow pressure, suspension rheology, and pore space structure. Study 2A focused on the formation of inner cake by polymer solutions and its potential rearrangements during backflow at pore levels. Study 2B focused on the formation of inner cake as a function of the initial saturation condition of the pore space.

1.1.1 Research objective

Study 1A: flow of xanthan gum (XG) solutions of 0.2 and 0.4% mass/mass (m/m) polymer concentration through porous ceramic filters of 50 and 120 μm average pore size under different pressure drops using HTHP filter press;

Study 1B: flow of suspensions of calcium carbonate ($CaCO_3$) 5% volume/volume (v/v) in solutions of XG 0.2 and 0.4% (m/m) polymer concentration through porous ceramic filters of 50 and 120 μm under different pressure drops using HTHP filter press;

Studies 1A and 1B: characterization of the rheological properties of both the solution and suspension before and after the filtering stage using a viscosimeter;

Study 2A: flow of XG solutions of 0.2 and 0.4% (m/m) polymer concentration through miniature carbonate core plugs with different characteristics, then flow of different mineral oil flow rates using a fluid pumping system;

Study 2B: flow of XG solutions of 0.2% (m/m) polymer concentration through miniature carbonate core plugs with different characteristics and different initial saturation conditions using a fluid pumping system;

Studies 2A and 2B: imaging of pore fluid occupancy using a Heliscan micro-CT system to analyze polymer and oil saturation profiles, and mapping of pore fluid occupancy, cluster, and

globule size distributions and phase connectivity as a function of non-wetting and wetting flow rate in drainage and imbibition displacements, respectively.

Finally, this thesis is structured in the following chapters: chapter 2 presents a literature review of the fundamental concepts and the previously published research on the topic of this study. Chapter 3 presents the novel experimental methodologies and setups for polymer preparation, pore media characterization, core flow tests, and image analysis workflow. The results are reported and discussed in chapter 4. Chapter 5 highlights the conclusions of the main findings and provides some insights for future research.

2. Literature review

This chapter introduces a literature review of the fundamental concepts and the recent studies about the main topics of this thesis. First, it presents an overview of drilling operations and rock and drilling fluid properties. Next, inner and external cake formations, polymer retention, and the mathematical approach for fluid flow through porous media are discussed. In the end, a brief description of X-ray micro-computed tomography and its application in geoscience is presented.

2.1 Drilling operation

In the drilling operations of an oil well, the rocks are drilled due to the rotation and weight applied to the drill bit located at the end of the drilling column. A drilling fluid is injected inside the drill bit and returns to the surface through the annular, carrying the drilled solids. Besides this application, and among others, the drilling fluid provides hydrostatic pressure on the formations and stabilizes the walls of the well (Thomas, 2001).

The formation pressure and the monitoring of the operational window are key factors during the drilling stage. They ensure a safe and efficient operation. The knowledge of the formation pressure allows a high penetration rate, determination of the linings depth of the settlement, and time and cost reduction (Li, George, and Purdy, 2012; Thomas, 2001). The monitoring of the operational window, in turn, determines the variation allowed for the specific mass of drilling fluids and, consequently, the pressure on the walls of the well to maintain their stability (Ferreira, 2010).

Two types of operational limits are defined: the upper and the lower. The upper limit of the operational window is the curve of the fracture gradient. It limits the maximum specific mass of the drilling fluid. Excess fluid weight can generate tensile stresses in the rock, causing hydraulic fractures, loss of fluid, and even loss of circulation, i.e., total loss of drilling fluid (Li, George, and Purdy, 2012; Ferreira, 2010). The lower limit corresponds to the pore pressure curve. It limits the minimum specific gravity of the drilling fluid. The weight of the fluid below the pore pressure can cause an inflow of fluid from the reservoir to the well. If the influx is controllable, there is a kick; if it is uncontrollable, there is a blowout (Li, George, and Purdy, 2012; Ferreira, 2010; Thomas, 2001).

Thus, depending on the pressure gradient between the drilling fluid and the reservoir, three operational scenarios can be established: (i) an underbalanced process when the gradient is negative, (ii) a near balanced process when the gradient is zero, or (iii) an overbalanced processes when the gradient is positive. Most drilling operation processes occur in overbalanced conditions, with around 100 to 500 psi (Azar and Samuel, 2007).

2.1.1 Reservoir rock properties

The petrophysical properties of reservoir rocks enable evaluating the most appropriate drilling techniques to achieve the highest productivity. Sandstones and carbonates are the largest oil and

gas reservoirs. Sandstones are the most frequent type of reservoir rock. They are found in thick layers, have an average porosity of 10 to 20%, and are brittle and subject to cracking. Carbonate rocks, in turn, are limestones, dolomites, and the intermediates between those. They have greater porosity than sandstones, resulting in high permeability (Rosa, Carvalho, and Xavier, 2006).

Here it is presented the fundamental rock properties like porosity, permeability, wettability, and saturation usually estimated in the drilling operations.

✓ Porosity

Porosity, ε, is a static property of the ratio between the void volume and the total volume of the rock. It is expressed by Equation 2.1 (Dandekar, 2013):

$$\varepsilon = \frac{pore\ volume}{total\ volume} \tag{2.1}$$

Three different types of pores might be present in a porous medium. The interconnected pores are pores interconnected with others, forming a pore network and enabling fluid mobility. The dead-end pores are pores connected with other void spaces but with a dead-end, trapping the fluid. The isolated or closed pores are completely isolated or closed pores from other void spaces due to cementation. They are inaccessible and remain fully saturated with the fluid from the formation (Dandekar, 2013). Figure 2.1 illustrates a conceptual representation of pore space with the three types of pores.

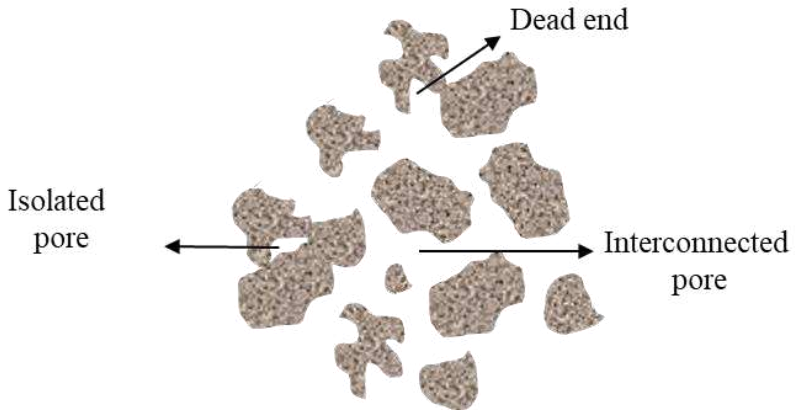

Figure 2.1: Representation of interconnected, dead-end, and isolated pores in a pore space (based on Dandekar, 2013).

Based on the type of pores, absolute, effective, and ineffective porosity can be defined. Absolute porosity is the ratio between the volume of interconnected, dead-end, and isolated pores to the total volume of the rock. The effective porosity is related to the volume of interconnected and dead-end pores to the total volume of the rock. This latter represents the maximum volume of fluid extracted from the reservoir, i.e., the space occupied by fluids that can move through the pore space. Lastly, ineffective porosity is the ratio of the volume of isolated pores to the total volume (Dandekar, 2013; Rosa, Carvalho, and Xavier, 2006).

The reservoir rock is composed of grains connected by cement and matrix materials. Thus, the total volume of the reservoir corresponds to the volume of solid materials (grain, cement, and matrix) and the empty spaces between them. The shape, arrangement, packing, and size of the grains also affect the porosity (Thomas, 2001).

✓ Permeability

Permeability, K, is a flow property of the medium as it relates the fluid flow to its viscosity and pressure drop. It characterizes the ability of a rock to allow the fluid to flow through the pore space, as is shown in Figure 2.2. It is a tensorial property and usually exhibits anisotropy caused by rock heterogeneity (Schön, 2011).

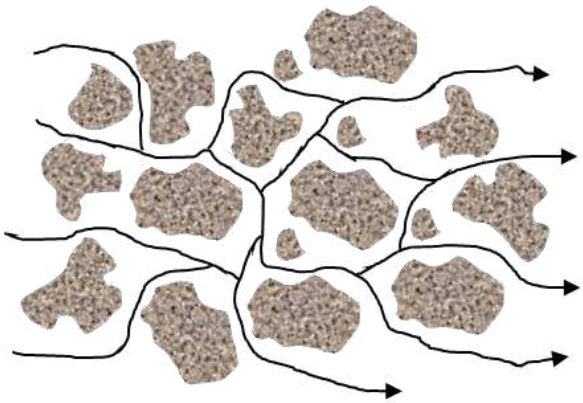

Figure 2.2: Conception of permeability of a porous medium (based on Dandekar, 2013).

Large and connected pores offer less resistance to fluid flow, increasing the porous medium permeability. Besides, natural or artificial fractures increase or create permeability for fluids. Although the fractures do not change the permeability of the matrix pores, they change the permeability of the overall flow network. In contrast, the more tortuous, narrow, and strangled the porous channels, the lower the medium permeability (Dandekar, 2013; Schön, 2011; Sochi, 2010;).

The permeability can be categorized into three types: (i) absolute, (ii) effective, and (iii) relative. The absolute permeability is defined when only a single fluid phase saturates the porous medium. As it is a porous medium property, it does not depend on the fluid that saturates it. Effective permeability is related to the flow of one fluid in the presence of another fluid when they are immiscible. It depends on the saturation of each fluid in the pore space. The relative permeability is the ratio of effective and absolute permeabilities (Dandekar, 2013; Schön, 2011; Thomas, 2010; Rosa, Carvalho, and Xavier, 2006).

Permeability has an area unit, explaining it as a pore geometrical measure (Schön, 2011). Several permeability models have been reported in the literature to estimate the permeability values, as is shown later in this chapter.

✓ Wettability

Wettability is the property for one fluid to adhere (coat) a rock surface in the presence of another immiscible fluid spontaneously. It can also be referred to as the distribution of contact angles, θ, throughout the pore-space and it is related to interfacial tension, σ, by Equation 2.2 (Blunt, 2017; Schön, 2011):

$$cos\theta = \frac{\sigma_{s1} - \sigma_{s2}}{\sigma_{21}} \qquad (2.2)$$

where σ_{s1} and σ_{s2} are the interfacial tensions between the solid and fluid 1 and 2, respectively; and σ_{21} is the interfacial tension between fluids 1 and 2.

Figure 2.3 illustrates the above concepts:

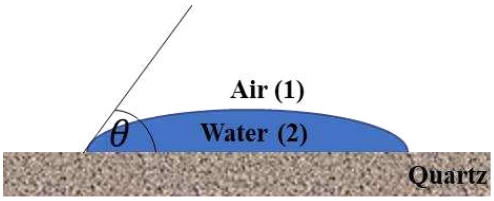

Figure 2.3: Contact angle and interfacial terms (modified from Schön, 2011).

The wettability type controls the fluid distribution in the pore space. The surface of a water-wet rock tends to be coated with water, while oil and gas occupy the center of the largest pores. The opposite occurs for oil-wet samples. In intermediate wettability, both oil and water adhere to the pore surface (Schön, 2011). Figure 2.4 shows the oil displacement in water and oil-wet surfaces during an imbibition process.

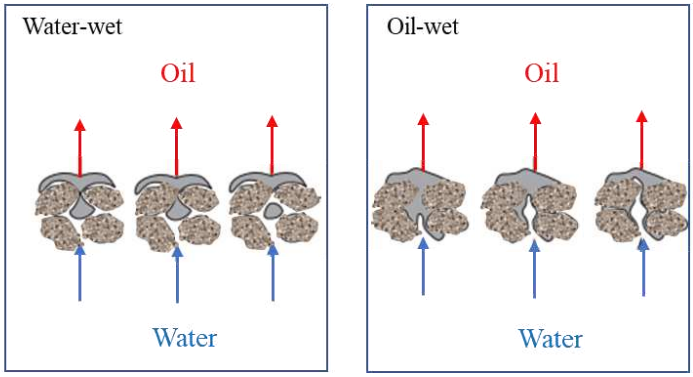

Figure 2.4: Oil displacement in water and oil-wet surfaces during imbibition (modified from Consentino, 2001).

✓ Saturation

Saturation, S, is the fraction of the porosity occupied by a given phase (oil, water, or gas), as Equation 2.3 expresses. It ranges from 0 to 1, and the summation of all phase saturation is 1 (Blunt, 2017).

$$S = \frac{total\ volume\ of\ fluid\ phase}{pore\ volume} \quad (2.3)$$

Three types of fluid saturations are important in the context of oil recovery: (i) critical gas saturation, (ii) residual oil saturation, and (iii) irreducible water saturation. The critical gas saturation corresponds to when the initial trapped gas in the hydrocarbon phase becomes continuous and flows. The residual oil saturation is the oil phase that remains in the pore space after displacement. The irreducible water saturation is the reaming and immobile water saturation in the pore space (Dandekar, 2013).

The invasion of mud filtrate and the removal of rock core sampling can affect the estimation of fluid saturation in the reservoir. It is because the filtrate of drilling fluids invades the formation pores, affecting the initial fluid saturation of the core sample. The process of removing the core, in turn, might lead the gas expansion and alteration in the fraction of each fluid in the medium (Dandekar, 2013).

Lastly, exemplifying the interplay among the above petrophysical properties, the larger and well-connected pores linked by large throats are the main porous structures contributing to bulk fluid flow (Sochi, 2010). This configuration results in a high permeable medium. Larger pores are also the firsts to be filled when a fluid is injected into the pore space. It is because they have low capillary pressure, P_c. This latter is defined as the pressure difference between the displacing and displaced fluids (wettability influence) and is given by Equation 2.4 (Blunt, 2017):

$$P_c = \frac{2\ \sigma\ cos\theta}{r} \quad (2.4)$$

where r is the capillary radius.

2.1.2 Drilling fluids

Drilling fluid (or mud) is a mixture of liquids, solids, chemical additives, and sometimes, gases used in the drilling stage. It can assume aspects of suspension, colloidal dispersion, or emulsion depending on the physical state of its components. Moreover, depending on the nature of the dispersing and dispersed phases, muds are classified as water, oil, air, or synthetic-based. This latter is the most used in the Brazilians' operations, especially the olefin-based in the salt layers of the Pres-salt formations (Petrobras, 2001; Thomas, 2001). Water-based fluids tend to present a larger diameter of mud infiltration invasion near the wellbore, followed by emulsions, and to a lower extent, the oil-based fluids (Schroeder and Torres-Verdín, 2019; Simpson, 1974).

The main functions of drilling fluids are the removal of cuttings and their transport to the surface, the controlling of the pressure of the rock formation, the maintenance of the mechanical and chemical stability of the wall of the well, the sealing of permeable formations, and the cooling and lubrication of the drill bit (Azar and Samuel, 2007; Asme, 2005).

The drilling fluids are formulated to increase the efficiency of the drilling operations according to the site that will be drilled. Usually, XG and $CaCO_3$ are present in the formulations as they play a key role in the formation of the filter cakes, increasing the stability of the drilling stage. XG is a biopolymer formed by structures of heteropolysaccharide and produced through bacterial fermentation of Xanthomonas campestris. Chemically, it has the main molecular chain formed by β-D-glucose structures in positions 1 and 4. It is non-toxic, biodegradable, and shows high stability over a wide range of pH and temperature (García-Ochoa et al., 2000). The high viscosity and the shear-thinning behavior of aqueous solutions of XG made them extensively used as a viscosifier and a fluid-loss controller. The $CaCO_3$ acts as a filling and thickening agent. It blocks the pores of the reservoir by forming the external filter cake, reducing fluid loss. It also increases the specific mass of the mud, favoring the control of hydrostatic pressure and the stability of the wall of the wells (Petrobras, 2011; Thomas, 2001).

2.1.2.1 Drilling fluid rheology

Drilling fluids are shear-thinning and time-dependent fluids, characterized by an apparent viscosity that decreases with increasing shear rate and with the time for which the fluid has been sheared. When the fluid is sheared at a constant rate, its apparent viscosity gradually decreases as the internal structure of the molecules is progressively broken down. As the number of structural linkages capable of being broken down decreases, the rate of change of the apparent viscosity with time also decreases (Chhabra and Richardson, 2008). These behaviors favor the transport of cutting to the surface during drilling and their suspension during operational stops, avoiding circulation loss and drill bit jamming (Skalle, 2011).

The power-law model is widely used to mathematically describe the shear-thinning behavior due to its simplicity and accuracy. It is given by Equation 2.5 and the apparent viscosity is given by Equation 2.6:

$$\tau = m\,\gamma^{n} \tag{2.5}$$

where τ is the shear stress, γ is the shear rate, and m and n are the empirical curve-fitting parameters known as the fluid consistency coefficient and the flow behavior index, respectively.

$$\mu_{ap} = m\,\gamma^{n-1} \tag{2.6}$$

2.2 Filter cake formation

A positive pressure gradient between the well and the reservoir is settled during overbalanced drilling operations. It avoids the uncontrollable migration of the fluid from the reservoir to the well, increasing operation safety, as already discussed. However, as the pressure of mud is settled above the reservoir pressure, there is a cross-flow filtration and, subsequently, a filter cake buildup over the face of the porous rock and filtrate invasion into the reservoir (Civan, 2007; Asme, 2005).

The filter cake formation consists of three stages. The first stage corresponds to the spurt loss. It is the initial filtration phase attributed to invasion and clogging of the porous medium by fine particles prior to filter cake formation. It is an initial jump in the cumulative volume of the filtrate that occurs in a short time. This initial nonlinear relationship of the filtrate volume and the squared root of time is mainly caused by some inertial flow in filtration at high flow rates and high overbalance pressure differences.

An inner filter cake is formed at the end of the spurt loss period. The filtrate and solids from the mud and cuttings smaller than the pore throat invade the reservoir pores in a pore volume filling event after the pore throat plugging. The external cake is formed by solids larger than the pore throat that accumulates on the reservoir wall and by finer particles that fill the interstices of the porous matrix formed by the larger particles (Dandekar, 2013; Civan, 2007; Asme, 2005). Figure 2.5 illustrates the spurt loss, inner and external filter cakes in an overbalanced operation.

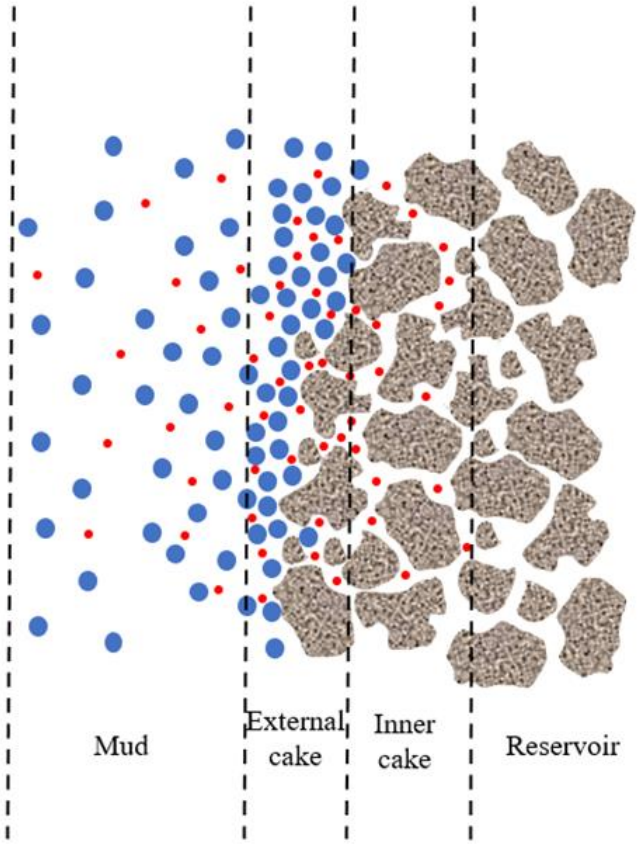

Figure 2.5: Formation of inner and external filter cake. The blue and red colors tag the larger and smaller particles, respectively.

Filter cakes can be formed by static and dynamic filtrations depending on the dynamic of fluid circulation. The characteristics of the cake like porosity, permeability, and thickness depend on the balance between the particle deposition and the cake erosion. Static filtration occurs when there

is no mud circulation. The solids are continuously deposited in the void spaces of the cake until they are filled. Thus, cake thickness increases continually, and the filtrate volume decreases with time. Once the cake is established, it controls the filtration rate, which is proportional to the square root of time.

In contrast, dynamic filtration occurs when the mud is being circulated. In this case, the cake grows to a point in which both the shear stress caused by the mud and the shear strength of the cake are balanced. It limits the cake thickness, and the rate of filtration after the cake formation is proportional to time. For a vertically oriented well, the solids deposition occurs radially as the fluid moves vertically (Civan, 2007; Asme, 2005, Waldmann, 2005).

Finally, the evaluation of the cake formation and its depth of invasion is important not only to control the fluid loss but also to ensure reservoir productivity. It is because formation damage might occur by pore blockage and wettability alteration due to chemical incompatibility between filtrate and the reservoir water (Fattah and Lashin, 2016; Salehi et al., 2015).

2.2.1 Inner filter cake

The inner cake formation is mainly formed by the mud filtrate and fine solids that migrate through the reservoir pores. This thesis analyzes the inner cake formation from macro and pore-scale perspectives by resembling the cake composition by polymer solutions. Thus, a brief discussion about non-Newtonian fluid flow through the porous medium is presented.

The polymer flow through a porous medium is governed by the interaction between the polymer properties (like polymer chain length and weight) and the rock characteristics (like pore and throat size distributions and aspect ratio). These interactions result in polymer retention in the porous structure, decreasing its permeability (Sorbie, 1991).

Three major retention mechanisms for polymer flood are widely reported in the literature: (i) polymer adsorption, (ii) mechanical entrapment, and (ii) hydrodynamic retention. Their descriptions are shown in sequence based on the studies of Agi et al. (2018), Manichand and Seright (2014), and Sorbie (1991). Polymer adsorption is physical adsorption controlled by hydrogen bond and van der Waal's forces between the rock surface and the polymer molecules. A bigger surface area increases polymer adsorption as the polymer occupies surface adsorption sites. The rock wettability also influences the adsorption due to the affinity of the surfaces to the dispersing phase. Water-wet surfaces, for example, show an affinity for aqueous polymer solutions.

Mechanical entrapment is caused by large polymer molecules being trapped in the narrow crevices and constricted flow channels of the porous medium. The regions where it occurs might trap more molecules upstream of the blockage, relating this mechanism to deep-bed filtration. Usually, the higher entrapment is reported near the inlet of the core, and it decreases exponentially along the core length. Mechanical entrapment is also a function of polymer concentration. The increase in polymer concentration increases the number of polymer molecules per unit of volume,

raising the probability of molecular retention on rock surfaces (Zhang and Seright, 2015; Dang et al., 2014; Sazali et al., 2019). Moreover, the effluent concentration of the core decreases to the input concentration due to polymer entrapment. The inlet and outlet concentration would only be similar after several pore volumes of pumped solutions. Lastly, the pore space can be completely blocked above a critical number of entrapment sites, falling the core permeability to zero.

Hydrodynamic retention regards the total level of polymer retention as a function of fluid flow rate. There are some questions around this mechanism, but it is widely noticed that the polymer retention observed in steady-state experimental conditions can be different depending on the flow rate. High polymer injections lead to high polymer retention. It is attributed to the tendency of polymer molecules to be trapped in the stagnant flow regions by hydrodynamic drag forces. The reversibility of retention, however, is still controversial in the literature.

Usually, a mechanism of polymer retention can not happen isolated. All mechanisms are related, and one type may trigger the others. It has been reported that adsorption tends to predominate in high permeable rocks, while mechanical entrapment and hydrodynamic retention in low permeable rocks (Al-Hajri et al., 2018; Chhabra and Richardson, 2008; Huh, Lange and Cannella, 1990).

Figure 2.6 illustrates the above mechanisms of polymer retention.

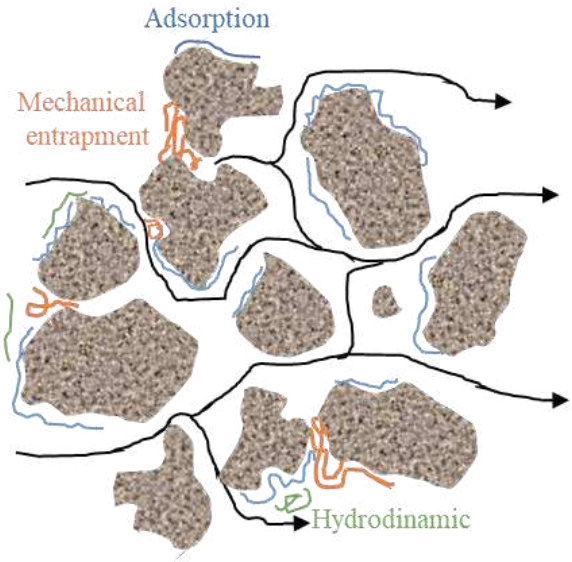

Figure 2.6: Polymer retention mechanisms: adsorption, mechanical entrapment, and hydrodynamic retention (based on Sorbie, 1991).

2.2.2 External cake formation

The external cake formation occurs by the deposition of particle solids larger than the reservoir pores in the external wall of the borehole. The initial formation of the dynamic filter cake plays a key role in controlling the quality of the formed cake and filtration properties. Under static conditions, the particle size distribution of the filter cake resembles the particle size distribution of

the mud. However, under dynamic conditions, specific particle size fills the opening space in the cake that is being formed. Usually, dynamic cakes tend to present lower permeability and porosity than static cakes. The cake thickness, in turn, depends on the filtrate loss and the amount and type of solids in the mud. Thin cakes are desirable to reduce formation damage and wall sticking. The dynamic cake reaches a finite thickness once the balance between the deposition and erosion is reached. Under static conditions, however, the cake thickness tends to increase as the time of operation stops increase (Chesser et al., 1974).

Salehi et al. (2015) studied the effect of particle bridging, filtrate invasion, and permeability performing HTHP filter press tests with water-based mud and sandstones. The filtration tests showed that fine size of $CaCO_3$ as a primary agent had the best performance in reducing filtration (an average of more than 10 mL reduction in cumulative filtration). Besides, higher spurt loss was observed in higher permeability samples. The effect of the bridging agent solids and viscosifier (XG and carboxymethylcellulose -CMC) was also studied by Ferraz (2014). The author used filter paper in the HTHP filter press. Smaller sizes of bridging agents built a less porous and permeable cake. The cake permeability decreased as the pressure drop increased from 500 to 1000 psi for all ranges of $CaCO_3$ sizes. The decrease in the cake permeability as the pressure increases was also reported by Magioni (2015). Ezeakacha and Slehi (2017) developed an experimental and statistical investigation of drilling fluid loss to evaluate the influence of temperature, concentration, and size distribution of bridging agents and petrophysical characteristics of porous media. An increase of 37.7 °C increased dynamic fluid loss up to 40%. High spurt and cumulative volume losses are associated with high porosity and permeability formations. For both sandstones and limestones, an increase in permeability resulted in a more than 50% increase in dynamic fluid loss. The rate of fluid invasion was strongly dependent on the early evolution of internal filter cake and particle size agglomeration.

Ramézani et al. (2015) modeled the filtrate drilling fluid to assess the initial and final permeabilities, fluid flow rate, and damage ratio in formation damage, including/excluding the inertial effects for static and dynamic conditions. Damage ratio corresponds to the difference between the initial and final permeabilities divided by the initial permeability of the medium. The experimental test injected mud through a horizontal sandstone core in a Hassen cell. They also related the influence of petrophysical rock properties on the cake formation, i.e., cakes formed in highly porous and permeable rocks tend to be less voluminous. The cake thickness had a non-linear growth over time for both conditions with and without inertial effect. Iscan, Civan, and Kok (2007) also noticed the permeability damage ratio. The authors verified that the damage ratio increased as the filtration pressure increased and kept constant.

2.3 Fluid flow through non-deformable porous media

The continuum approach mathematically describes the fluid flow through non-deformable porous media. According to Massarani (2002), for a fixed reference in a porous medium, the

equations of continuity and momentum for the fluid component in the integral form are given by Equations 2.7 and 2.8, respectively:

$$\int_{V_R} \frac{\partial}{\partial t}(\varepsilon\,\rho)dV + \int_{S_R} \varepsilon\,\rho\,u\,.n\,dS = 0 \tag{2.7}$$

and

$$\int_{V_R} (\varepsilon\,\rho\,u)dV = \int_{S_R} T\,n\,dS - \int_{V_R} m^*\,dV + \int_{V_R} \varepsilon\,\rho\,g\,dV \tag{2.8}$$

where SR and VR are the surface and volume integrals from the region R, respectively, ρ is the specific mass of the fluid, u is the interstitial fluid velocity, T is the tension tensor that acts in the fluid phase, m^* is the force exerted by the fluid on the porous matrix, and g is the gravitational force.

The interstitial and superficial, q, fluid velocities are related by Equation 2.9:

$$q = \varepsilon\,u \tag{2.9}$$

In the tension tensor, the isotropic part of the tension tensor that acts on the fluid in the porous medium is the pressure, p, as it is shown by Equation 2.10:

$$T = -p\,I + T^{"} \tag{2.10}$$

where I is the identity tensor, $T^{"}$ is the constitutive part of the tensor, corresponding to the extra tension, and it is a function of the superficial velocity. The static part of the tensor tension is $p\,I$, while the dynamic one corresponds to $T^{"}$.

The force exerted by the fluid on the porous matrix, i.e., the interaction force fluid-particle, can be separated in the resistive force, m', and buoyancy force. See Equation (2.11):

$$m^* = m' - (1-\varepsilon)\,\rho\,g \tag{2.11}$$

Therefore, the continuity and momentum equations for the fluid in the differential form are given by Equations 2.12 and 2.13, respectively:

$$\frac{\partial}{\partial t}\left(\varepsilon\,\rho_f\right) + div\,(\rho\,q) = 0 \tag{2.12}$$

and

$$\left(\varepsilon\,\rho_f\right)\left[\frac{\partial u}{\partial t} + (grad\,u)u\right] = -grad\,p - m' + div\,T^{"} + \rho g \tag{2.13}$$

For uniform and incompressible flows, the momentum equation can be described by Equation 2.14:

$$-grad\ p = \frac{\Delta P}{l_m} = m' \tag{2.14}$$

where ΔP is the pressure drop, l_m is the medium length and $\Delta P/L$ is the pressure drop per unit length.

Constitutive equations describe the resistive force. Darcy's law and the Forchheimer equation are the widest expressions used in the literature.

Darcy's law is the simplest model to describe the single-phase flow of incompressible fluids through porous media and fractures at low flow rates. This law assumes that viscous forces dominate over inertial forces in porous media. It is also valid for isothermal and purely viscous fluids (Takhanov, 2011; Sochi, 2010). Darcy's law describes a linear relationship between the pressure drop per unit length and the superficial velocity, as it is shown by Equation 2.15:

$$\frac{\Delta P}{L} = \frac{\mu}{K_m}\, q \tag{2.15}$$

where K_m is the medium permeability and μ is the viscosity of the injected fluid.

The inertial effects become more relevant as the flow rate increases, and the relationship between the pressure drop per unit length and the superficial velocity becomes non-linear. At this condition, the flow velocity difference between pore throats and pore bodies causes turbulences. First, in the weak inertial regime, both the inertial and the viscous forces have the same order of magnitude. As the flow rate increases further, the pressure loss transforms from weak to the strong inertial regime, known as the Forchheimer regime (Takhanov, 2011). In this case, the pressure drop per unit length is proportional to the square root of superficial velocity, as it is shown by Equation 2.16:

$$\frac{\Delta P}{L} = \frac{\mu}{K_m}\, q + \beta\, \rho\, q^2 \tag{2.16}$$

where β is the non-Darcy flow coefficient.

The non-Darcy coefficient is a parameter for quantifying the non-Darcy flow effect. It is an intrinsic property of the medium and represents the additional inertial resistance caused by the pore space structure, i.e., the converging/diverging and tortuous medium geometry (Balhoff and Wheeler, 2009; Huang and Ayoub, 2006). In a single-phase system, it decreases with the increase of permeability and porosity (Takhanov, 2011).

Several authors have been proposing empirical correlations and theoretical equations to estimate the non-Darcy coefficient. An extended literature review about some models was elaborated by Takhanov (2011) and Li and Thomas (2001). In this thesis, three different models (M1, M2, and M3) were evaluated based on the petrophysical characteristics of ceramic filters provided by the manufacturer and obtained in laboratory tests. The models were proposed by: (i) Ergun (1952) (Equation 2.17, M1), which is used by Massarani (2002) to describe the fluid flow through undeformable media; (ii) Jone (1987) (Equation 2.18, M2), used by Souza and Souto

(2015) in their work; (iii) and Janicek and Kartz (1955) (Equation 2.19, M3) also used by Souza and Souto (2015) and Cruz, Boy and Pires (2011).

$$\beta = \frac{c}{\sqrt{K_m}} \tag{2.17}$$

where c is the dimensionless Ergun coefficient (dependent on the flow regime) determined through experimental tests.

$$\beta = \frac{6.15\ 10^{10}}{K_m{}^{1.55}} \tag{2.18}$$

where β [1/ft] and K_m [mD]

$$\beta = 1.82\ 10^{8}\ K_m^{-5/4} \varepsilon^{-3/4} \tag{2.19}$$

where β [1/cm] and K_m [mD]

The above equations are valid for Newtonian fluids. In the case of non-Newtonian fluids, the fluid viscosity should be replaced by the effective viscosity. It corresponds to the apparent viscosity experienced by the fluid inside the pore, i.e., in situ viscosity. In this case, the shear rate is given by a characteristic distension rate, γ^*, (a kinematic flow property) described by Equation 2.20 (Massarani, 2002). The effective viscosity is correlated with measured parameters, such as superficial velocity and rock properties like porosity and permeability (Ferreira, 2019).

$$\gamma^* = \frac{1.1}{(t'\ \varepsilon)^{1/2}} \frac{q}{\sqrt{K_m}} \tag{2.20}$$

where t' is a structural factor of the porous media (t = 2.5 (Silva and Massarani, 1979)).

The flow regime in porous media can also be evaluated by the Reynolds number, which represents the ratio of inertial to viscous forces in the flow. Several models have been proposed to evaluate the Reynolds number for flow in porous media in the literature. This thesis used the models described by Huang and Ayoub (2006) Equations 2.21 and 2.22, and the model described by Madlener, Frey, and Ciezki (2009), and Metzner and Reed (1955) (Equation 2.23). They differ in the characteristic length and the non-Newtonian behavior of fluids.

$$Re_i = \frac{\rho\ q\ d_p}{\varepsilon\ \mu} \tag{2.21}$$

where Re_i is the interstitial Reynolds number and d_p is the average diameter of the pore.

$$Re_k = \frac{\rho\ q\ K_m^{1/2}}{\mu} \tag{2.22}$$

where Re_k is the modified Reynolds number.

$$Re_{gen} = \frac{\rho\ d_p^n\ q^{2-n}}{m\ 8^{n-1}} \tag{2.23}$$

where Re_{gen} is the generalized Reynolds number.

Flow regimes in porous media are classified from small to large Reynolds numbers, corresponding to the stages of Darcy, weak inertia, Forchheimer (strong inertia), transition for Forchheimer to turbulence, and turbulence (Kundu, Kumar, and Mishra, 2016; Skjetne, 1995). A large dispersion of the thresholding limiting values for transitions between the flow regimes has been reported in the literature. Darcy's flow regime is characterized by $Re_i < 1$. At $Re_i \sim 1$, bound layers start to develop near the walls of the pores. When the boundary layers become more pronounced, the inertia effect appears and Re_i ranges from 1 ~ 10. This form of steady nonlinear laminar flow occurs up to $Re_i \sim 150$. Wake oscillations and the development of vortices occur in an unsteady laminar flow regime for $Re_i = 150 \sim 300$. Lastly, a highly unsteady and chaotic flow regime occurs for $Re_i > 300$ (Huang and Ayoub, 2006).

2.4 Fluid flow through non-deformable porous media and cake combined

Filtration is the separation of particles from slurries in a filter medium that is permeable to fluid flow but does not allow particle percolation. The particles retained at the surface of the medium form a cake (Geankoplis, 1993). During the process of cake formation and growth, specifically for cakes with a degree of compressibility, the structure of the cake – like porosity, permeability, and thickness – varies with time as the compressible stress throughout the cake varies with time (Ni, 2001).

Several models have been reported to predict incompressible and compressible filter cake thickness, filtrate volume, filtration rate for linear and radial filtrations under static and dynamic filtration conditions (Civan, 2007). Dewan and Chenevert (2010) proposed a model that describes the volume of solids in the cake as a function of the filtration time. Civan (2007) showed several equations to model static and dynamic filtrations. Ferreira and Massarani (2005) proposed a model for crossflow filtration. Ni (2001) proposed equations for modeling and simulating the cake formation with some forces explicitly.

In this thesis, the proposed model was developed based on the conventional and simplified filtration theory reported by Massarani (2002). This model was also used by Damasceno (1985), Oliveira Junior (2014), and Maginoni (2015). The simplified filtration theory assumes that the superficial velocity of solids in the cake is lower than in the fluid phase, i.e., the fluid velocity is only a function of time. It is acceptable when the cake is slightly compressible, decreasing the complexity of the filtration equations.

In cake filtration, the fluid phase passes through two resistances in series, i.e., through the cake and filter medium, and its superficial velocity is the same through both media. It is shown in Equation 2.24:

$$\Delta P = \mu\, q \left(\alpha \frac{M}{A} + R_m\right) \tag{2.24}$$

where α is the specific cake resistance (Equation 2.25), M is the mass of solids in the cake (Equation 2.26), A is the cross-sectional filter area, and R_m is the filter medium resistance (Equation 2.27).

$$\alpha = \frac{1}{\rho_s(1-\varepsilon_c)K_c} \tag{2.25}$$

where ρ_s is the specific mass of the solid, ε_c is the cake porosity, and K_c is the cake permeability.

$$M = C\, p_{fil}\, V \tag{2.26}$$

where C is the mass concentration of solids in the suspension (mass of solid per mass of fluid in the suspension), p_{fil} is the specific mass of the filtrate.

$$R_m = \frac{l_m}{K_m} \tag{2.27}$$

The superficial velocity of the filtrate can be described by the volume of fluid, V, flowing through the cross-sectional area in time, t. It is given by Equation 2.28:

$$q = \frac{dV}{dt}\frac{1}{A} \tag{2.28}$$

2.5 X-ray micro-CT

X-ray micro-CT is a non-destructive imaging technique widely applied in geoscience that enables the 3D characterization of rocks. It is made possible due to sample rotation in front of the X-ray source resulting in different angular projections that are then reconstructed (Cnudde and Boone, 2013). Usually, the images can be acquired at high resolutions as the miniature cores can be exposed to high-energy X-ray beams for a long acquisition time (Arshadi et al., 2017; Machado et al., 2016; Khishvand, Akbarabadi, and Piri, 2016).

X-rays are high-energy electromagnetic waves resulting from electron collision in a metal target. When a source of cathode rays, such as a hot filament tube, is exposed to a large potential difference (Kilovolts, KV), an electron current (Microampere, μA) is produced and accelerated until colliding with a metal target anode. During the collision, the electrons are decelerated, and heat and X-rays are generated. The electron gun, the target, and the potential difference generator are called X-ray tube, and it operates under vacuum (Brown, 1975).

Figure 2.7 shows a laboratory-based micro-CT setup with a conical X-ray beam that allows geometrical magnification.

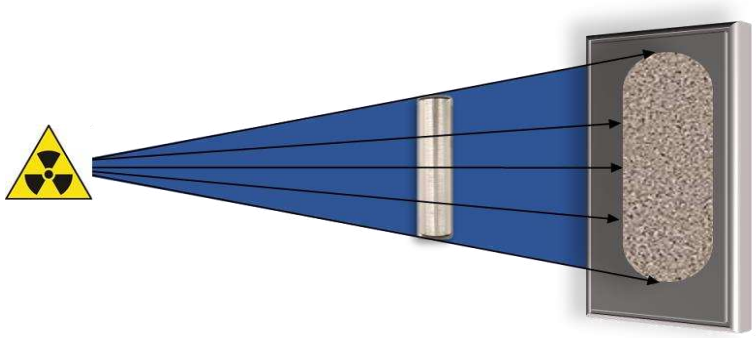

Figure 2.7: Laboratory-based micro-CT setup (based on Cnudde and Boone, 2013).

The X-ray principle is based on the attenuation of monochromatic X-rays that follow a straight path through a material with a specific attenuation coefficient. Mathematically, it is formulated by Beer's law, as it is shown in Equation 2.29 (Cnudde and Boone, 2013):

$$I' = I'_0 \, e^{-\mu' l_m} \tag{2.29}$$

where: I' and I'_0 are the X-ray beam after and before pass through the sample, in this order; and μ' is the local linear attenuation coefficient of the sample.

The micro-CT images are often analyzed to obtain pore fluid occupancy, pore and throat size distribution, porosity, relative permeability, capillary pressure, wettability state, pore space deformation, and connectivity. Berg et al. (2015) studied the onset of oil mobilization during imbibition by flowing brine in sintered glass, sandstone, and carbonate porous media with distinct petrophysical features. The largest and initially connected clusters broke off into smaller segments that could break again or reconnect as the imbibition stages went on. In a similar line, Guo et al. (2018) investigated the effects of pore structure and permeability in the oil displacement efficiency and remained oil-cluster morphology. The authors showed that large clusters were broken into small segments in high permeable media. Besides, the greater the coordination number, the more significant the imbibition performance was. Zhang et al. (2019) analyzed brine injections through limestone under variable effective stress. They evaluated the effect of the petrophysical properties of rocks, stress change, and fluid flow on rock microstructure integrity. The less consolidated areas in the porous medium were easily broken, increasing pore space porosity and connectivity. The effective stress had a minor impact on the rock microstructure.

Singh et al. (2019) showed that both snap-off and pore-filling events (imbibition mechanisms) were strongly correlated with the aspect ratio and weakly to throat shape factor. Small aspect ratios favor piston-like occurrence. They also reported a new type of pore snap-off caused by the pinning of fluid-fluid interfaces at rough surfaces. It led to the formation of a non-wetting ganglion in a fraction of the pore body.

Snap-off and pore-filling (piston-like) are two processes whose competition controls the nature of the displacement in imbibition mechanisms. Snap-off is the swelling of wetting layers, usually trapping the non-wetting phase in larger pores surrounded by the wetting phase in narrower

regions. Piston-like, in turn, is the directing filling of pores and throats from adjacent pores occupied by the wetting phase (Blunt, 2017).

Nguyen et al. (2006) investigated the aspect ratio and rate-dependence in imbibition relative permeability and residual saturation. While the time for filling the pores and throats was rate dependent, the swelling of wetting films was mostly independent. The higher the aspect ratio, the larger the rate effects. The increase in both the displacement rate and contact angle suppressed the snap-off mechanism, favored relative permeability curves, and decreased the residual non-wetting saturation. Rücker et al. (2015) reported that snap-off events trigger the coalescence of non-wetting phase clusters. The authors stated that besides the pressure-driven connected pathway flow, mass transfer of the oil happens by a sequence of breakup and coalescence in a ganglion-dynamic process.

3. Methodology

This section describes the original methodology applied in this thesis by elucidating the experimental setups, procedures, and data collection for analyzing the pore space characteristics and polymer concentration in the formation of inner and external filter cakes. First, it outlines the properties of XG and $CaCO_3$, the preparation of the polymer solutions and suspensions, and their rheological characterizations. Then, it details the procedures performed in Studies 1 and 2. Study 1 was carried out at the Federal University of Uberlândia, Minas Gerais, Brazil, and Study 2 at the University of Kansas, Kansas, United States of America.

In this thesis, to study inner and external cake formations, the mud was simplified by a polymer solution of XG and a suspension of $CaCO_3$ in XG solution, respectively. The aqueous polymer solution reproduces a water-based drilling fluid. Although this fluid simplifies real drilling fluids, it has the same rheological behavior as muds and is a component of mud formulation. So, enough and good insights about non-Newtonian fluid flowing through the porous medium were achieved.

3.1 Filtration tests: Study 1

This subsection describes the methods used to characterize the materials used in Studies 1A and 1B and to perform the filtration tests.

3.1.1 Characterization of XG and $CaCO_3$ solids

XG from Êxoto Científica (G22407RA) and $CaCO_3$ from Provale Indústria e Comércio S/A were used in this part of the research.

✓ Experimental setup

A Micromeritics (AccuPyc 1330) gas pycnometer was used to measure the specific mass of $CaCO_3$ and XG. Tests were performed with helium, in quintuple, and at room temperature (25 °C).

The solids were characterized by scanning electron microscopy (SEM) (Zeiss, EVO MA 10) with different magnifications. For the SEM analysis, samples were fixed to an SEM spin stub with a conductive adhesive and then coated with a thin layer of gold (56 nm) using a sputtering device (LEICA EM SCD050).

$CaCO_3$ particles were analyzed regarding their size distribution by laser diffraction in a Malvern Mastersizer Microplus. The dispersion of the solids was ensured by adding them to an aqueous solution of Calgon (1 g/L), used as a dispersant in an ultrasonic bath for 30 seconds. Tests were run in triplicate at room temperature (25 °C). Then, the Rosin-Rammler-Bennet (RRB) model (Equation 3.1) was fitted to the volumetric diameter of the particle, d_p', and the cumulative fraction of solids, X, using the Statistica® software.

$$X = 1 - \exp\left(-\left(\frac{d'_p}{d_{0.632}}\right)^{n'}\right) \quad (3.1)$$

where $d_{0.632}$ and n' are the model parameters related to the characteristic particle size corresponding to 63.2% of the cumulative distribution and the uniformity coefficient indicating the wider size distribution, respectively.

3.1.2 Preparation of XG solutions and $CaCO_3$ suspensions

✓ Experimental setup

XG solutions and $CaCO_3$ suspensions were prepared in a mechanical helix propeller stirrer (Ika Labortechdade, RW 20D2Mn), ranging from 0 to 2000 rpm.

✓ Experimental procedure

The aqueous solutions of XG 0.2 and 0.4% (m/m) were formulated by adding XG, water, and formaldehyde, as it is shown in Table 3.1. The formaldehyde aims to avoid the proliferation of microorganisms, ensuring the rheological stability of the solutions. The compounds were mixed at 1600 rpm for 1 hour. Then, the solutions rested for 24 hours to provide polymer hydration (Moreira, 2014).

Table 3.1: Formulation of the aqueous solution of XG.

XG solution	XG [g]	Water [mL]	Formaldehyde [mL]
0.2	2	998	2
0.4	4	996	4

The $CaCO_3$ suspensions 5% (v/v) were prepared by adding $CaCO_3$ into 300 mL of XG solution. The compounds were mixed at 1600 rpm for 10 minutes to ensure a homogeneous suspension.

3.1.3 Rheological characterization of XG solutions and $CaCO_3$ suspensions

The XG solutions and $CaCO_3$ suspensions were characterized regarding their specific mass and rheological behavior.

✓ Experimental setup

The specific mass characterization was done by pycnometry using a 25 mL pycnometer.

The rheological experiments were carried out in a Brookfield Low-Viscosity Digital Viscosimeter (LVDV2T). The spindle geometry was cone/plate SC4-18 and SC4-31 for XG 0.2 and 0.4% (m/m), respectively. The RheocalcT software was used to report the data, and the tests were done in triplicate. The temperature was set at 25 °C using a thermostatic bath.

✓ Experimental procedure

The specific mass was calculated by the ratio of the weight of the solutions (and suspensions) to the volume of the pycnometer.

XG solutions were rheological characterized by the plots of rheogram, shear stress peak, and thixotropic hysteresis. $CaCO_3$ suspensions, in turn, were characterized only by the rheogram test. The rheogram represents the relation between the shear stress to the shear rate in a steady-state condition. The shear stress peak evaluates the impact of the resting time in forming gelled structures. The thixotropic hysteresis considers the time dependence of shear stress and apparent viscosity (Chhabra and Richardson, 2008; Machado, 2002).

The rheology experiments consist of three stages. First, the highest shear rate was applied in the samples (solutions and suspensions) to break any possible gel structure. This stage was called a pre-shear rate. Then the samples rested to reorganize their molecular chains (Melo, 2008). Lastly, different shear rates were applied to evaluate the shear stress response.

In the rheogram test, the samples were pre-shared at 100 (XG 0.2% (m/m)) and 68 s^{-1} (XG 0.4% % (m/m)) for 1 minute and then rested for 5 minutes. In the last stage, they were sheared by different shear rates (1, 5, 10, 25, 50, 68, and 100 s^{-1}) until the steady-state condition was achieved. The highest shear rate of 100 and 68 s^{-1} were applied only in the XG 0.2 and 0.4% (m/m), respectively, due to the accuracy range of the spindle rotation in each fluid.

The power-law rheological model (Equation 2.5) was fitted to the shear stress and shear rate experimental data. It was chosen because of its simplicity (bi-parametric) and precision in characterizing non-Newtonian fluids.

In the shear stress peak analysis, the initial stage was the same as the rheogram test. However, three different resting times (10 seconds, 10 minutes, and 30 minutes) were evaluated. The final shear stage was performed at 1 s^{-1} until the shear stress response achieved the steady-state condition, and the experimental data were recorded every second.

Finally, in the hysteresis test, the pre-shared stage was performed at 50 s^{-1} for 1 minute and the resting time was 5 minutes. The final shear rates were 1, 5, 10, 25, and 50 s^{-1}, and they were applied for 20 seconds each in a sequence of increase and decrease of the rate. The hysteresis test aims to evaluate the time dependence of the fluid, so the shear stress response should be recorded before the steady-state condition is achieved. The same range of shear rates was applied in the XG solutions to compare the hysteresis area of both samples using Origin software.

3.1.4 Solution and suspension flow

Figure 3.1 illustrates an overview scheme about the filtration experiments performed in Studies 1A and 1B. The aqueous solutions of XG and $CaCO_3$ suspensions were used as drilling fluids in the inner and external filter cake formation studies, respectively.

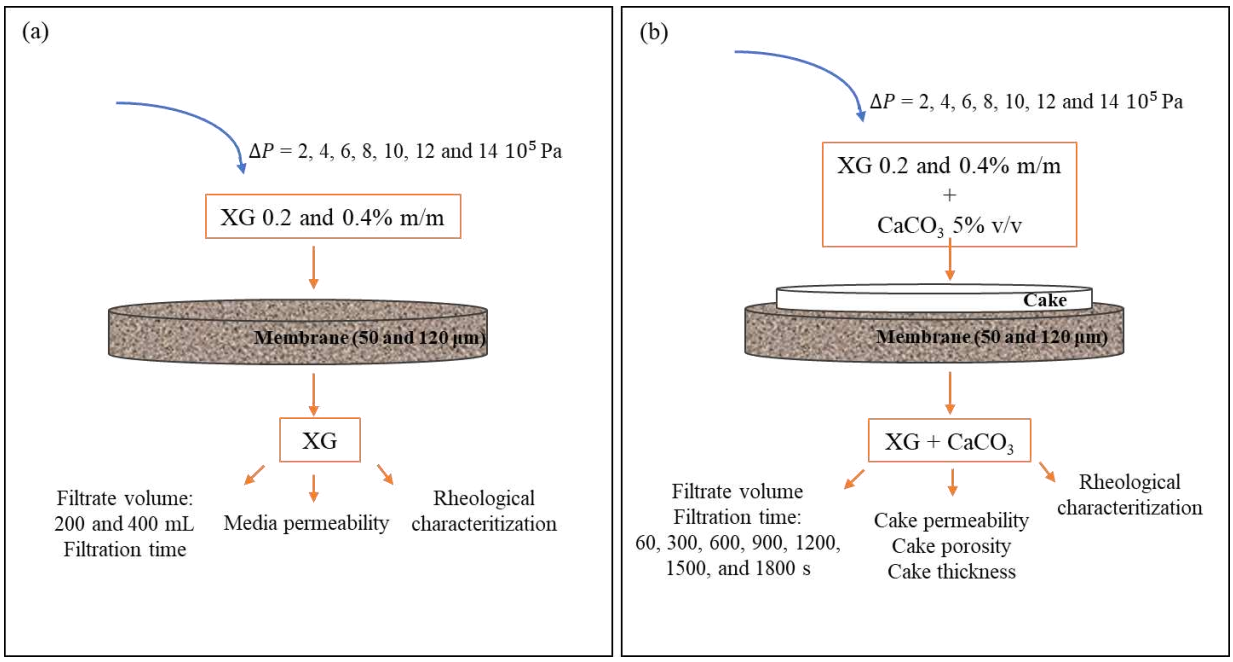

Figure 3.1: Overview scheme about the filtration experiments for (a) Study 1A and (b) 1B.

✓ Experimental setup

The OFITE HTHP dynamic filter press (170-50) was used to perform the filtration tests. It is composed of a 500-mL stainless steel test cell, the top (motor-driven shaft fitted with a propeller) and end caps with a threaded hole for the valve stems, and the porous ceramic filter as the filter medium (membrane).

The system was pressured by a nitrogen (N_2) line that connected the N_2 cylinder to the valve stem at the top cap. The valve stem was open to the atmosphere in the end cap, and the filtrate was collected in a beaker. Figure 3.2 illustrates the HTHP filter press apparatus in the laboratory, its main components, and its lateral view according to its instruction manual. In the lateral view, the valve stem in the end cap is connected to a removable backpressure receiver that was not used in this study.

The ceramic filters reproduce similar porosities and permeabilities to those of the drilled formations and enable the evaluation of mud invasion (fluid loss) and the bridging characteristics of drilling fluids. According to OFITE, porous ceramics consist of closely-sized alumina and silica particles (mostly) bonded together, resulting in a uniform and permeable medium that forms a tortuous path for fluid flow. The ceramic filters are 6.35 cm in diameter and 0.635 cm in thickness (length). Moreover, they are usually classified by mean pore throat size, i.e., the average minimum pore diameter. This study was performed in porous ceramic filters of 50 and 120 µm, whose permeabilities to mercury are reported to be 1.48×10^{-11} and 3.95×10^{-11} m^2, respectively. Figure 3.3 shows the superficial view of the ceramic filters. They were also characterized by the SEM images shown in section 4.1.3.

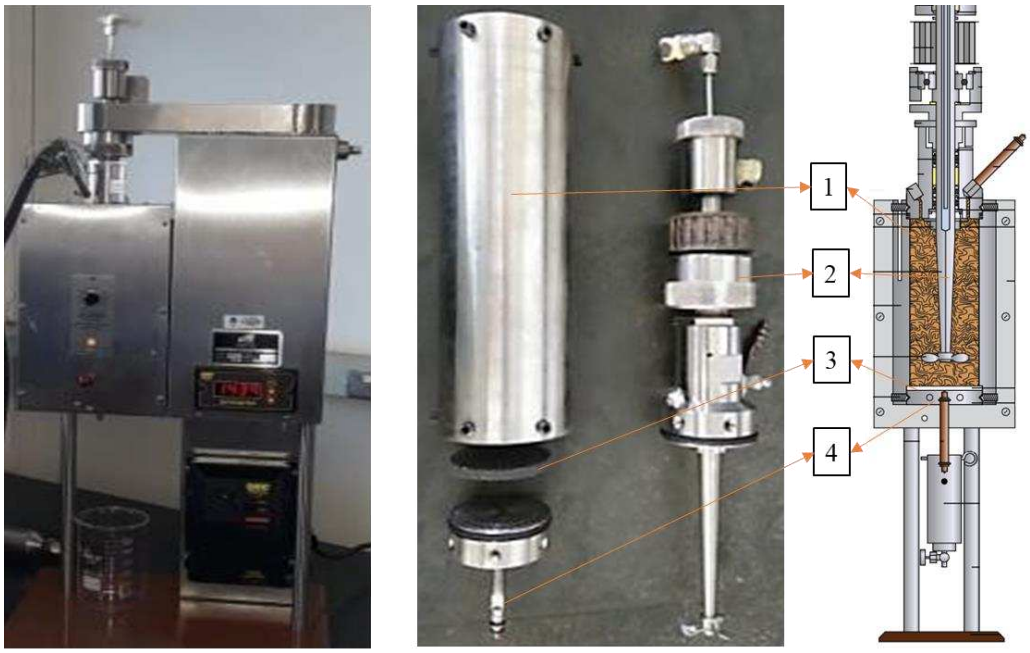

Figure 3.2: HTHP Dynamic filter press (a) in the laboratory, (b) its main components, and (c) its lateral view, being (1) the test cell, (2) the top cap (motor-driven shaft fitted with a propeller), (3) the porous ceramic filter (filter medium); and (4) the end cap.

Figure 3.3: Superficial view of the (a) 50 µm and (b) 120 µm porous ceramic filters.

✓ Experimental procedure

First, the total porosity of the ceramic filters was estimated to characterize them better. It was done by gravimetric measurements and the ratio between the volume of water in the ceramic filter and the total volume of the ceramic filter. For this, each membrane was placed in a beaker with

water and under vacuum pressure (ΔP = -670 mmHg) for 30 minutes to remove any trapped air in the pore space, ensuring its full saturation.

A similar ceramic filter saturation procedure was performed with the XG solution corresponding to the one that would be filtered before each filtration test. The membranes were placed in beakers with XG under vacuum pressure (ΔP = - 670 mmHg) for 5 minutes. This method aimed to mimic the initial saturation condition of the reservoirs.

The inner filter cake formation was evaluated by flowing the XG solutions through the ceramic filters. First, the test cell was filled with 200 mL of XG, then it was pressurized with N_2, and lastly, the valve stem in the end cap was opened. The pressure drop was kept constant during the test, and the time to collect the filtrate was recorded. The same procedure was also carried out with 400 mL of XG. The filtrate volume was expected to be similar to the one placed in the test cell. It was ensured by weighing the filtrate and measuring its specific mass with a pycnometer. The pressure ranged from $2x10^5$ to $14x10^5$ Pa, stepped by $2x10^5$ Pa. Finally, the tests were run in triplicate at room temperature (25 °C).

The numerical values of ceramic filter permeability after each experimental condition of polymeric flow were estimated using the solving tool in the Maple software. Both the Darcy and Forchheimer equations were analyzed to check out the influence of inertial effects in the fluid flow. These models were modified to incorporate the non-Newtonian characteristic of XG in the viscosity parameter. Considering that the characteristic distension rate, γ^*, corresponded to the shear rate, γ, Equation 2.20 was replaced in Equation 2.6, resulting in Equation 3.2. In this case, the rheological indexes, m and n, corresponded to the average value between the XG solution before and after filtration.

$$\mu_{ap} = m \left[\left(\frac{1.1}{(2.5\ \varepsilon)^{1/2}} \right) \frac{q}{\sqrt{K_m}} \right]^{n-1} \tag{3.2}$$

For the Forchheimer model, the non-Darcy coefficients given by equations 2.17, 2.18, and 2.19 were used to assess how the porous medium characteristics influence the flow. To obtain the c parameter in Equation 2.17, experiments similar to those described for the XG flow were carried out using water. Then, the linear form of the Forchheimer model was fitted to the experimental data. As water is a Newtonian fluid, c could be obtained by the slope of the curve. Its value was 1.64 and $1.71x10^3$ for the 50 and 120 μm ceramic filters, respectively.

Once the medium permeability was estimated, the corresponding apparent viscosity and pressure gradient were estimated for each experimental condition. Finally, the model that best described the polymer flow through the membranes was evaluated by analyzing the smallest relative error between the experimental and the estimated pressure drop values for all experimental conditions and combinations of XG concentration and membrane. The value of the Reynolds number also contributed to the analysis of the model that best described the polymeric flow. In this

case, the apparent viscosities and the media permeability estimated for Darcy's law and Forchheimer equation were used as the fluid viscosity and medium permeability in Equations 2.21 and 2.22.

External cake permeability was studied by flowing $CaCO_3$ suspensions through the ceramic filters. The impairment in medium permeability caused by fine clogging was also evaluated at this stage. Although it is widely accepted that the medium permeability remains almost constant after mud invasion, the membranes used in this study had a small thickness so that changes in the medium permeability could not be neglected.

In the beginning, the test cell was filled with 300 mL of suspension, then it was pressurized with N_2, and the valve stem in the end cap was opened. Each test was performed at a constant pressure drop and lasted 30 minutes. The filtrate was collected after 1 minute, and from 5 to 30 minutes, stepped by 5 minutes. The weight and volume of the filtrate were measured for each time step, making it possible to calculate the specific mass of the filtrate.

Once the filtration time was reached, the remaining suspension in the test cell was discarded, and the mass and thickness of the cake were measured. Then the cake was dried in an oven at 110 °C for water removal for 7 days. Later, the dry cake was weighted, and its porosity was calculated. The calculation was done by the ratio of the volume of evaporated water and volumes of water and solid in the wet cake.

To estimate both medium and cake permeabilities, a model was proposed. The non-Newtonian behavior of the suspension was accounted for by replacing both the porosity and the medium permeability with the cake properties in Equation 3.2, resulting in Equation 3.3. As the suspension filtration took longer than the XG filtration and the filtrate volume from the suspension was smaller than the filtrate volume from only XG for the same pressure drop, this study assumed that the cake controlled filtration.

$$\mu_{ap} = m\left[\left(\frac{1.1}{(2.5\,\varepsilon_c)^{1/2}}\right)\frac{q}{\sqrt{K_c}}\right]^{n-1} \tag{3.3}$$

Thus, replacing Equations 3.3, 2.25, 2.26, 2.7, and 2.28 in 2.24, Equation 3.4 was proposed:

$$\left(\frac{dV}{dt}\right)^n = \frac{\Delta P\,A^n}{\left[m\left(\frac{1.1}{(2.5\varepsilon_c)^{0.5}}\right)^{n-1}\right]\left(\frac{1}{\sqrt{K_c}}\right)^{n-1}} \Bigg/ \left(\frac{1}{\rho_s(1-\varepsilon_c)K_c}\frac{C\,p_{fil}\,V}{A} + \frac{l_m}{k_m}\right) \tag{3.4}$$

Equation 3.4 was solved by applying the Differential Evolution algorithm. It is a population-based search algorithm that optimizes a problem by iteratively improving a candidate solution based on an evolutionary process. Iteration is performed using vectorial operations considering the

different combinations among the population. In the end, the population tends to converge to the best possible solution. As this type of approach does not use information about the gradient of the objective function and the constraints, a global solution can be found. Differential Evolution was chosen as an optimization tool as it is a global search strategy widely reported in science and engineering applications.

Cake and medium permeabilities were estimated for each experimental condition defined by the XG concentration (0.2 and 0.4% (m/m)) and the membrane (50 and 120 μm). For this, an inverse problem was formulated and solved. It consisted of minimizing the objective function, OF, given by Equation 3.5.

$$\min OF\ (K_c, K_m) = \sum_{i=1}^{Np} (V_i^{exp} - V_i^{est})^2 \qquad (3.5)$$

where i is a stage of optimization, Np is the number of experimental data (population), V^{exp} is the filtrate volume obtained from the experimental tests, and V^{est} is the filtrate volume estimated by Equation 3.4.

Two constraints were added to optimize the model:

(i) the cake permeability should be lower than the medium permeability (Asme, 2005):

$$K_c < K_m$$

(ii) for each experimental condition, both cake and medium permeabilities decrease as the pressure drop increases (Maginoni, 2015; Ferraz, 2014)

$$K_c\ (P_2) < K_c\ (P_1)$$

$$K_m\ (P_2) < K_m\ (P_1)$$

where $P_2 > P_1$. Only for the first pressure drop those constrains were not applied.

The detailed information about the optimization settings applied in the Differential Evolution algorithm can be found in section A.1 of the Appendix.

The cleaning stage was the last step in the filtration tests for both flow tests of solutions and suspensions. Concurrent and countercurrent water flows were carried out twice at the highest pressure (14×10^5 Pa) to remove possible polymer and carbonate trapped in the pore space.

Finally, the filtrates of both flow tests were rheological characterized by performing the same procedure used for the rheogram of the solutions and suspensions before the filtration.

3.2 Core flooding tests: Study 2

This subsection describes the methods used to characterize the materials, design the cores, and carry out the image acquisition and analysis in Studies 2A and 2B.

Figure 3.4 illustrates an overview scheme of the core flooding experiments. Aqueous solutions of XG and mineral oil were injected to reproduce the inner cake formation and its displacement once the well is put in production, respectively.

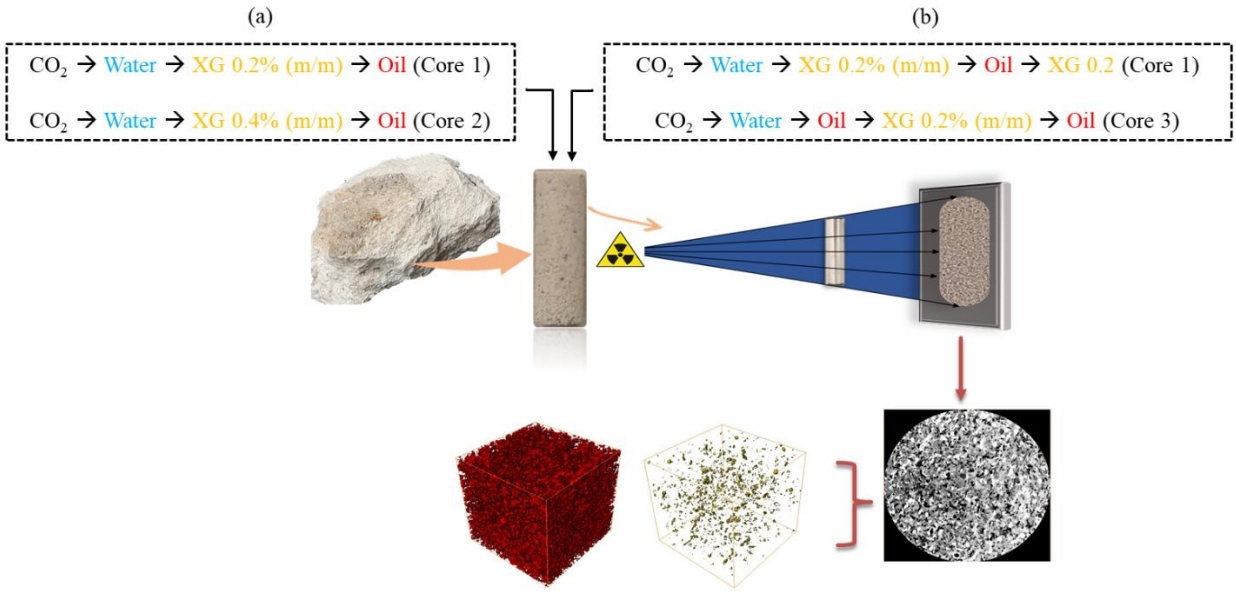

Figure 3.4: Overview scheme of the core flooding experiments for (a) Study 2A and (b) 2B.

3.2.1 Preparation of XG solutions

In this part of the research, XG from Sigma-Aldrich was used.

✓ Experimental setup

XG solutions were prepared in a magnetic stirring mixer (Isotemp, Fisher Scientific).

✓ Experimental procedure

The procedures and compounds used to prepare the XG solutions were similar to those described in section 3.1.2.

3.2.2 Design and characterization of core holders

A carbonate outcrop from Miocene Agua Amarga Basin in the southeast of Spain was used to make the core holders.

✓ Experimental setup

The core holders were designed using a drill bit to obtain the cores and epoxy to fix the core to the aluminum sheets. The aluminum cover acts as a filter by absorbing lower energy X-ray beams and reducing beam hardening artifacts in the reconstructed images (Machado et al., 2016; Teles, Lima, and Lopes, 2016).

✓ Experimental procedure

Three core samples were drilled from the outcrop using water as a coolant. Then the cores were cleaned with N_2 and dried in an oven at 110 ºC for 24 hours to remove any trapped water. Lastly, the dry cores were placed inside of an aluminum core holder with fingertight fittings on both ends.

Table 3.2 shows the core sizes. Figure 3.5 illustrates the outcrop, core, and core holder in sequence. The outcrop was also characterized by the SEM images shown in section 4.2.1.

Table 3.2: Core sizes.

Core	Length [cm]	Diameter [cm]
1	3.118	1.105
2	3.308	1.146
3	2.670	1.138

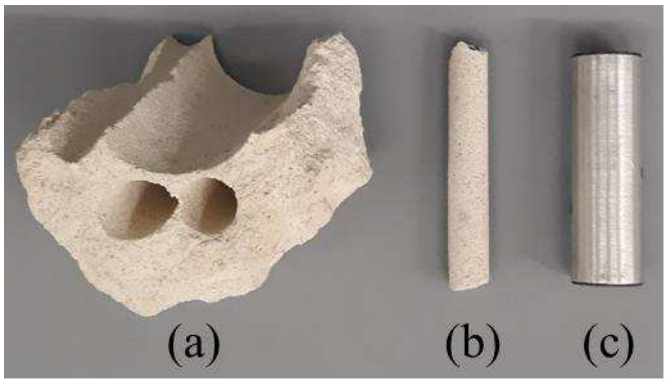

Figure 3.5: (a) outcrop, (b) core, and (c) core holder designed for Study 2.

The cores were characterized regarding their wettability, permeability, porosity, pore network features, and pore size distribution. These last three properties were determined by using digital image analysis at the pore level. The micro-CT technique and image processing are detailed in the following subsection.

3.2.3 Fluid injection

✓ Experimental setup

The core-flooding system consisted of a core holder, fluid vessels, dual cylinder Vindum pumps, a differential pressure transducer, and flexible connection lines. The water and oil injection pumps retracted the fluids from vessels and injected them into the core holders at a constant flow rate and closed-loop system. The input and output of the core holders were connected by flexible tubing. A differential pressure transducer measured the pressure drop along the core for permeability measurements under steady-state conditions.

The XG solutions, in turn, were injected into the core holders at a constant pressure using an N_2 line. The output of the core holder was open to the atmosphere, and the filtrate was collected in a gradual cylinder. Figure 3.6 illustrates the schematic diagram of the experimental apparatus.

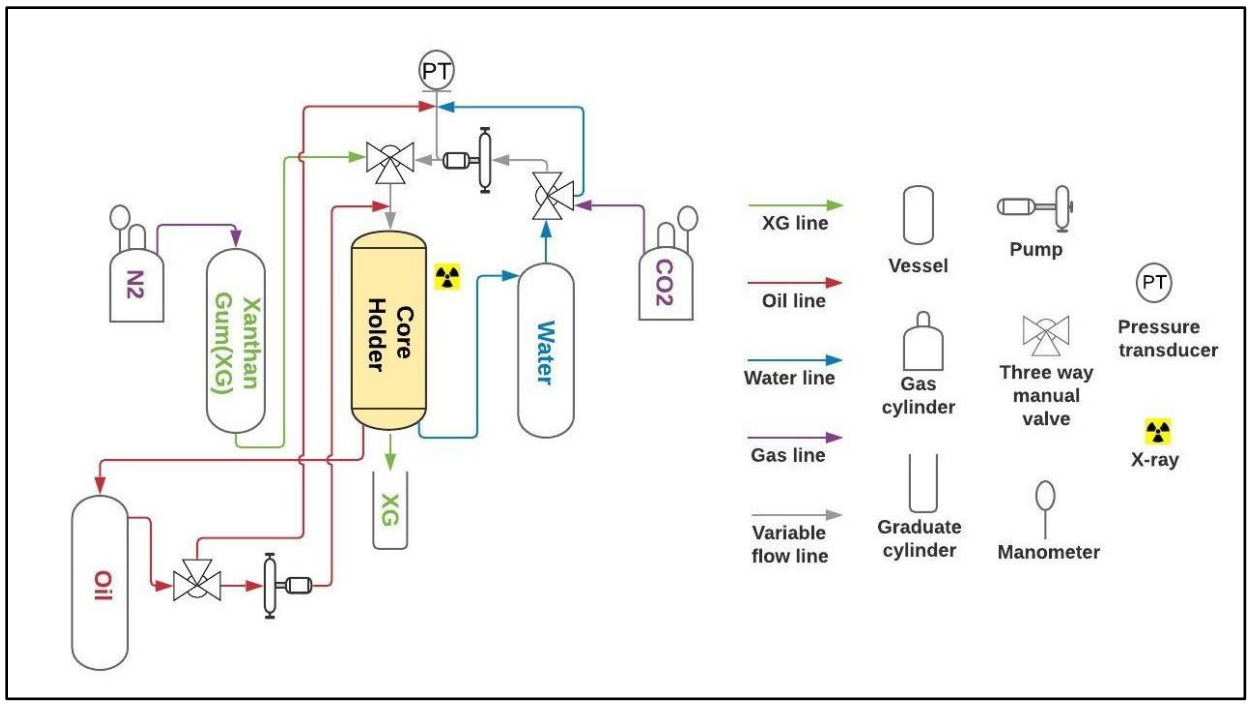

Figure 3.6: Schematic diagram of the experimental apparatus.

✓ Experimental procedure

Several pore volumes of carbon dioxide (CO2) were initially injected into the cores to saturate them and all connecting lines by displacing the air. This was done at 6.89×10^4 Pa constant pressure for 5 hours in each core holder. Then, water was injected into the cores to displace CO_2. The water pressure was occasionally raised to dissolve any trapped CO_2. At this stage, the absolute permeability values were also measured. The pressure drop was plotted to the superficial velocity of several water injections. Moreover, since carbonates are prone to dissolution in water, rock minerals were stirred in the water at 1200 rpm for 2 hours. It allowed achieving a mineral equilibrium, preventing rock dissolution and changes in the pore space (Santos et al., 2021).

In Study 2A, an average of 17 pore volumes of XG 0.2% (m/m) were injected in core 1 (experiment 1) and XG 0.4% (m/m) in core 2 (experiment 2) at a constant pressure drop of 2.07×10^6 Pa. The outlet flow rate of the polymer solutions was measured in the first experimental hour. Once the pore space was fully saturated with polymer, oil-to-XG displacements (drainage) were performed using Soltrol mineral oil #170. The oil was doped with 8% (v/v) Iodooctane to generate enough X-ray contrasts between XG and oil. The oil was injected at different flow rates to evaluate its impact on pore-level fluid occupancies, as Table 3.3 lists.

In Study 2B, experiments 3 and 4 were performed. Experiment 3 corresponds to the re-injection of 17 pore volumes of XG 0.2% (m/m) into core 1 after the third drainage stage at a constant pressure of 2.41×10^6 Pa.

Table 3.3: Oil flow rate in each drainage stage of experiments 1 and 2.

Oil stage	Core 1	Core 2
	Oil flow rate [mL/min]	
1st drainage	0.25	0.025
2nd drainage	3.00	0.300
3rd drainage	12.00	1.100

In experiment 4, oil was pumped at 0.08 mL/min after water injection, resulting in a multiphase initial saturation condition in core 3. Once the initial saturation was set, 10 pore volumes of XG 0.2% (m/m) were injected. The injection pressure of XG was gradually increased from 2.07 to $8.27x10^6$ Pa due to the low permeability and high aspect ratio of core 3, as will be discussed in section 4.2.1. In the end, the XG displacement was evaluated by injecting oil at 0.05 mL/min.

Lastly, the experiments were performed ex-situ, i.e., outside of the micro-CT chamber. Ex-situ experimental setups provide better control over the pressure and temperature of the tests, and multiple experiments can be run in parallel. All injections were done from top to bottom of the vertically oriented cores, and only one fluid was injected into each step. The tests were run at room temperature (22 °C).

3.2.4 Data acquisition and image analysis

✓ Experimental setup

The Thermo Scientific™ HeliScan™, a micro-CT imaging system, was used to image the cores after each experimental stage. The system has a dedicated feedthrough aperture and limited stage rotation capability and was operated at 100 KV and 80 μA. As part of the imaging system, a Varian Flat Panel camera with 1 binning number and 9 camera shifts in an X-ray detector with 0.139 x 0.139-pixel matrix was exposed to 1.1 seconds and operated to take 2800 projections per revolution. A double-helix trajectory was used for the sample rotation yielding an average resolution of 7.13 ± 0.03 μm voxel sizes. The image acquisition time was an average of 19 hours per scan. Thermo Scientific™ PerGeos, a digital rock analysis software, was used to reconstruct the projections and analyze the images.

Figure 3.7 illustrates the configuration and components of the X-ray chamber used in this study.

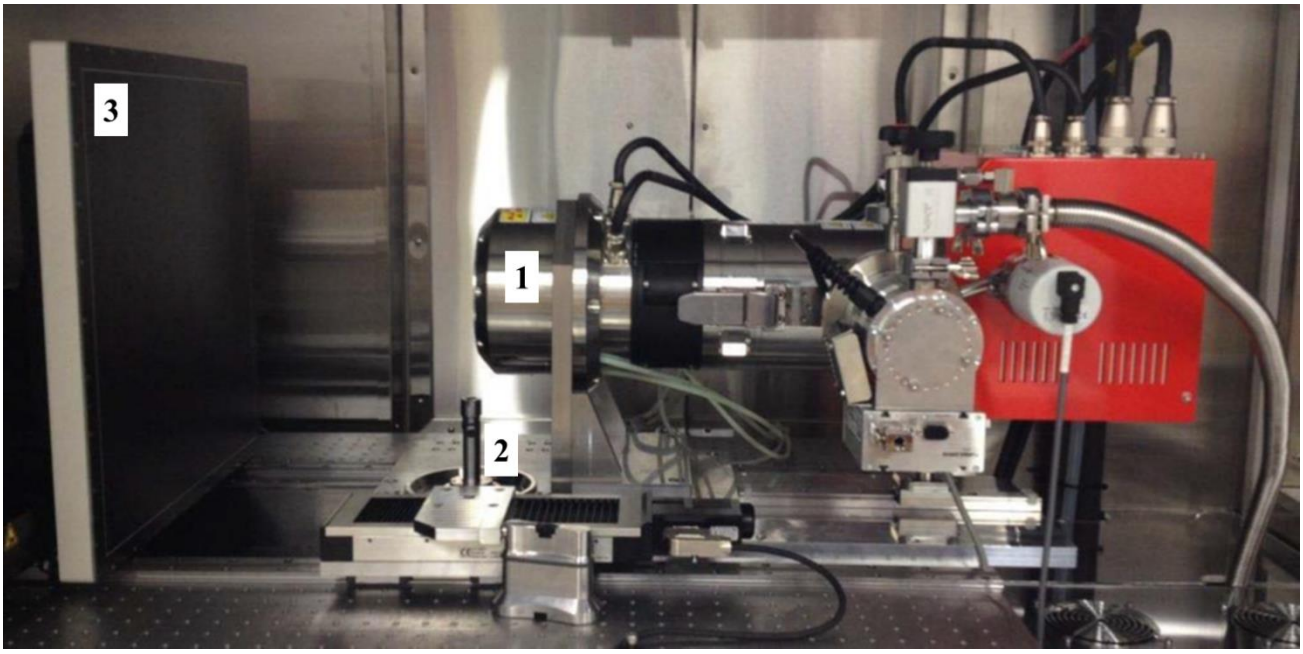

Figure 3.7: X-ray chamber and its configuration and components: (1) X-ray gum, (2) sample support, and (3) detection panel.

✓ Experimental procedure

Two sets of images called reference and target were collected to enable image analysis. Reference-state images were taken after XG injection in cores 1 and 2 and after water injection in core 3. They were used to segment the resolvable pore space. Target-state images were collected after each oil injection and applied to identify pore fluid occupancies changes at different experimental stages. Then, the two-dimensional (2D) planar X-ray projections were reconstructed using a Filtered Back Projection (FBP) algorithm, resulting in grayscale 3D images.

The reconstructed images were first filtered by applying a non-local means filter. It removed the noise, sharpened the phase boundaries, and cleaned the features resulting in a smoothed image.

Next, the reference and target state images were registered to assist with the segmentation of the pore space. The registration step is often challenging in carbonate images, and it is done by overlapping both 3D image sets. The target images were manually and computationally aligned with the reference image. The registration quality was evaluated by comparing cross-section images from both states in various planes perpendicular to the X-, Y-, and Z-axes. This stage was facilitated since both the reference- and target-state images were acquired with similar scan parameters and resolutions.

The next stage was the segmentation of the resolvable pore space. The histogram-thresholding method was used to obtain seed of pore, micropore, and grain from the reference image. Using a watershed algorithm, each voxel was marked as pore, micropore, and grain. Then, the extracted pore map was multiplied, pixel by pixel, by the target image to obtain the pore space in the target-state image. The latter had zero value corresponding to the micropore and grain regions and non-

zero values representing different fluid phases. This procedure reduced the segmentation error due to similar X-ray attenuation of the doped oil and microporosity (Qin, Arshadi, and Piri, 2019; Arshadi et al., 2018). The same methodology of histogram-thresholding and watershed analysis was applied to delineate the boundaries for XG or water from the oil in the pore space of the target-state images, segmenting them.

One may notice that the voxels sandwiched between XG and grain were often segmented as oil phase. It is because the oil has intensity values between those of the grain and XG and is known as the partial volume effect. Pixels of phases with average intensity attenuation values between the materials composing the sample are often seen in phase boundaries of micro-CT tomograms like stained imagens (Ketcham and Carlson, 2001). To eliminate the partial volume, a novel workflow was proposed. It entails dilating the XG and grain phases then subtracting them from the original segmented phases. The intersection region formed by the subtraction operation and the sandwiched oil was removed from the oil and added in the XG phase. After, the Nagao filter was applied to remove eventual spots of XG in the oil and vice versa without altering the actual pore space. Figure 3.8 illustrates the methodology for eliminating the regions impacted by partial volume effect after the first drainage in experiment 1 of Study 2A.

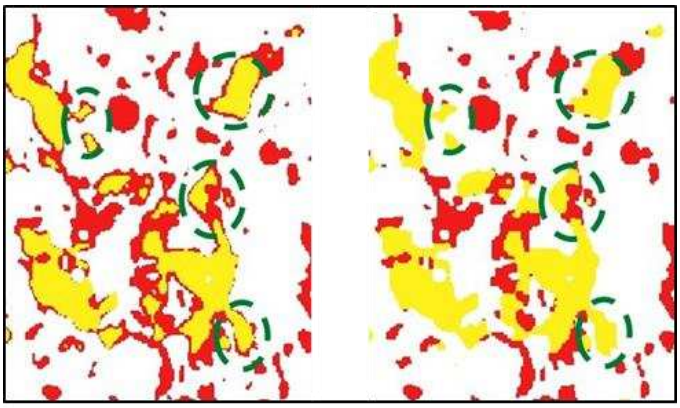

Figure 3.8: Before (a) and after (b) of partial volume effect removal in the pore space of core 1 (experiment 1, Study 2A). The yellow and red colors represent XG and oil, respectively.

The micropores were analyzed regarding their contribution to the total porosity. Micropores are pores smaller than the micro-CT resolution that, subsequently, are unresolved in the scan images. The porosity from the resolved pores was measured based on the grayscale intensity of the pores on PerGeos. In contrast, the porosity from the non-resolved pores was calculated by a linear correlation between the grayscale intensity of the image and the porosity values. Grain and pore contributions were tagged as 0 and 100%, respectively. Every voxel was then assigned a porosity value according to its grayscale intensity value.

In the end, the segmented fluid phase image and the reference-state scan were combined in a final four-phase labeled image. These images were analyzed about the XG, water, and oil saturation profiles, pore fluid occupancy maps, globule, and cluster size distributions.

Although unresolvable pores (micropores) contribute to the total pore volume, they were excluded from pore fluid occupancy image analysis. Only pores with resolvable fluid occupancies were analyzed to segment each fluid phase in the pore space and study oil-polymer displacements at pore levels.

The histograms of size distributions correlate the frequency as a percentage of the number of objects and their size in volume (μm^3). Objects are pores, clusters, and globules. They were ranged in 25 equally spaced bins, being the smallest and the biggest object size the limits of the scale. The volume axis was plotted in the logarithmic base, and the Gaussian model was fitted to the experimental data.

Figure 3.9 illustrates some snapshots of the image analyses workflow after the third oil injection in core 1. It shows the X-ray scans before and after the filter and registration steps, the extracted resolvable pores, and the segmented XG and oil after partial volume effect removal.

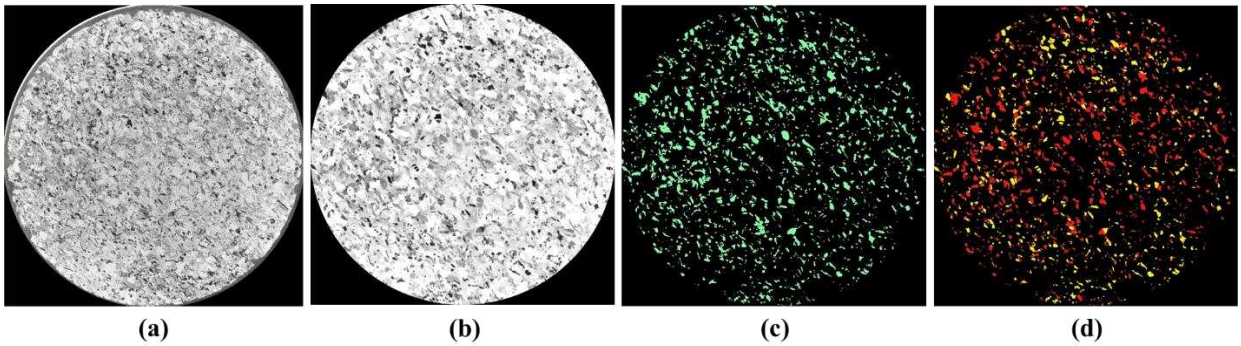

Figure 3.9: Image processing steps: (a) raw X-ray scan; (b) filtered and registered scan; (c) extracted pore space; and (d) fluid segmentation. The black color corresponds to pores, gray to micropores, white to grains, green to extracted resolved pores, yellow to XG, and red to oil.

4. Results

This section addresses and discusses the results of the data analysis of this thesis. It is divided into two main subsections corresponding to Studies 1 and 2. The first section presents the characterization of the materials and the results from the filtration tests of Study 1. It discusses the change in the medium permeability and the proposed model to estimate cake permeability. Then, the second section shows the description of cores and the main finding of pore fluid occupancy after drainage and imbibition cycles in Study 2. It shows the XG and oil saturation profiles, pore size occupancy, and size distribution of clusters and globules.

4.1 Filtration tests: Study 1

This subsection shows the characterization of XG and $CaCO_3$ solids, fluid and rheological properties of XG solutions and $CaCO_3$ suspensions, and porous ceramic filters. It also shows the evaluation of inner and external cake formations in Studies 1A and 1B, respectively.

4.1.1 Characterization of XG and $CaCO_3$ solids

The specific mass of XG and $CaCO_3$ was 1522.2 ± 0.3 and 2808 ± 2 Kg/m^3, respectively. SEM images at different magnifications show an elongated shape for the XG solids and a crystal and straight shape for $CaCO_3$, as Figures 4.1 and 4.2 illustrate.

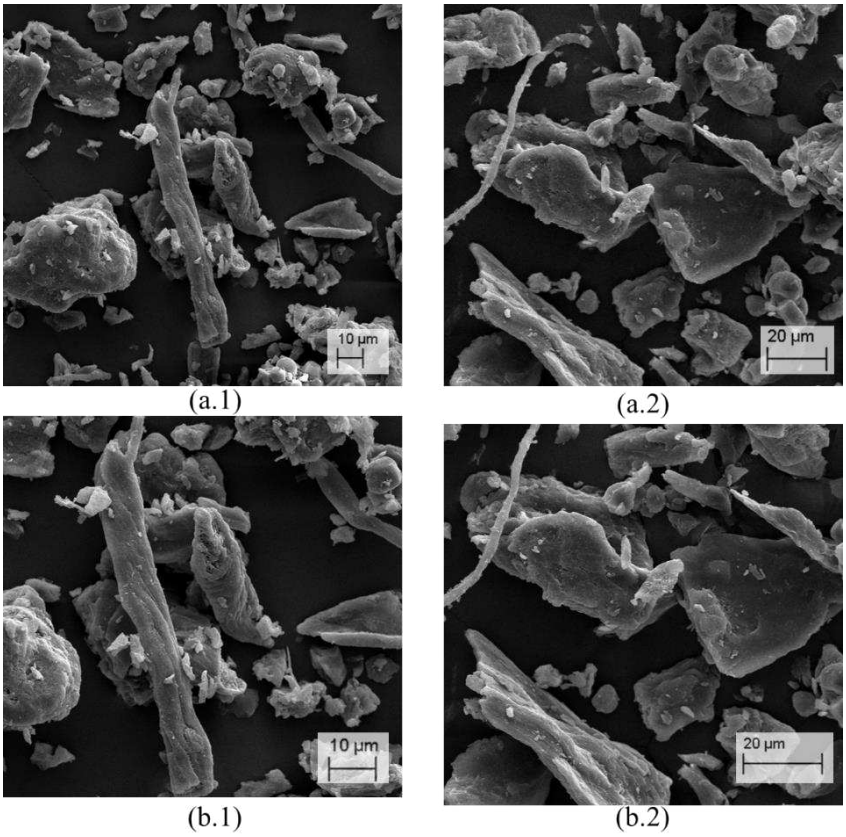

Figure 4.1: SEM images at (a) 1000 and (b) 1500 magnifications for XG solids.

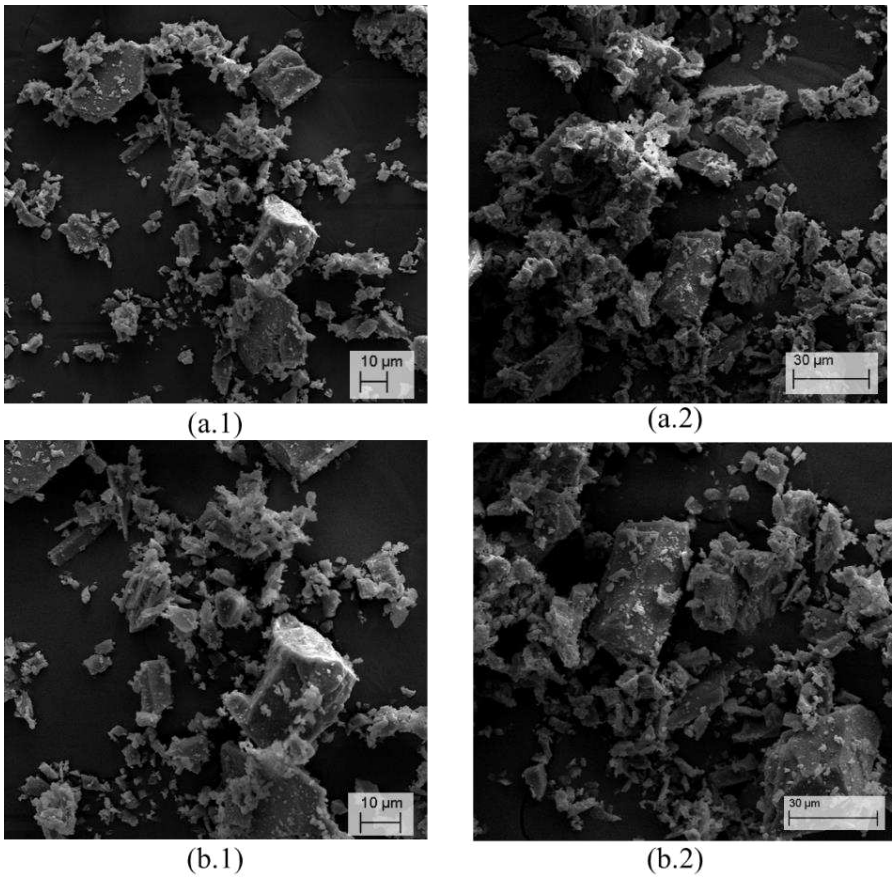

Figure 4.2: SEM images at (a) 1000 and (b) 1500 magnifications for $CaCO_3$ solids.

Regarding the particle size distribution of $CaCO_3$, Table 4.1 presents the fitting parameters ($d_{0.632}$ and n') and determination coefficients, r^2, for the RRB model, and Table 4.2 lists the particle fractions diameter of 0.1, 0.5, and 0.9. The experimental and fit plots are shown in Figure 4.3.

Table 4.1: Fitting parameters and determination coefficients for the RRB model for $CaCO_3$.

$d_{0.632}$ [µm]	n' [-]	r^2
27.8 ± 0.6	1.28 ± 0.07	0.999

Table 4.2: Particle fractions diameter of 0.1, 0.5, and 0.9 of $CaCO_3$.

Particle fraction [-]	0.1	0.5	0.9
d'_p [µm]	4.79	20.88	53.34

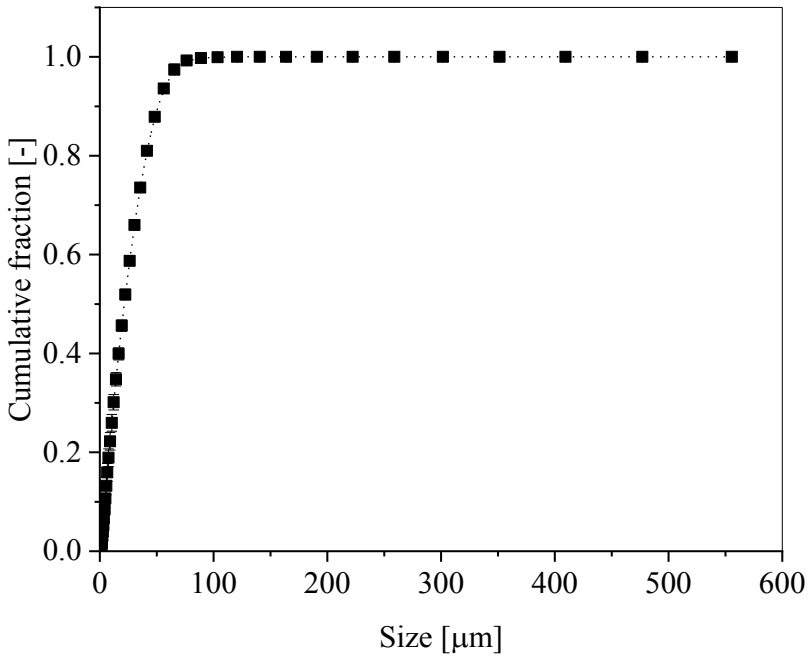

Figure 4.3: Experimental and fit plots of the particle size distribution of $CaCO_3$.

4.1.2 Fluid properties and rheological characterization of XG solutions and $CaCO_3$ suspensions

Table 4.3 lists the specific mass of water, XG solutions, and $CaCO_3$ suspensions. The water properties are from Perry et al. (1997). The increase in the polymer concentration increased the specific mass of both XG solutions and suspensions. It is in line with the expected results since the higher the polymer concentration, the higher the size and weight of the molecular structures of gels.

Table 4.3: Fluid properties.

	Water	XG [% m/m]			
		Solution		Suspension ($CaCO_3$)	
		0.2	0.4	0.2	0.4
Specific mass [Kg/m^3]	997.05	998.28 ± 0.05	999.73 ± 0.02	1110 ± 15	1140 ± 18
Viscosity [cP]	0.891				

Figure 4.4 shows the experimental data and the fitted plots for both XG solutions. Table 4.4 lists the fitting parameters and the determination coefficient for the power-law model. Statistically, the power-law showed a good fit to experimental data as the determination coefficient represents the variable response variation that the model predicts. In general, as higher the R-square value, the better the model explains the variability of the response data (Dodge, 2008).

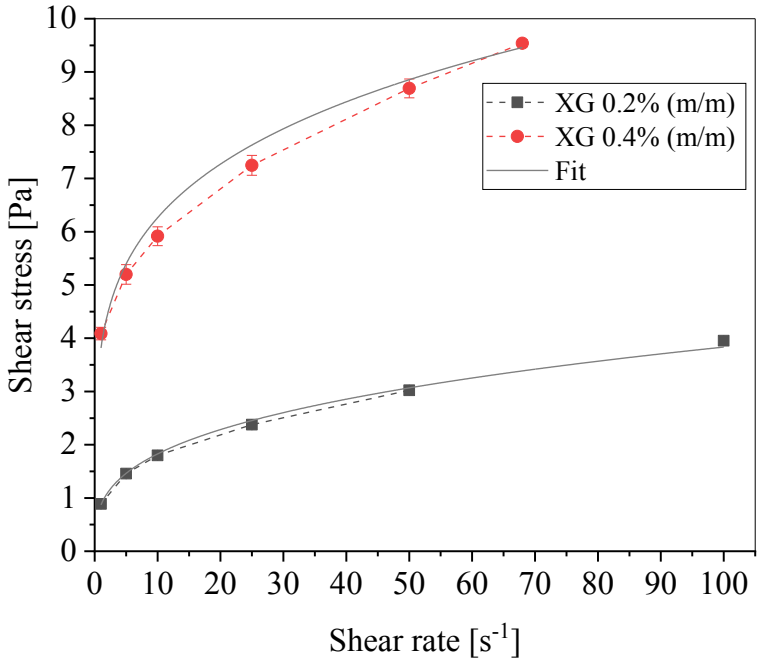

Figure 4.4: Rheograms of XG solutions 0.2 and 0.4% (m/m).

Table 4.4: Fitting parameters and determination coefficients for the power-law model for XG solutions 0.2 and 0.4% (m/m).

XG [% m/m]	m [Pa.s^n]	n [-]	r^2
0.2	0.87 ± 0.02	0.322 ± 0.007	0.997
0.4	3.8 ± 0.2	0.22 ± 0.01	0.989

The XG solutions showed a shear-thinning rheological behavior. The increment in the shear rate resulted in a non-linear response to the shear stress. The higher polymer concentration influenced both the values of behavior and consistency indexes. XG 0.4% (m/m) showed higher consistency and lower behavior indexes. The rise in polymer concentration increases the number of polymer molecules per unit of volume, increasing its resistance to flow. It is numerically shown by the consistency index, which is viewed as the value of apparent viscosity at the shear rate equal to one (Chhabra and Richardson, 2008). Moreover, the high number of polymer molecules in concentrated solutions boosts their pseudo-plasticity degree. Shear-thinning fluids have an index behavior of less than one, and as further it is from the unity, further it is from the Newtonian state (Chhabra and Richardson, 2008; Sorbie, 1991).

The test about the shear stress peak also reported the higher resistance of XG 0.4 than 0.2% (m/m) to flow. It is shown by the higher peaks of shear stress as soon as the flow starts, as Figure 4.5 illustrates.

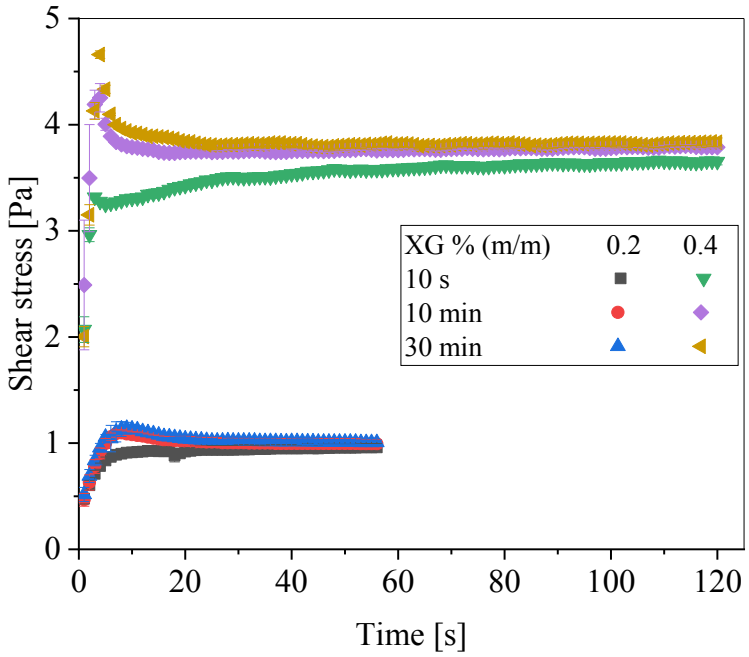

Figure 4.5: Shear stress peak for XG solutions 0.2 and 0.4% (m/m).

The resting time influenced the shear stress profile. The longer the resting time, the higher the initial shear stress response. It occurs because the resting time favors the folding of XG molecular chains. Thus, it increases the polymer degree of gelation and its resistance to flow. Once the flow achieved the steady-state condition, the shear stress value was the same despite the resting time. It indicates that the molecules are aligned in the flow direction, decreasing the fluid resistance to flow (Chhabra and Richardson, 2008; Machado, 2002).

Figure 4.6 exhibits the hysteresis curves for both XG solutions. The measured shear stress was higher in the increasing step of shear rate than in the decreasing step for the same shear rate. It featured the fluids as thixotropic, i.e., they are time-dependent on the shear rate. The hysteresis area quantified the influence of the polymer concentration in the required time for the fluid to achieve the steady-state condition. The hysteresis area was higher for XG 0.4 (19.12 Pa s^{-1}) than for XG 0.2% (m/m) (8.98 Pa s^{-1}). The hysteresis loop area has the dimension of energy required to break down the time-dependent structures per unit of volume of the sample (Roopa and Bhattacharya, 2009).

The rheograms of $CaCO_3$ suspensions are shown in Figure 4.7. The fitting parameters and the determination coefficient for the power-law model are listed in Table 4.5.

The $CaCO_3$ suspensions also presented shear-thinning behavior. However, as the presence of particles impairs the alignment of the fluid and its constituent molecules in the flow direction, higher values of both the consistency and behavior indexes were reported in the suspensions. As the shear rate increases, these disorganized structures form layers in the same plane as the shear, resulting in the shear-thinning behavior (Chhabra and Richardson, 2008).

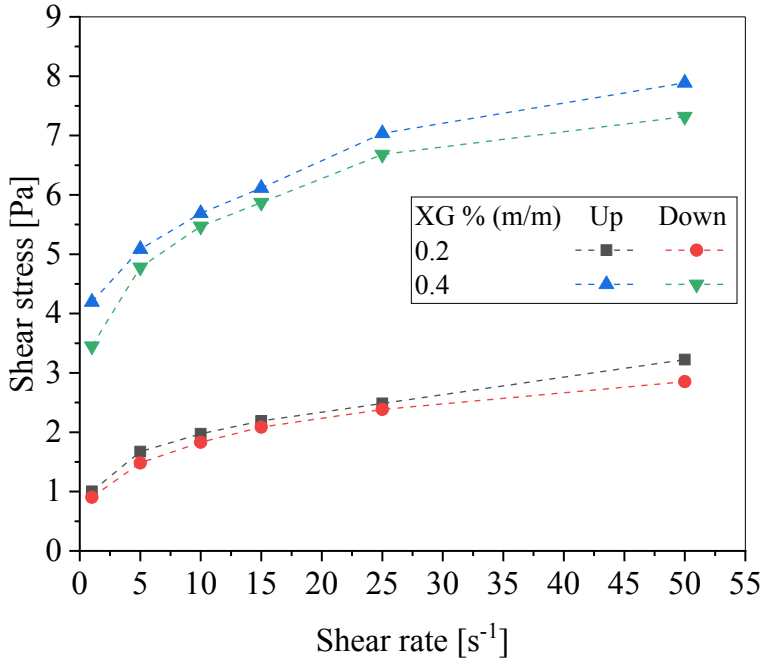

Figure 4.6: Hysteresis plots for XG 0.2 and 0.4% (m/m).

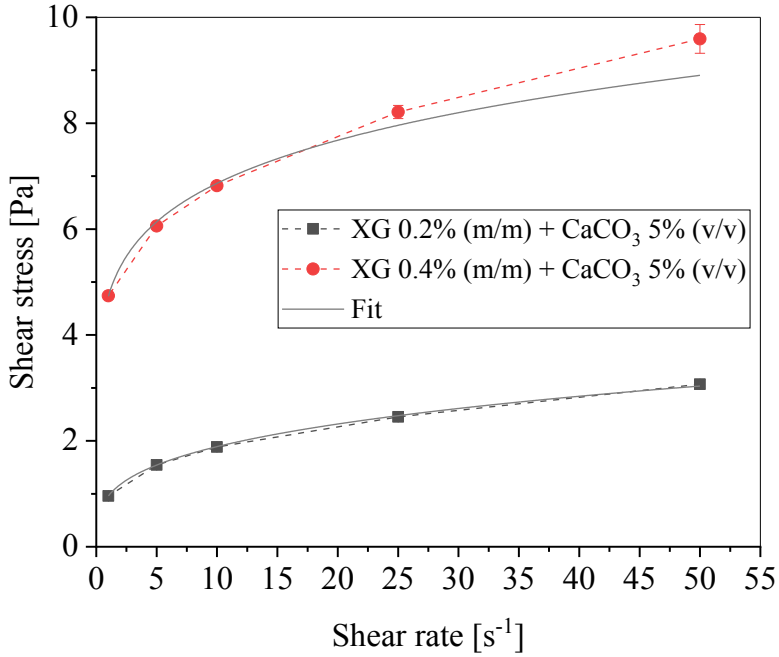

Figure 4.7: Rheograms of $CaCO_3$ suspensions.

Table 4.5: Fitting parameters and determination coefficients for the power-law model for $CaCO_3$ suspensions.

XG concentration in the $CaCO_3$ suspension	m [Pa.s^n]	n [-]	r^2
0.2	0.961 ± 0.005	0.294 ± 0.002	0.999
0.4	4.73 ± 0.03	0.162 ± 0.006	0.993

4.1.3 Porous ceramic filter characterization

The measured porosity values for the 50 and 120 µm ceramic filters were 0.354 and 0.257, respectively. Figures 4.8 and 4.9 show the SEM images of the superficial and lateral views of the ceramic filters, respectively. Pore size and porosity are key parameters that drive the fluid flow through porous media. Although the 50 µm membrane showed higher porosity, its smaller pores might not have connected enough as this sample also presented a lower permeability value.

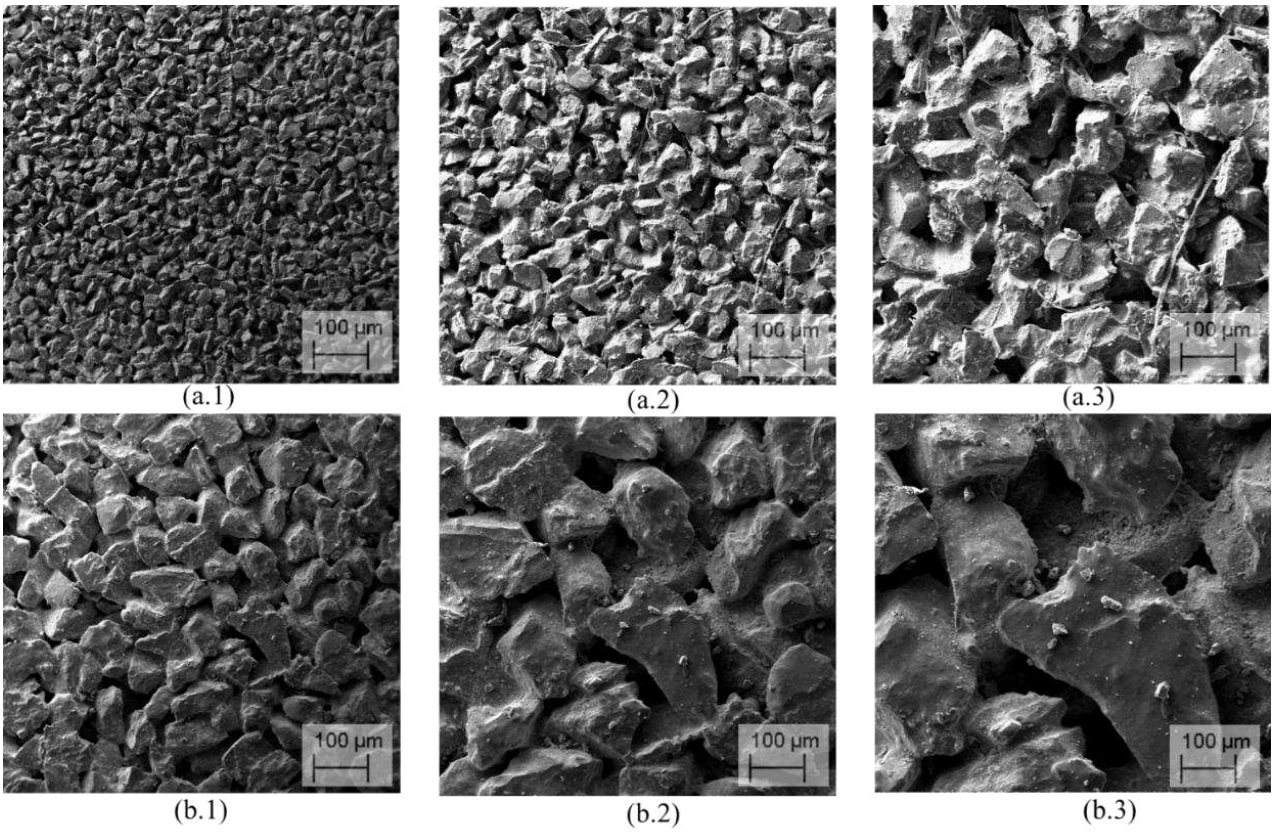

Figure 4.8: SEM image of the superficial view of the (a) 50 µm and (b) 120 µm ceramic filters at (1) 50, (2) 100, and (3) 150 magnifications.

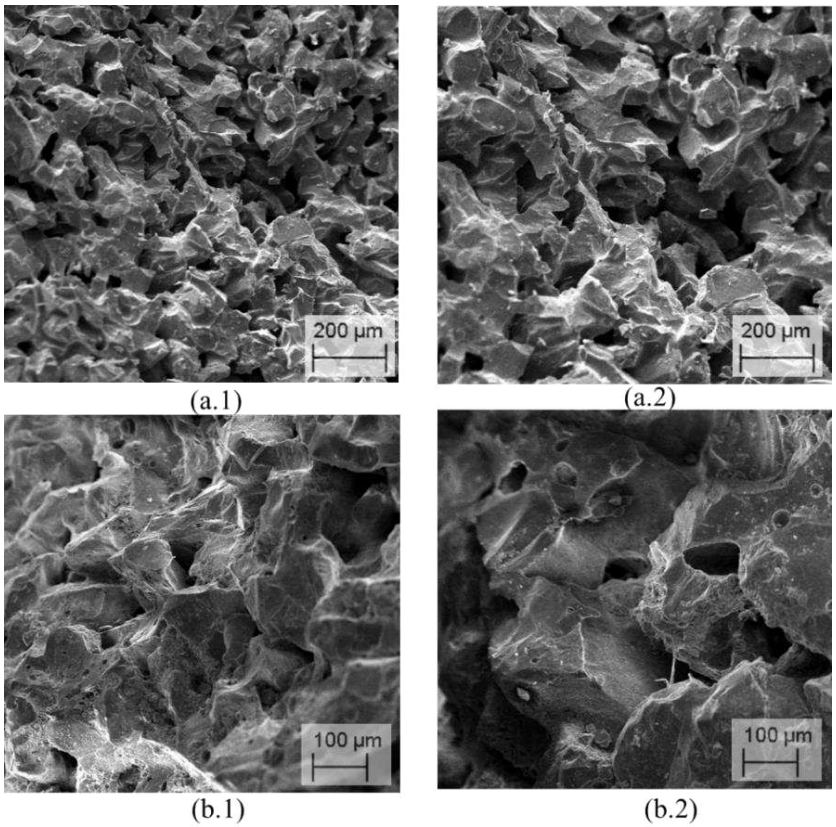

Figure 4.9: SEM images of the lateral view of the (a) 50 µm and (b) 120 µm ceramic filters at (1) 100 and (2) 150 magnifications.

4.1.4 Evaluation of inner cake formation: Study 1A

This subsection discusses the change in the porous media permeability and evaluates both the viscous and inertial effects in the polymer flow. The experimental condition of XG solution and ceramic filter is represented by XG *a_b* (*a* should be 0.2 or 0.4% (m/m), and *b* should be 50 or 120 µm). For example, XG 0.2% (m/m)_50 µm means the solution of XG 0.2% (m/m) flowing through the membrane of 50 µm.

Figure 4.10 shows the superficial velocity as a function of pressure drop per unit length for the XG solutions through the ceramic filters. The higher superficial velocities were reported in the porous medium with larger pores (120 µm). It agrees with the expected results since larger pores offer less frictional resistance to fluid flow. XG 0.2% (m/m) also presented higher superficial velocity at a lower pressure drop since it has lower resistance to flow. However, as the pressure drop increased, almost no significant difference was reported between the superficial velocity of XG 0.2 and 0.4% (m/m) for the same membrane.

The shape of the curves was a function of pressure. They presented a curvature shape for lower pressures and a linear trend for higher pressures. This behavior was more evident for XG 0.4% (m/m)_50 µm. The opposite was found for XG 0.2% (m/m)_120 µm. This change was attributed

to the tendency of shear-thinning solutions be less viscous and closer to a Newtonian behavior at a high pressure.

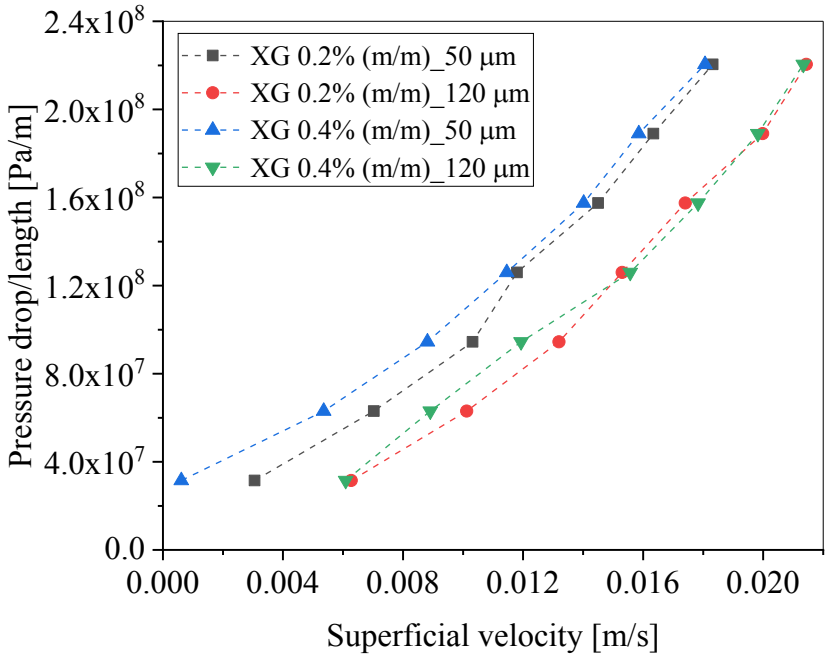

Figure 4.10: Superficial velocity of polymeric flows as a function of a pressure drop per unit length.

The data set of superficial velocity and pressure drop per unit length was used to estimate the permeability of the ceramic filters after polymer flow using Darcy's law and the Forchheimer equation. Table 4.6 presents the values for the non-Darcy coefficients described by M1, M2, and M3. Lower non-Darcy coefficients, i.e., inertial resistance factor, were reported in the membrane formed by larger pores. It is in line with Takhanov (2011) since the fluid path in these media is less impeded. The highest coefficient values corresponded to M1.

Table 4.6: Non-Darcy coefficients.

Membrane	Non-Darcy coefficient [m^{-1}]		
[µm]	M1	M2	M3
50	$4.27x10^8$	$6.79x10^4$	$2.39x10^5$
120	$2.72x10^8$	$1.48x10^4$	$8.91x10^4$

The permeability values obtained using the non-Darcy coefficients described by M2 and M3 in the Forchheimer equation were the same as those obtained using Darcy's law. It shows that when M2 and M3 describe the polymeric flows, the account of higher inertial resistance factors resembles the fluid closer to the one described by Darcy's law, where viscous forces dominate. In this case, the estimated medium permeability and apparent viscosity obtained by Darcy's law and Forchheimer equation using M2 and M3 were the same. In contrast, the inertial effects were not

neglected when the non-Darcy coefficient was described by M1. In this case, the viscous force was not the only effect in the polymeric flow, and higher values of medium permeability and apparent viscosity were reported.

Figures 4.11 and 4.12 illustrate the plot of the filter media permeability for each experimental condition as a function of pressure drop per unit length for Darcy's law and Forchheimer equation, respectively. From now on in this section, both the filter medium permeability and apparent viscosity obtained by Darcy's law are referred to those obtained from Darcy's law itself and those obtained from the Forchheimer equation when M2 and M3 were used as the non-Darcy coefficient. The Forchheimer equation, in turn, refers to the Forchheimer equation when M1 was used.

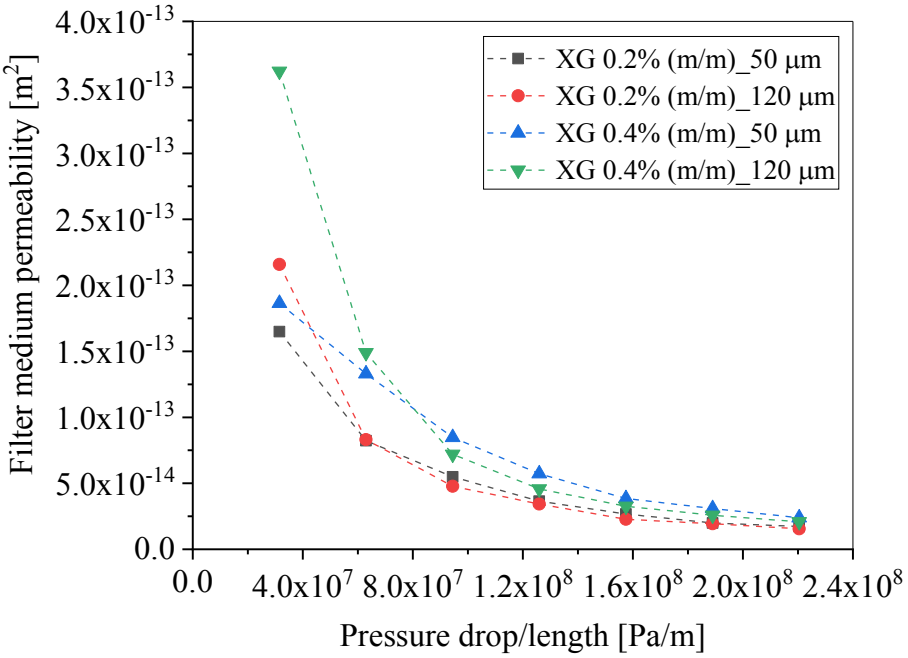

Figure 4.11: Estimated filter medium permeability after polymeric flow for different pressure drop per unit length using Darcy's law.

The permeability in both ceramic filters decreased as a function of pressure drop for all experimental conditions. It is explained by polymer retention in the interstices of the porous matrix. The retained polymer blocks some pore throats, decreasing the effective fluid path for polymer flow. The permeability reduction can be interpreted as reducing the effective pore diameter in the porous medium caused by polymer retention (Ferreira, 2019). The range of decrease in the permeability calculated by Darcy's law is wider than the ones calculated by Forchheimer. In the latter, most of the filter medium permeability values presented a similar order of magnitude, and this slight variation may have a low impact on field application.

The membrane of 120 µm still presented higher permeability than the 50 µm after both XG 0.2 and 0.4% (m/m) polymer flows at lower pressure drops for Darcy's law and Forchheimer equation. In the scenario described by Darcy's law, as the pressure drop increases, the force to push the

solutions through the media is higher, fully saturating them with polymer. That is why the difference between the reported permeabilities shortens as a function of pressure. At the highest pressure, there was no significant difference between them. In contrast, the scenario described by the Forchheimer equation showed a small variation in the permeability of the ceramic filter of 50 µm to 120 µm. In this case, there was not an effective convergence between the permeability values of all experiments.

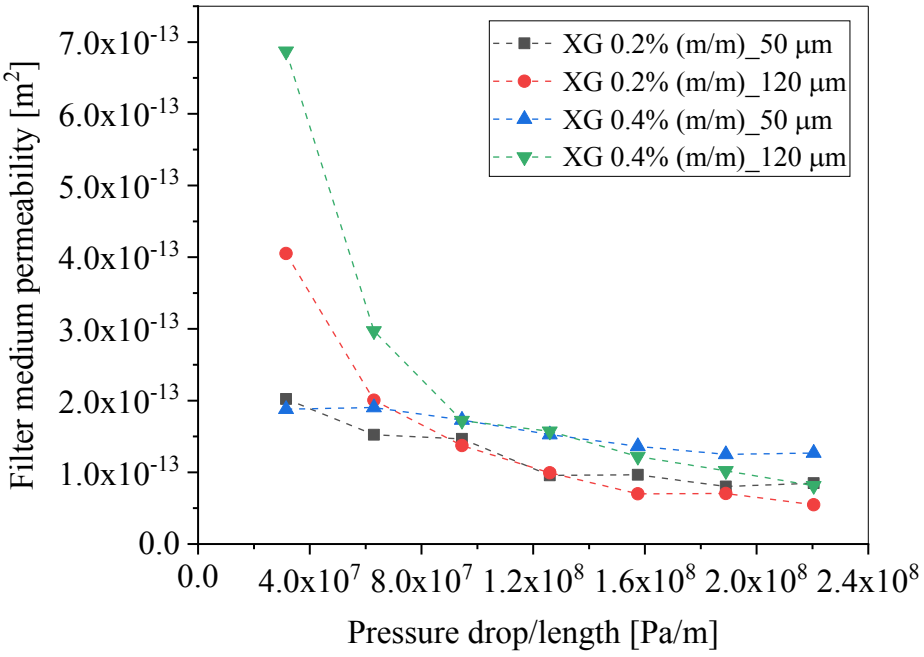

Figure 4.12: Estimated filter medium permeability after polymeric flow for different pressure drop per unit length using the Forchheimer equation.

All estimated values were in the 10^{-13} order of magnitude. The lowest range of filter medium permeability corresponded to the XG 0.4% (m/m)_50 µm described by the Forchheimer equation. The higher polymer concentration and the small pore bodies in this membrane impaired the fluid flow. In this scenario, physical adsorption and polymer entrapment might be the most important types of polymer retention.

After the flow of XG solutions at lower pressure drops, the filter medium permeability presented higher values when it was percolated by the more concentrated solution. Once again, it might be explained by the adsorbed polymer layer in the external surface area of membranes.

Once the permeability of the filter medium after polymer flow was estimated, the apparent viscosity of XG inside the pore space was also estimated. By putting numbers in perspective, the consistency and behavior indexes and the coefficient of determination for the power-law fitting for each experiment are listed in Tables 4.7 and 4.8 for XG 0.2 and 0.4% (m/m) through the membranes of 50 and 120 µm, respectively. The decrease in value of these parameters indicates

that part of polymer molecules was retained in the pore space, reproducing the inner filter cake formation.

Table 4.7: Fitting parameters and determination coefficients for the power-law model for the filtrate of XG 0.2% (m/m) through the membranes of 50 and 120 µm.

	XG 0.2% (m/m)_50 µm			XG 0.2% (m/m)_120 µm		
ΔP (x10^5) [Pa]	m [Pa.s^n]	n [-]	r^2	m [Pa.s^n]	n [-]	r^2
Reference	0.87 ± 0.02	0.322 ± 0.007	0.997	0.87 ± 0.02	0.322 ± 0.007	0.997
2	0.68 ± 0.01	0.330 ± 0.005	0.999	0.86 ± 0.02	0.319 ± 0.006	0.999
4	0.696 ± 0.009	0.320 ± 0.004	0.999	0.798 ± 0.002	0.308 ± 0.001	0.999
6	0.65 ± 0.01	0.329 ± 0.004	0.999	0.747 ± 0.002	0.307 ± 0.002	0.999
8	0.662 ± 0.007	0.322 ± 0.003	0.999	0.66 ± 0.02	0.320 ± 0.006	0.999
10	0.67 ± 0.01	0.312 ± 0.004	0.999	0.622 ± 0.006	0.309 ± 0.004	0.999
12	0.67 ± 0.01	0.305 ± 0.004	0.999	0.584 ± 0.008	0.318 ± 0.004	0.999
14	0.65 ± 0.01	0.309 ± 0.005	0.999	0.60 ± 0.01	0.315 ± 0.004	0.999

Table 4.8: Fitting parameters and determination coefficients for the power-law model for the filtrate of XG 0.4 % (m/m) through the membranes of 50 and 120 µm.

	XG 0.4% (m/m)_50 µm			XG 0.4% (m/m)_120 µm		
ΔP (x10^5) [Pa]	m [Pa.s^n]	n [-]	r^2	m [Pa.s^n]	n [-]	r^2
Reference	3.8 ± 0.2	0.22 ± 0.01	0.989	3.8 ± 0.2	0.22 ± 0.01	0.989
2	2.99 ± 0.03	0.201 ± 0.003	0.999	3.55 ± 0.04	0.196 ± 0.005	0.997
4	3.25 ± 0.03	0.200 ± 0.005	0.996	3.37 ± 0.05	0.214 ± 0.004	0.998
6	3.02 ± 0.03	0.214 ± 0.003	0.999	3.79 ± 0.06	0.188 ± 0.005	0.997
8	3.05 ± 0.05	0.212 ± 0.005	0.998	3.09 ± 0.03	0.198 ± 0.003	0.999
10	3.167 ± 0.004	0.197 ± 0.002	0.999	3.010 ± 0.001	0.196 ± 0.002	0.999
12	2.95 ± 0.02	0.207 ± 0.003	0.999	2.924 ± 0.008	0.202 ± 0.001	0.999
14	2.97 ± 0.03	0.200 ± 0.005	0.997	2.97 ± 0.03	0.202 ± 0.002	0.999

The rheograms of the filtrates are shown in Figure 4.13. The filtrates showed a decrease in the shear stress to shear rate for all experimental conditions in relation to the XG solutions before filtration (reference state). In the ceramic filter of 50 µm, the rheogram curves corresponding to the filtrate were closer to each other than those in the 120 µm.

Although polymer retention increased as a function of pressure drop in both filters, this increment was slower in the ceramic filter of 50 µm. One may assume that mechanical entrapment and polymer adsorption was the predominant polymer retention mechanisms in the filter of 50 µm. In the filter of 120 µm, in turn, besides these mechanisms, the hydrodynamic effect also played an important role in XG retention, because the highest XG flow rates were reported in 120 µm. As the superficial velocity increases, the polymer molecules tend to be trapped in the polymer layer previously settled in the pore wall, increasing the amount of polymer retention (Sorbie, 1991).

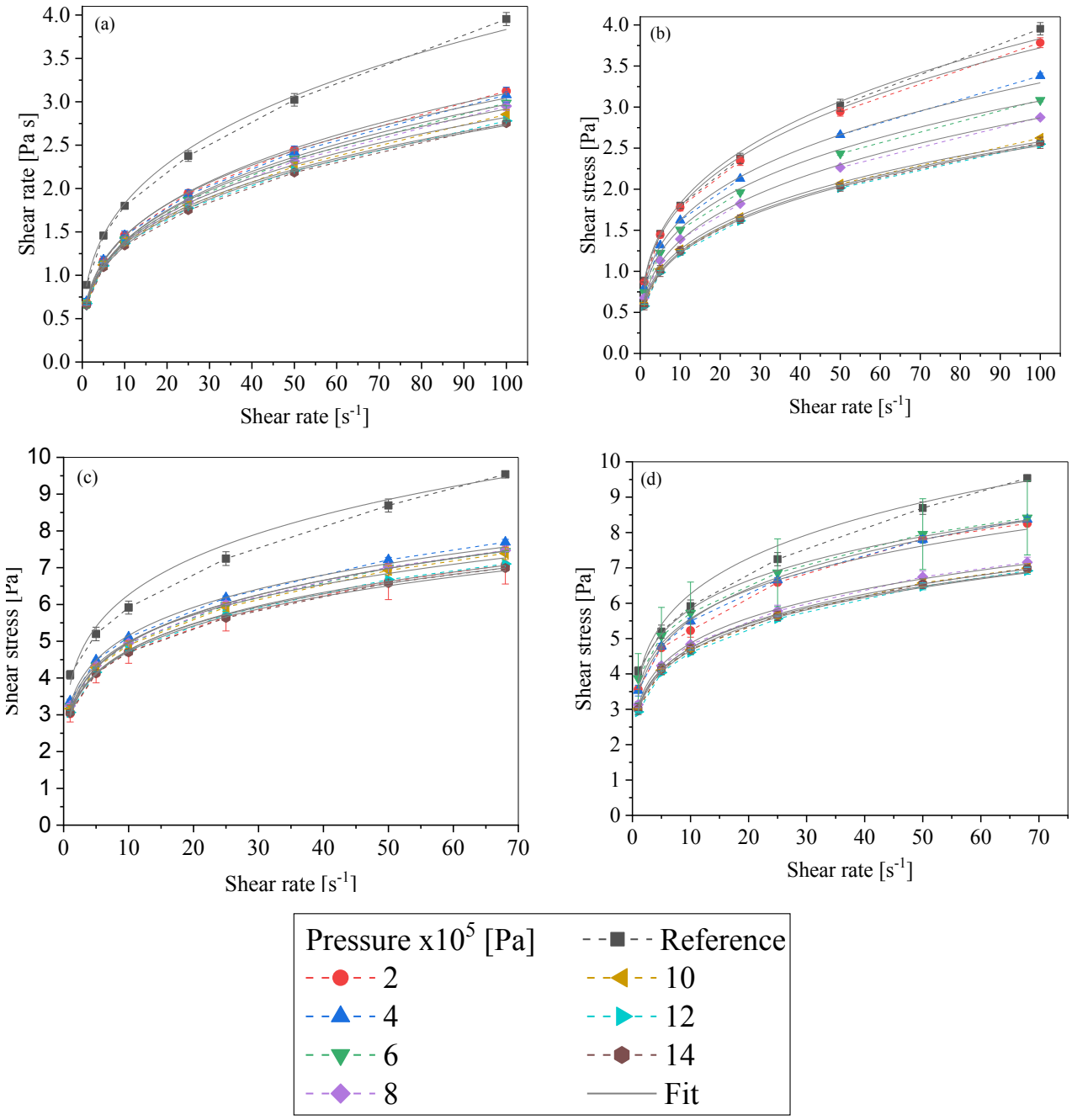

Figure 4.13: Rheogram of the filtrate for (a) XG 0.2% (m/m)_50 µm, (b) XG 0.2% (m/m)_120 µm; (c) XG 0.4% (m/m)_50 µm, and (d) XG 0.4% (m/m)_120 µm.

Using the estimated values of filter medium permeability and rheological fitting parameters, the apparent viscosity of XG inside the ceramic filter could be estimated. Figures 4.14 and 4.15 show the plot of apparent viscosity as a function of pressure drop per unit length for each experimental condition using Darcy's law and the Forchheimer equation, respectively. As expected, the increase in the pressure drop decreased the apparent viscosity in all scenarios, and the filtrate of XG 0.4% (m/m) still presented higher viscosity values. The broad difference in the

apparent viscosity was reported for lower pressures. They might not be enough to fully develop the flow through pore space roughness and size distribution. The hydrodynamic effect of polymer retention is here noticed by the lower viscosity of the filtrate from the ceramic filter of 120 µm.

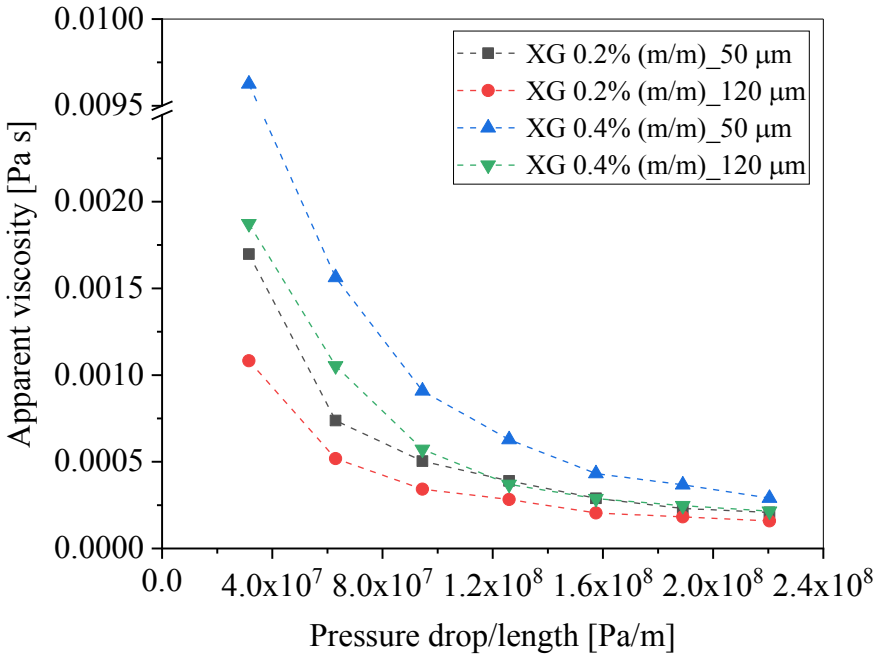

Figure 4.14: Estimated apparent viscosity of XG as a function of pressure drop per unit length using Darcy's law.

As the Forchheimer equation considers both the viscous and inertial forces in the polymeric flow, the viscous parameters in this model were smaller than the ones estimated by Darcy's law (Table 4.9). In this case, the total forces were split between the viscous and inertial ones. The inertial parameter, in turn, was higher in the ceramic filter of 50 µm for all non-Darcy coefficients—as Table 4.10 illustrates—because the small pores hamper the full development of fluid flow through the pore space. The fluid inside the matrix pores presented higher viscosity than in the medium formed by larger pores. Besides, the inertial effect was not influenced by the XG concentration. This effect results from the combination of petrophysical characteristics of pore space and fluid density. As both XG solutions had similar densities, the key factors influencing the inertial effect calculation were pore size and medium permeability.

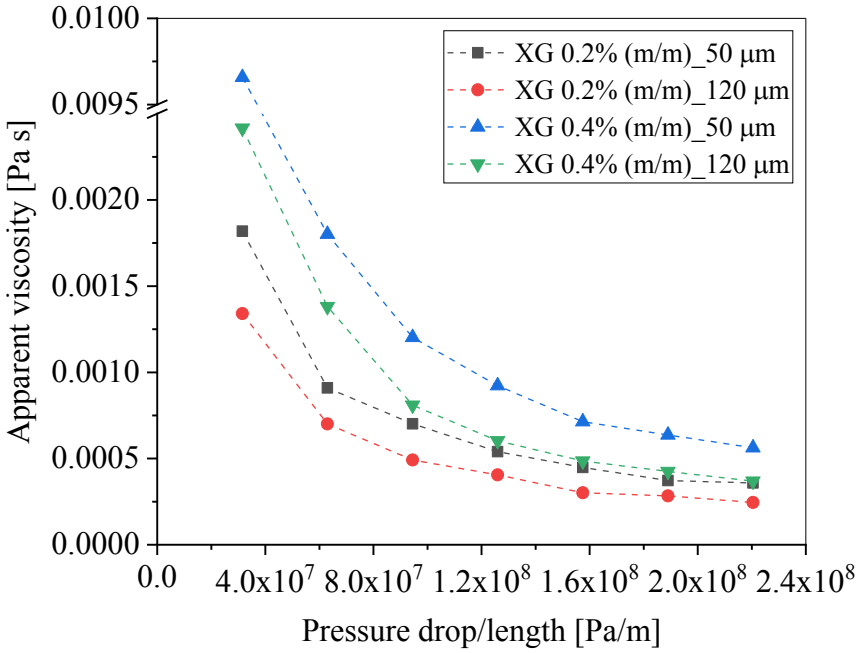

Figure 4.15: Estimated apparent viscosity of XG as a function of pressure drop per unit length using the Forchheimer equation.

Table 4.9: Viscous parameter estimated by Darcy's law and Forchheimer equation for each experimental condition.

Pressure $x10^5$ [Pa]	(Viscous parameter) $x10^{10}$ [Pa s/ m^2]							
	XG 0.2% (m/m) 50 µm		XG 0.2% (m/m) 120 µm		XG 0.4% (m/m) 50 µm		XG 0.4% (m/m) 120 µm	
	Darcy	Forchheimer	Darcy	Forchheimer	Darcy	Forchheimer	Darcy	Forchheimer
2	1.03	0.90	0.50	0.33	5.16	5.14	0.52	0.35
4	0.90	0.60	0.62	0.35	1.18	0.95	0.71	0.47
6	0.92	0.48	0.72	0.36	1.07	0.70	0.79	0.47
8	1.07	0.57	0.82	0.41	1.10	0.61	0.81	0.38
10	1.08	0.47	0.90	0.43	1.12	0.52	0.88	0.40
12	1.16	0.47	0.95	0.40	1.19	0.51	0.96	0.42
14	1.20	0.42	1.03	0.45	1.22	0.43	1.03	0.45

Table 4.10: Inertial parameter estimated by different non-Darcy coefficients for each experimental condition.

Model	(Inertial parameter) $x10^7$ [Kg/m^4]			
	XG 0.2% (m/m) 50 µm	XG 0.2% (m/m) 120 µm	XG 0.4% (m/m) 50 µm	XG 0.4% (m/m) 120 µm
M1	42,600	27,200	42,600	27,200
M2	6.78	1.48	6.79	1.48
M3	23.9	8.89	23.9	8.90

In this study, the inertial effects play an important role in the characterization of fluid flow when the non-Darcy coefficient described by M1 was used. In this case, there were two orders of magnitude higher than the viscous effect. However, using M2 and M3, the inertial effect was lower than the viscous effect, and the fluid flow was described as it is by Darcy's law.

The Reynolds number was also analyzed to characterize the XG flow in both ceramic filters. Tables A.1, A.2, and A.3 (section A.2 of the Appendix) list these numbers for the different approaches of flow in porous media described by Equations 2.21, 2.22, and 2.23, respectively, for all experimental conditions. As expected, larger pores and the increment in the pressure drops increased the superficial velocity of the solution for the same polymer concentration, resulting in a higher Reynolds number. Based on the thresholding values for interstitial Reynolds number, the inertial effect was reported for higher pressure drops for the membrane of 50 μm for both XG 0.2 and 0.4% (m/m). In the membrane of 120 μm, however, the inertial effect was noticeable from intermediate pressure drops and it was even higher due to the higher fluid velocity and larger pores of this medium (Huang and Ayoub, 2006).

Finally, the evaluation of the model that best described the polymeric flow through the ceramic filters was based on the smallest value of the relative error of pressure drop per unit length. Darcy's laws presented a smaller relative error (10^{-3} order of magnitude), better describing the flows through the membranes.

4.1.5 Evaluation of external cake formation: Study 1B

This subsection discusses the estimated values of external cake permeability and the change in the ceramic filter permeability by $CaCO_3$ suspensions. The experimental conditions of each test of $CaCO_3$ suspensions in different XG solutions flowing through the membranes are also represented by the notation XG *a_b* (*a* being 0.2 or 0.4% (m/m), and *b* 50 or 120 μm).

First, the proposed model to estimate the permeabilities of the external cake and the ceramic filters after the suspension flow was evaluated. For this, the estimated and experimental values of the suspension filtrate volume as a function of time were compared. These values were in good agreement, as Figure 4.16 shows. The standard deviation values of estimated permeabilities of the cake and the membrane and the objective function were 10^{-24} order of magnitude, indicating that the optimization procedure was successfully done. Section A.3 of the Appendix lists the experimental parameters used in the model in Tables A.4 and A.5 and the estimated permeabilities in Tables A.6 and A.7 for XG 0.2 and 0.4% (m/m), respectively.

The filtrate volume of XG 0.2 was higher than 0.4% (m/m). As all suspensions had the same volumetric solid concentration, this high filtrate volume was attributed to the lower polymer concentration in XG 0.2% (m/m). A lower XG concentration results in lower viscous resistance for this suspension to flow. It was also observed a higher filtrate volume in the ceramic filter of 50 μm than in 120 μm. Although the reference permeability of the filter of 50 μm is lower, it has a higher porosity. Thus, one may notice that these pores might be mostly arranged like bundles,

connecting the inlet to the outlet surface of the membrane rather than being connected among them inside the pore space. A wider range of filtrate volume was also reported in the filter of 50 µm for both XG solutions, being even more noticeable for XG 0.4% (m/m). The lowest filtrate volume was reported for XG 0.4% (m/m)_50 µm. These findings are related to the narrow pore bodies of the membrane of 50 µm and the higher polymer concentration that makes the suspension flow more sensitive to pressure drop due to frictional and rheological resistances, respectively.

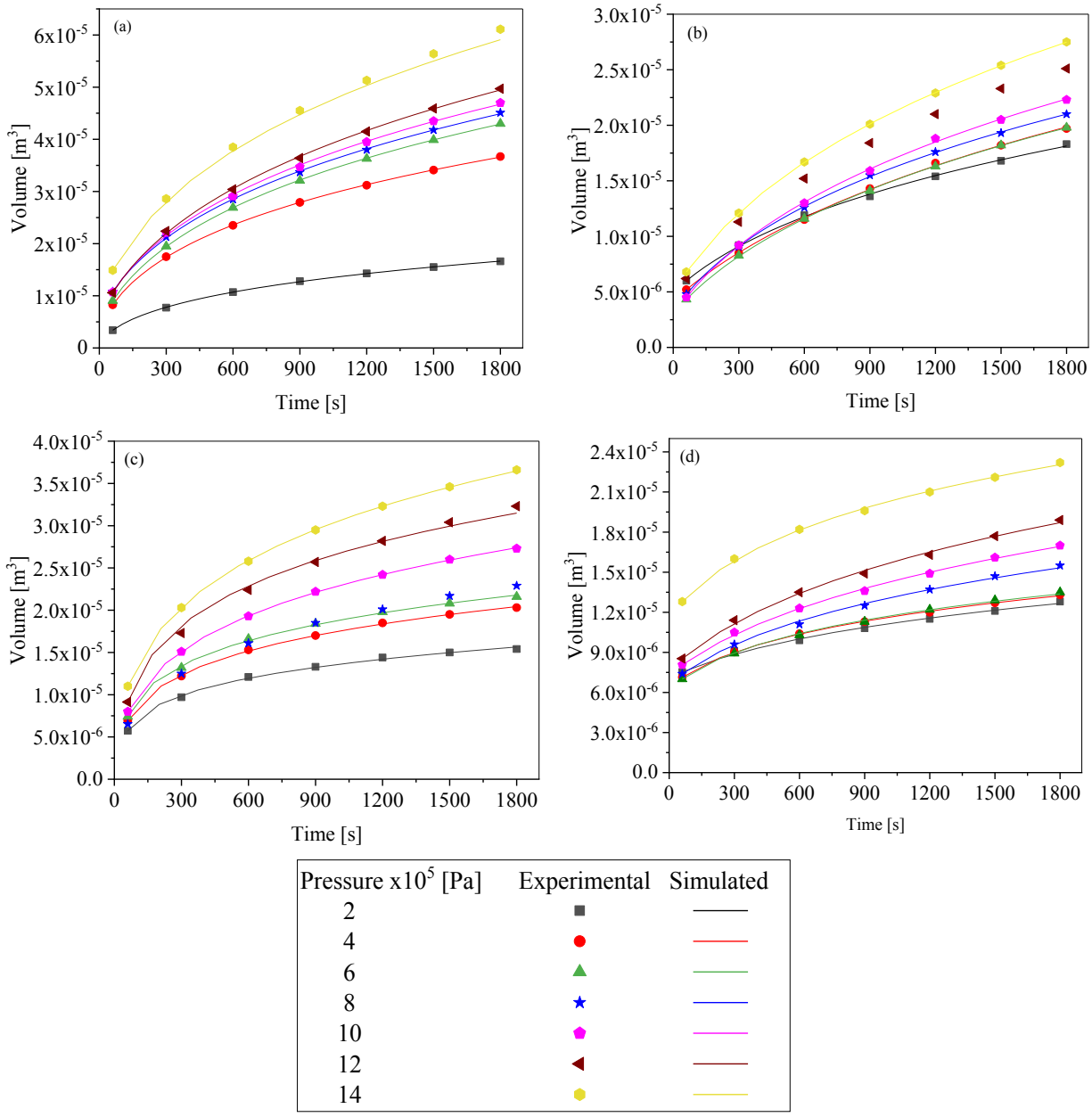

Figure 4.16: Experimental and estimated filtrate volume of (a) XG 0.2% (m/m)_50 µm, (b) XG 0.2% (m/m)_120 µm; (c) XG 0.4% (m/m)_50 µm, and (d) XG 0.4% (m/m)_120 µm for different pressure drops.

Figure 4.17 illustrates the filtrate sample of XG 0.2% (m/m)_50 µm at $8x10^5$ Pa. For all experimental conditions of suspension rheology and ceramic filter, the filtration rate decreased as a function of time. The filtrate became more clarified, indicating that part of the solid was retained in the cake and membrane. The filtrates from the ceramic filter of 120 µm were less translucid due to their higher solid content.

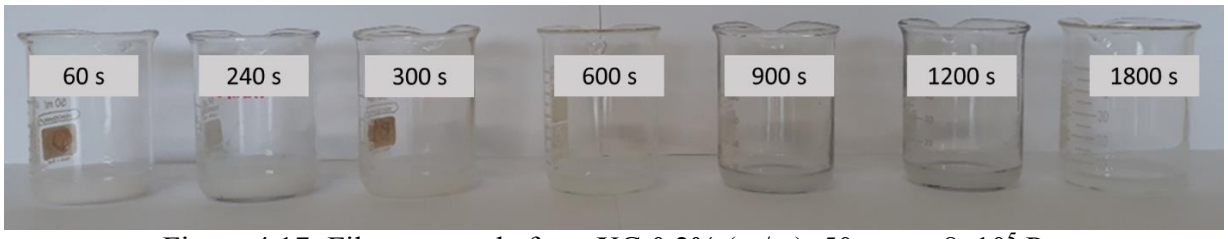

Figure 4.17: Filtrate sample from XG 0.2% (m/m)_50 µm at $8x10^5$ Pa.

After the suspension flow, the filter medium permeability was smaller than when it was percolated only by XG solutions. It was expected since the permeability reduction was attributed to polymer retention and pore-clogging by $CaCO_3$. Figure 4.18 illustrates the estimated medium permeability as a function of pressure drop for the different experimental conditions. The medium permeability decreased as the pressure drop increased since higher pressure drops pushed the suspensions through the pore space, filling the pore bodies and throats. Changes in the medium permeability were also reported to be less sensitive at high pressures. In this pressure range, particle deposition in the matrix pore of the medium achieved its highest clogging effect. Thus, solid deposition started to occur on the inlet surface of the membrane as a cake. In this stage, the spurt loss effect also occurred faster.

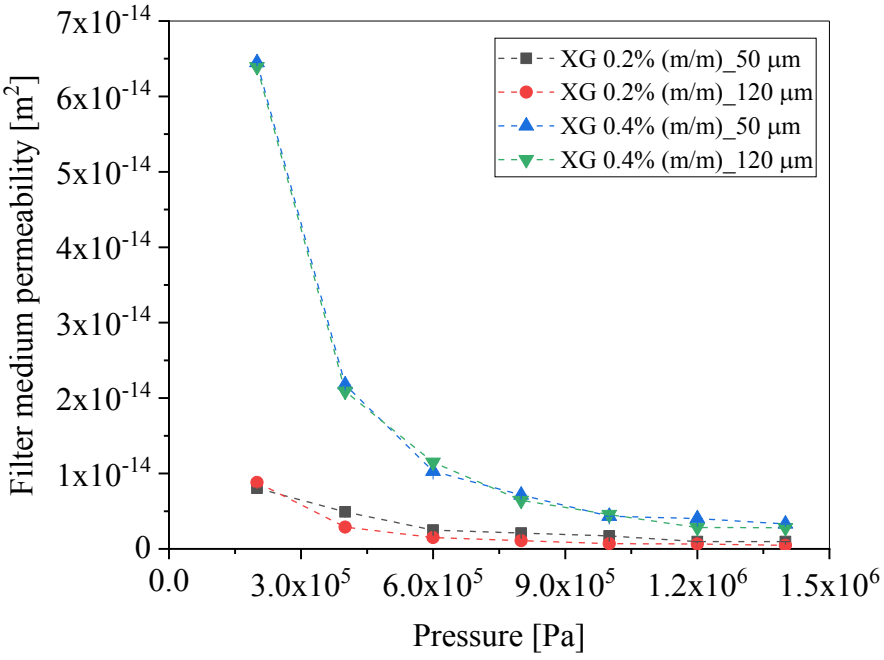

Figure 4.18: Estimated filter medium permeability after suspension flows for different pressure drops.

The suspension rheology strongly affected the medium permeability. Both ceramic filters presented lower permeability when percolated by XG 0.2% (m/m). It was justified by the lower viscous resistance of this solution to flow through the pore space. As higher filtrate volume percolates pore structures, pore bodies and throats become clogged by the solid deposition, decreasing the permeability of the medium. Furthermore, the suspension rheology seems to influence fluid percolation and cake formation more than the petrophysics of the membrane, because the 50 and 120 µm filters presented similar permeabilities after being percolated by the same XG concentration for the same pressure drop.

Lastly, although the decrease in the filter medium permeability is a function of pressure drop, most of them remained in the same order of magnitude, which might mean a small variation in field scale.

Figure 4.19 illustrates the estimated cake permeability as a function of pressure drop for the different experimental conditions. Cake permeability for both polymer concentrations decreased as a function of pressure drop. Except for XG 0.4% (m/m)_50 µm, cake permeabilities decreased one order of magnitude as the pressure drop increased. This range of variation was wider for the cake formed by XG 0.4% (m/m)_120 µm, which presented the highest permeability at the lowest pressure drop ($2x10^5$ Pa).

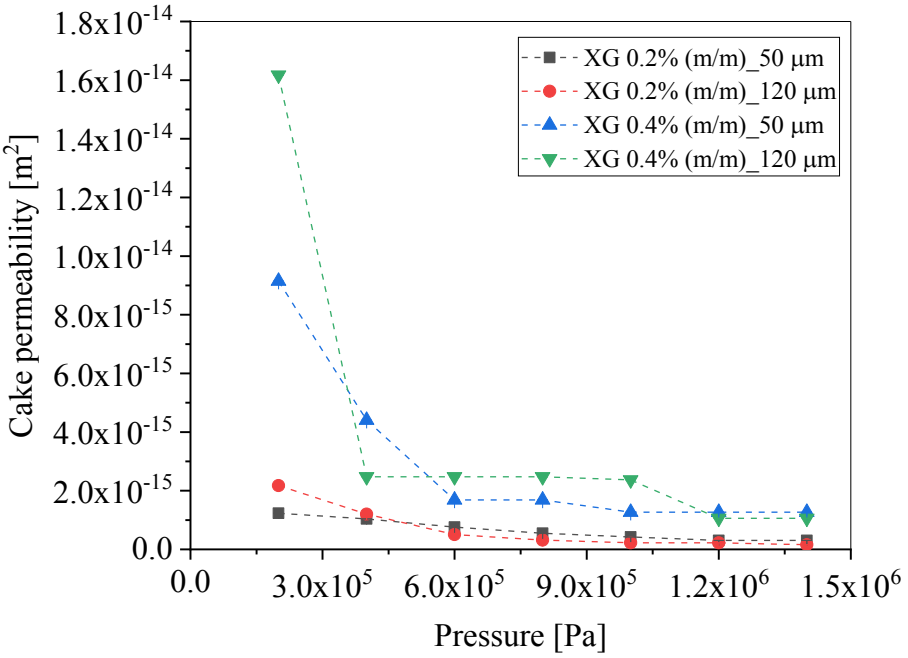

Figure 4.19: Estimated external cake permeability after suspension flows for different pressure drops.

The $CaCO_3$ suspensions in XG 0.4% (m/m) formed the most permeable cakes, because solids tend to be in suspension in high viscous solutions. The polymer chains in these solutions tend to be tangled, trapping solid particles and thus increasing the suspension resistance to flow. The

higher permeability of these cakes was also justified by their higher porosity values than those formed by XG 0.2% (m/m), as is shown in Tables A.6 and A.7. The cakes formed by XG 0.4% (m/m)_120 μm were more permeable than those formed in the filter of 50 μm. It was attributed to the larger difference in the pore bodies of the 120 μm membrane than the average particle size of $CaCO_3$, decreasing the solid retention on the surface of the membrane. Higher porosity means more void space that favors fluid flow. The relation between high porosity and high permeability of cake was also stated by Ferraz (2014) in HTHP filter tests with $CaCO_3$ suspension in XG and CMC solutions.

In contrast, the cakes formed from suspensions of XG 0.2% (m/m) presented similar permeability for both ceramic filters. As XG 0.2 % (m/m) has less viscous resistance to flow, more solid particles and polymer chains might be retained in the membrane surface, building the cake.

Besides, cake permeability was less variable in the high pressure range for all experimental conditions. As the pressure drop increased, the filtrate volume and the solid deposition on the surface of membranes, consequently, also increased. This was numerically reported by the slight increase in cake thickness as a function of pressure, as Table A.4 shows. Although cake thickness kept occurring for each increment in pressure drop, it was less noticeable from $6x10^5$ Pa. One may assume that cakes approached their final configuration up to this pressure.

Cake permeability might have changed if a longer experimental time had been performed and/or even higher pressure drops had been applied. Ferraz (2014) reported an average decrease of one order of magnitude in the permeability of cakes of non-Newtonian suspensions as the pressure drop increased from 3.45 to $6.90x10^6$ Pa.

The specific cake and medium resistances were also evaluated, as listed in Table 4.11.

Table 4.11: Specific cake and medium resistances for XG 0.2 and 0.4% (m/m) and $CaCO_3$ through the membranes of 50 and 120 μm.

ΔP ($x10^5$) [Pa]	α ($x10^{11}$) [m/Kg]				R_m ($x10^{12}$) [m^{-1}]			
	XG 0.2 50 μm	XG 0.2 120 μm	XG 0.4 50 μm	XG 0.4 120 μm	XG 0.2 50 μm	XG 0.2 120 μm	XG 0.4 50 μm	XG 0.4 120 μm
2	10.20	6.07	1.95	1.84	0.79	0.72	0.09	0.09
4	8.97	9.79	3.23	9.59	1.29	2.20	0.29	0.30
6	1.10	24.00	7.05	8.99	2.55	4.22	0.62	0.55
8	1.66	36.30	8.81	9.28	3.01	5.79	0.89	0.99
10	2.06	46.80	9.07	8.84	3.69	9.04	1.46	1.39
12	2.65	55.30	10.00	13.90	6.56	9.80	1.58	2.25
14	2.66	66.80	8.79	18.70	6.56	13.60	1.92	2.26

The specific cake resistance increased with the pressure drops, indicating cake compressibility. The greater resistance offered to flow at high pressures is caused by the more compact packing of the solids forming the cake. In compressible cakes, solid compaction increases as the filtrate flows

through cake because the filtrate exerts a drag force on the particles transmissible to the layer of solids from the surface of the filter cake to the medium surface (Richardson and Harker, 2002). In this study, the cake formed by XG 0.2% (m/m)_120 μm presented the highest and widest range of specific cake resistance values. It agrees with the literature since the highest superficial velocity and the lowest cake permeability were reported in that experimental condition. In contrast, the lowest values of specific cake resistance corresponded to the XG 0.2% (m/m)_50 μm as the thickest and lowest porosity cakes were formed in this condition.

The values of filter medium resistance were higher than the ones of specific cake resistance for all experimental conditions. They were also higher for XG 0.2% (m/m)_ 120 μm due to the highest superficial velocity of the filtrate in this condition.

Magioni (2015) reported a similar trend in specific cake permeability and compressibility. The author performed HTHP filter tests for aqueous and glycerin suspensions of $CaCO_3$ 5% (v/v) in a ceramic filter of 35 μm and the same pressure range as this study. Although Magioni (2015) studied a Newtonian fluid, an increase in the specific cake resistance was noticed as a function of pressure drop. Besides, a decrease in cake permeability and an increase in cake resistance were seen to increase with fluid viscosity. The order of magnitude of cake permeability was 10^{-14} and 10^{-16} m^2, and for the specific cake resistance, it was 10^8 and 10^{10} Kg/m for the aqueous and glycerin suspensions, respectively. Oliveira Junior (2014) used the same experimental apparatus as Magioni (2015) and reported thicker cakes for aqueous solutions of $CaCO_3$ 5% (v/v) than the ones from this study. It is justified by both the lower viscosity of water and the medium permeability to the materials used in this thesis. These factors favored fluid percolation while solids became retained in the membrane.

Figure 4.20 illustrates the cakes from XG 0.2% (m/m) right after the end of the experimental test at $8x10^5$ Pa. The cakes formed on the surface of the membrane of 50 μm (a and b) are thicker and more consistent. It is also visible the higher moisture content in the cake formed on the 120 μm filter (c and d).

Finally, the consistency and behavior indexes and the determination coefficient for the power-law fitting are listed in Tables 4.12 and 4.13 for $CaCO_3$ suspensions on XG 0.2 and 0.4% (m/m) through the membranes of 50 and 120 μm, respectively.

The consistency and behavior indexes decreased and increased to their respective reference suspensions for all filtrates, respectively. It was attributed to the lower solid content and polymer concentration in the filtrate due to the solid and polymer retention in the cake and membrane. Higher polymer concentrations increase the shear-thinning degree of solutions. The presence of solids impaired the alignment of the polymer molecules during shear, increasing the fluid resistance to flow. The filtrate rheograms for all filtrates are presented in Figure 4.21.

Table 4.12: Fitting parameters and determination coefficients for the power-law model for the filtrate of XG 0.2 and $CaCO_3$ through membranes of 50 and 120 µm.

	XG 0.2% (m/m)_50 µm			XG 0.2% (m/m)_120 µm		
ΔP (x10^5) [Pa]	m [Pa.s^n]	n [-]	r^2	m [Pa.s^n]	n [-]	r^2
Reference	0.961 ± 0.005	0.294 ± 0.002	0.999	0.961 ± 0.005	0.294 ± 0.002	0.999
2	0.0662 ± 0.008	0.306 ± 0.003	0.999	0.83 ± 0.01	0.288 ± 0.004	0.999
4	0.412 ± 0.002	0.367 ± 0.002	0.999	0.741 ± 0.003	0.294 ± 0.001	0.999
6	0.522 ± 0.005	0.327 ± 0.003	0.999	0.629 ± 0.009	0.311 ± 0.004	0.999
8	0.291 ± 0.005	0.396 ±0.005	0.999	0.73 ± 0.01	0.303 ± 0.004	0.999
10	0.237 ± 0.004	0.436 ± 0.005	0.999	0.630 ± 0.009	0.311 ± 0.004	0.999
12	0.281 ±0.002	0.384 ± 0.002	0.999	0.515 ± 0.009	0.323 ± 0.05	0.999
14	0.309 ± 0.003	0.381 ± 0.002	0.999	0.48 ± 0.01	0.335 ± 0.006	0.998

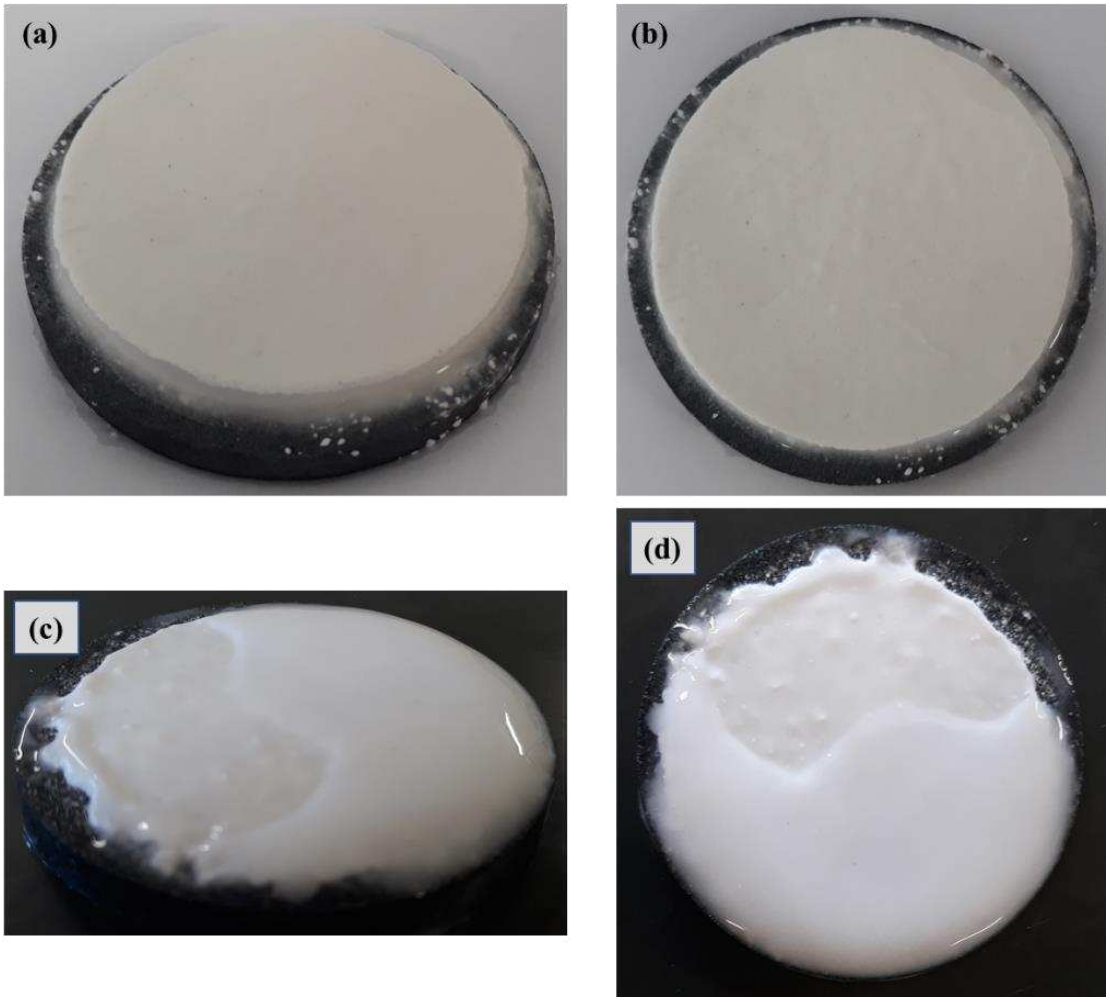

Figure 4.20: External cake from $CaCO_3$ suspension in XG 0.2% (m/m) on the surface of the membranes of 50 µm (a and b) and 120 µm (c and d).

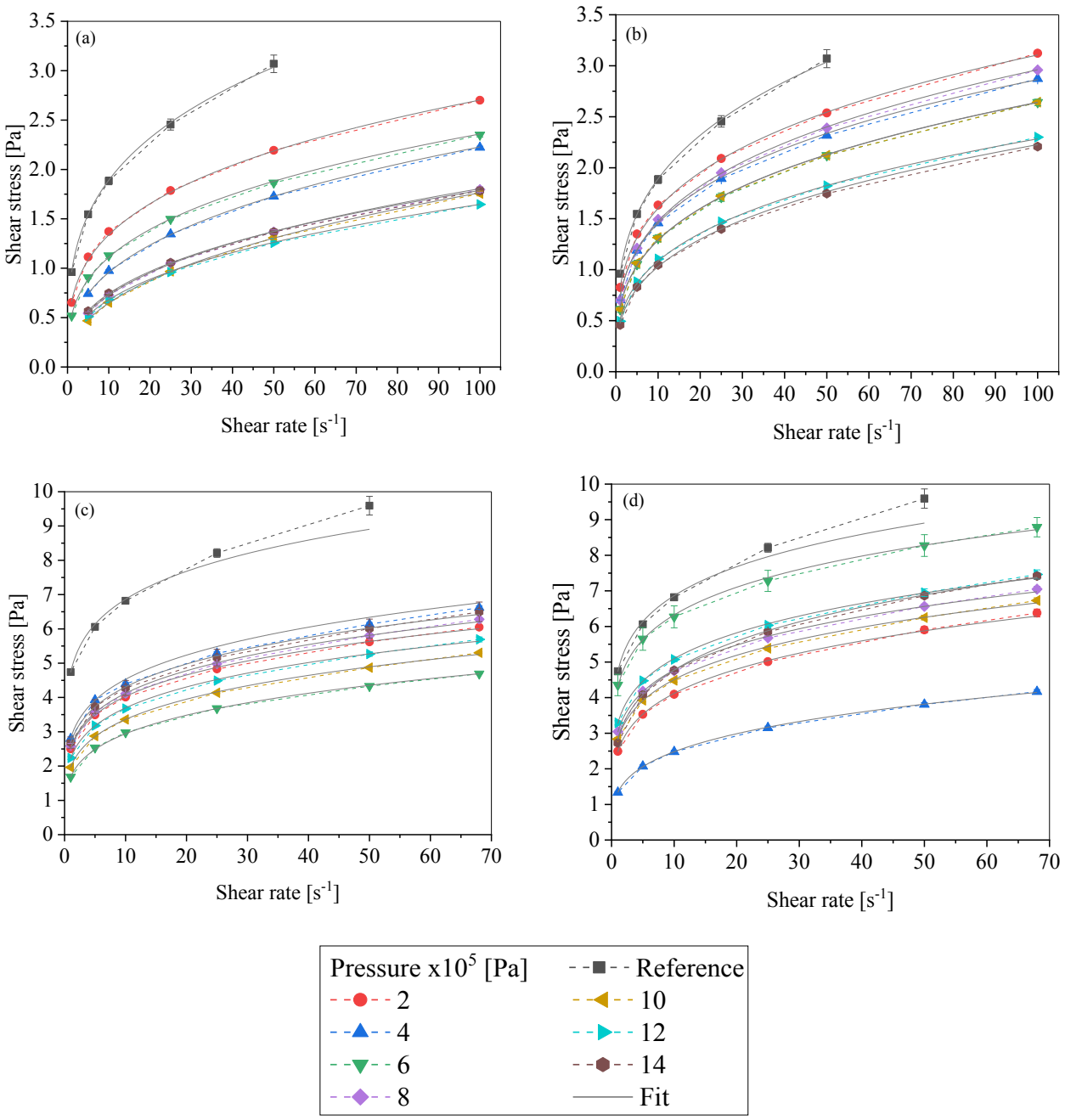

Figure 4.21: Rheogram of the filtrates for (a) XG 0.2% (m/m)_50 µm, (b) XG 0.2% (m/m)_120 µm; (c) XG 0. 4% (m/m)_50 µm, and (d) XG 0.4% (m/m)_120 µm.

Table 4.13: Fitting parameters and determination coefficients for the power-law model for the filtrate of XG 0.4 and $CaCO_3$ through membranes of 50 and 120 µm.

	XG 0.4% (m/m)_50 µm			XG 0.4% (m/m)_120 µm		
ΔP (x10^5) [Pa]	$\boldsymbol{m}$ [Pa.s^n]	$\boldsymbol{n}$ [-]	r^2	$\boldsymbol{m}$ [Pa.s^n]	$\boldsymbol{n}$ [-]	r^2
Reference	4.73 ± 0.03	0.162 ± 0.006	0.993	4.73 ± 0.03	0.162 ± 0.006	0.993
2	2.496 ± 0.008	0.208 ± 0.001	0.999	2.48 ± 0.02	0.221 ± 0.003	0.999
4	2.801 ± 0.007	0.209 ± 0.002	0.999	1.338 ± 0.007	0.268 ± 0.007	0.999
6	1.68 ± 0.02	0.243 ± 0.003	0.999	4.30 ± 0.06	0.168 ± 0.004	0.998
8	2.52 ± 0.03	0.214 ± 0.004	0.999	3.03 ± 0.02	0.197 ± 0.002	0.999
10	1.96 ± 0.01	0.234 ± 0.002	0.999	2.82 ± 0.02	0.204 ± 0.003	0.999
12	2.22 ± 0.02	0.221 ± 0.002	0.999	3.28 ± 0.02	0.192 ± 0003	0.999
14	2.66 ± 0.02	0.209 ± 0.003	0.999	2.83 ± 0.01	0.227 ± 0.002	0.999

4.2 Core flooding tests: Study 2

This subsection presents the core characterization and flooding tests. It is shown the findings of imaging analyses, saturation profiles, pore fluid occupancy, and cluster and globule size distributions for Studies 2A and then 2B.

4.2.1 Fluid and core characterization

The XG solutions used in Study 2 were assumed to have the same properties as shown in Table 4.3. The Soltrol mineral oil has a specific mass of 776 ± 3 Kg/m^3 and 2.5 ± 0.4 cP of viscosity. These are averaged values reported by Arshadi et al. (2018) and Tarantino and Mancuso (2005).

Regarding the characterization of the outcrop, its measured porosity and air permeability were reported to be 0.386 and 2.18x10^{-13} m^2, respectively. These petrophysical properties were similar to pre-salt Brazil carbonate reservoirs (Chinelatto et al., 2020; Valentín, 2018).

Being not exposed to oil, the outcrop was deemed to be water-wet. This was later confirmed by the pore-level images of fluid occupancies revealing oil and XG in the center and crevices of the pore space, respectively. The wetting phase tends to stick to the grain surfaces of water-wet samples.

Figure 4.22 shows the SEM images of the outcrop at different magnifications. It is possible to visualize the pore space roughness, different pore size, and grain.

The absolute permeability to water and the porosity of the cores are reported in Table 4.14. The differences in the petrophysical characteristics among the cores and among them and the outcrop were attributed to the outcrop heterogeneity and the core size. The miniature dimensions of the core make them below the representative elementary volume of the porosity and permeability, and hence the values could not be compared.

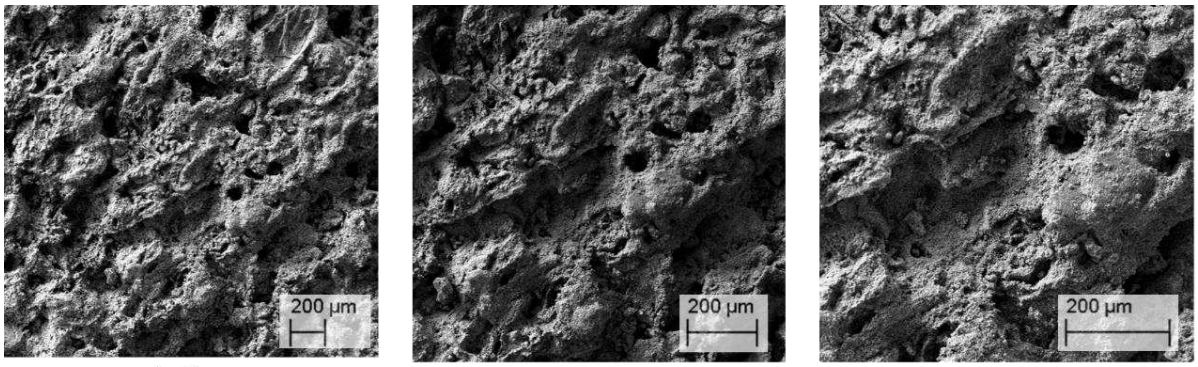

(a.1) (a.2) (a.3)

Figure 4.22: SEM images of the outcrop at (a) 50, (b) 100, and (c)150 magnifications.

Table 4.14: Absolute permeability and porosity values of cores.

	Core		
	1	2	3
Permeability [m^2]	$9.61x10^{-15}$	$1.07x10^{-15}$	$5.76x10^{-15}$
Total porosity [-]	0.3622	0.2673	0.2714
Porosity from resolvable pores [-]	0.1540	0.0640	0.1520
Porosity from micropores [-]	0.2082	0.2033	0.1194
Connected porosity [-]	0.3930	0	0.4250

The micropores play an important role in characterizing the total porosity of the cores better. The highest permeability of core 1 was attributed to the fracture placed from z = 14.57 mm to the bottom of this core. The fracture is a region of low aspect ratio, acting as a preferential fluid flow channel and thus increasing the core permeability. Besides, this core has the highest connected porosity and the largest pores and throats, as shown below. In contrast, core 2 had the lowest permeability and no connected porosity. These are attributed to the small coordination number and thin throats of this sample that were not resolved enough at 7.13 µm resolution.

Table 4.15 lists the pore network features like pore and throat radius, aspect ratio, and coordination number.

Table 4.15: Pore network features of cores 1, 2, and 3.

	Core		
Features	1	2	3
Number of pores [-]	730,377	514,394	628,088
Pore radius mean [µm]	19.39	16.38	19.52
Number of throats [-]	602,558	235,650	537,190
Throat radius mean [µm]	14.14	11.75	13.20
Coordination number (mean)	1.65	0.94	1.71
Aspect ratio (mean)	3.79	3.12	3.90

The coordination number is related to the interconnectivity of the pore space, and it is defined as the number of pore throats emanating from a pore body. Aspect ratio is the fraction between the radius of a pore-body and the radius of a connected pore-throat (Andersson, 2018; Civan, 2007; Zolfaghari and Piri, 2017).

A bi-modal profile described the pore size distributions, i.e., two main ranges of pore size characterize the cores, as is shown in Figure 4.23. Core 2 has the highest frequency of small and intermediate-sized pores, supporting the pore space features shown in the pore network analysis.

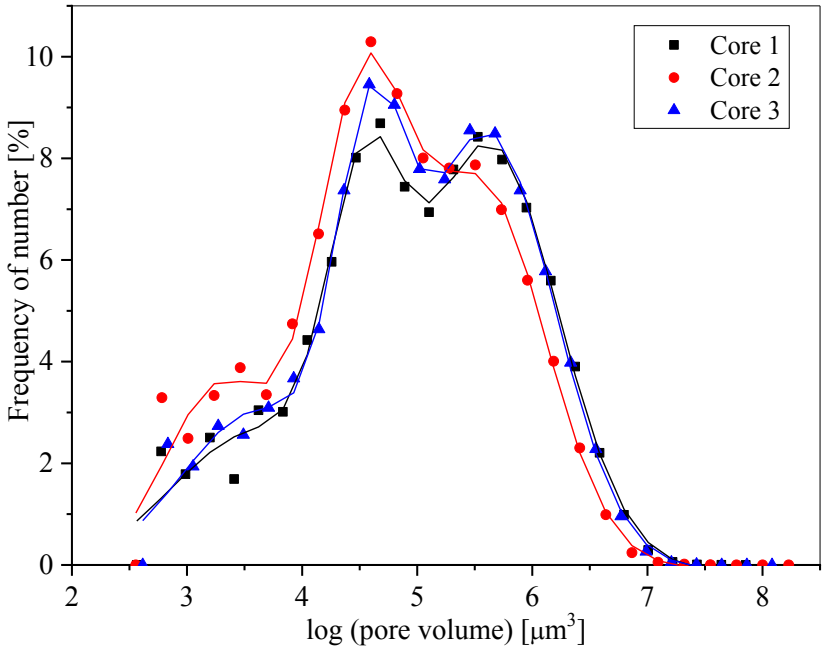

Figure 4.23: Pore size distributions of cores 1, 2, and 3.

4.2.2 Core flooding: Study 2A

This subsection discusses the results of saturation profile, pore fluid occupancy, and size distribution of XG and oil clusters and globules after drainage stages.

4.2.2.1 Saturation profiles

The porosity and the fluid saturation profiles along the height of cores 1 and 2 are represented in Figures 4.24 and 4.25, respectively. The total porosity profiles correspond to the resolvable pores segmented in the reference image state. Core 1 showed a higher and broader range of porosity variations. It is in line with the higher number and wider size distribution of pores in core 1 presented in Table 4.15 and Figure 4.23, respectively.

Larger pores and throats and higher values of connected porosity and permeability of core 1 also favored the polymer flow through this sample. The outlet flow rate of XG in the first experimental hour was 0.25 and 0.125 mL/min in cores 1 and 2, respectively.

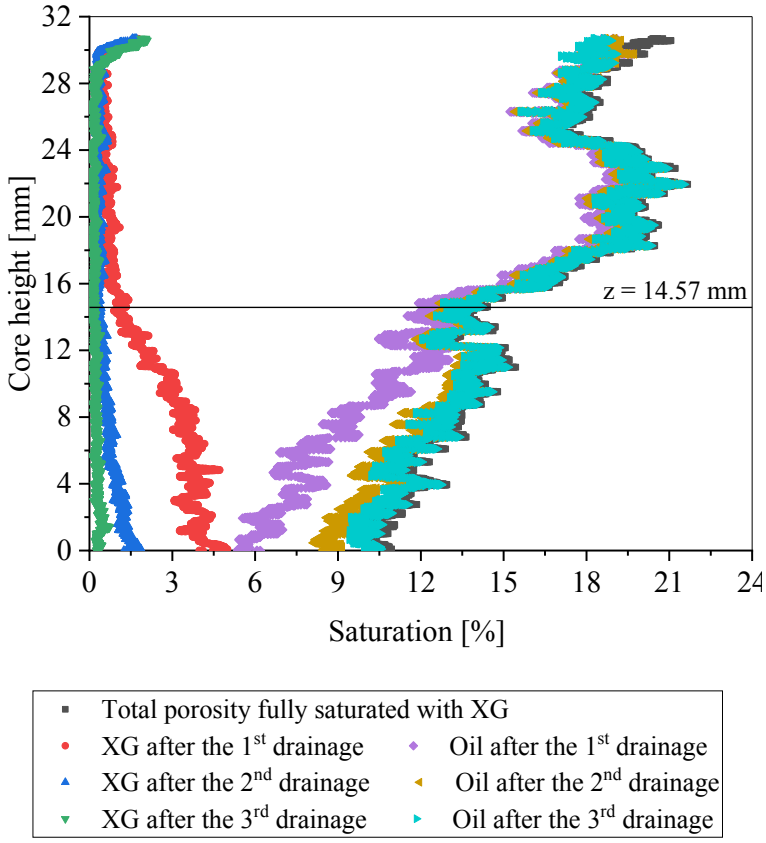

Figure 4.24: Porosity, XG, and oil saturation profiles at different stages of experiment 1.

The total porosity profiles also correspond to initial XG saturation profiles. It was assumed as several pore volumes of XG were injected into the cores, fully saturating the entire pore space.

Comparing XG saturation profiles at different drainage stages, the impact of polymer displacements from the pore space as the result of oil injections with different flow rates was noticed. The higher the oil flow rate, the higher the pressure drop to overcome the threshold capillary pressure and enhance the XG displacement. Table 4.16 lists the average percentage of the remaining initial polymer saturation after each oil injection in both cores.

Table 4.16: Average percentage of residual XG saturation after the drainage stages in cores 1 and 2.

Injection stage	Residual XG [%]	
	Core 1	Core 2
1st drainage	11.87	16.91
2nd drainage	3.60	8.54
3rd drainage	1.77	7.23

The higher residual XG saturation in core 2 is justified by its pore space features and high viscosity of XG 0.4% (m/m). The small pores connected by thin throats hinder the oil-to-polymer displacement in experiment 2. The network throats limit the wetting phase displacement for slow

flows when the capillary pressure reaches a maximum value (Blunt, 2017). In this core, the oil and XG rearrangements were marked by trapped phases spread along the core height, as it is discussed in the next sections.

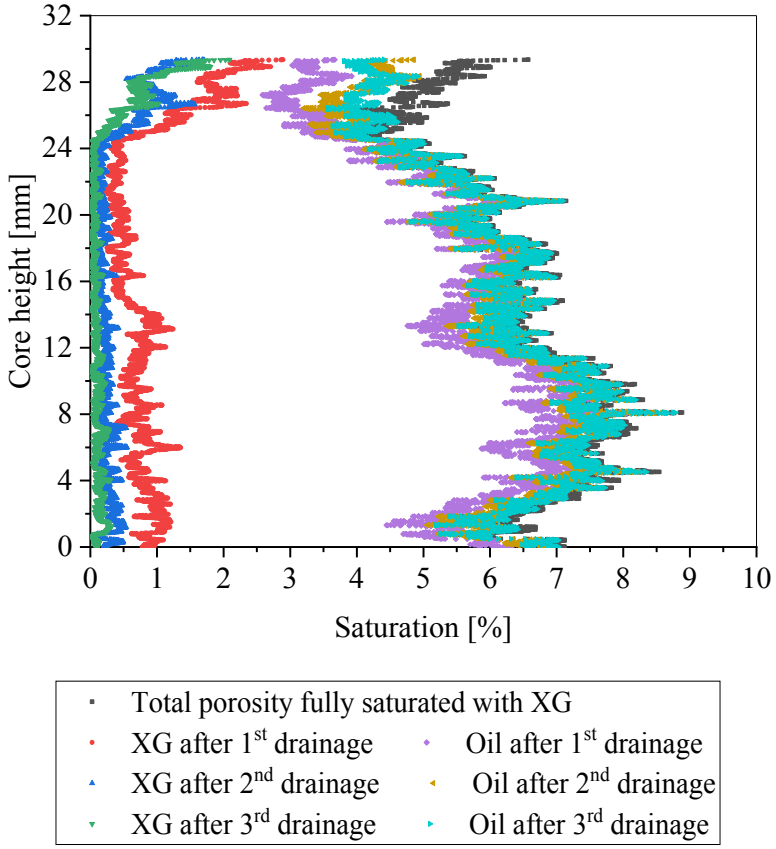

Figure 4.25: Porosity, XG and oil saturation profiles at different stages of experiment 2.

Figures 4.26 and 4.27 show the registered 2D-cross-sectional images of different stages of oil injection in core 1 and 2, respectively. The different phases were noted by their apparent densities. White, black, and gray represent grain, XG, and oil and/or micropores, respectively.

The widest polymer saturation was seen after the primary drainage in core 1. A higher polymer saturation was reported in the lower half of the sample where the fracture is placed. In the fracture, the frictional resistance is minimal for the polymer solution to be produced at the outlet. As a result, most of the oil-to-polymer displacements happened in the fracture, and the residual polymer was mainly retained in the pore space of the matrix surrounding the fracture. That increased XG saturations at the bottom of core 1. As the oil flow rate was increased in the subsequent oil drainages, the matrix pore space tended to get invaded more by the oil. This is because the frictional resistance along the fracture length increases at higher oil flow rates, which subsequently allows oil-to-polymer displacements to occur in the surrounding matrix.

Although the XG saturation decreased in both cores, a residual saturation was still noticed, mainly placed near the core inlet. It was attributed to polymer retention. At the inlet, the oil first

displaces polymer from a part of the core entrance before it starts to displace the cross-section more uniformly. This phenomenon could lead to permanent formation damage due to pore blockage. The top of the core is also the first mechanical barrier to polymer flow, where most of the polymer molecular chains tended to stick. It resulted in partial or even complete blockage of pores. Agi et al., 2018 in a reviewed study, also reported a high polymer saturation at the core close to the inlet and a decreasing saturation along the core height. The high concentration of XG in core 2 also corroborates with the polymer retention in this sample. The increase in polymer concentration elevates the number of polymer molecules per unit of volume, raising the probability of molecular retention on rock surfaces (Sazali, Roslan, and Jarrahian, 2019; Dang et al., 2014; Zhang and Seright, 2013).

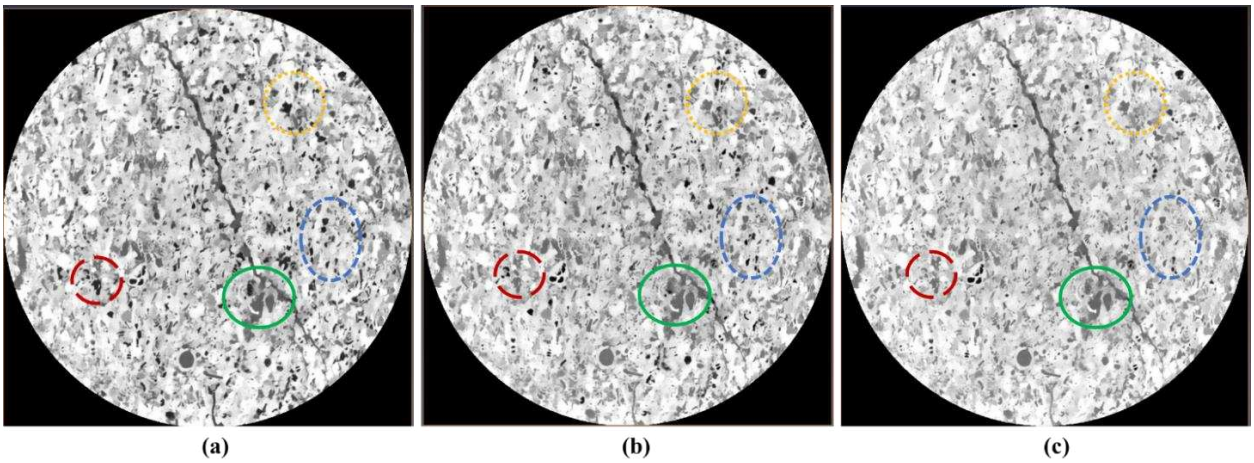

Figure 4.26: 2D cross-sections of registered images after the first (a), second (b), and third (c) oil injection in core 1.

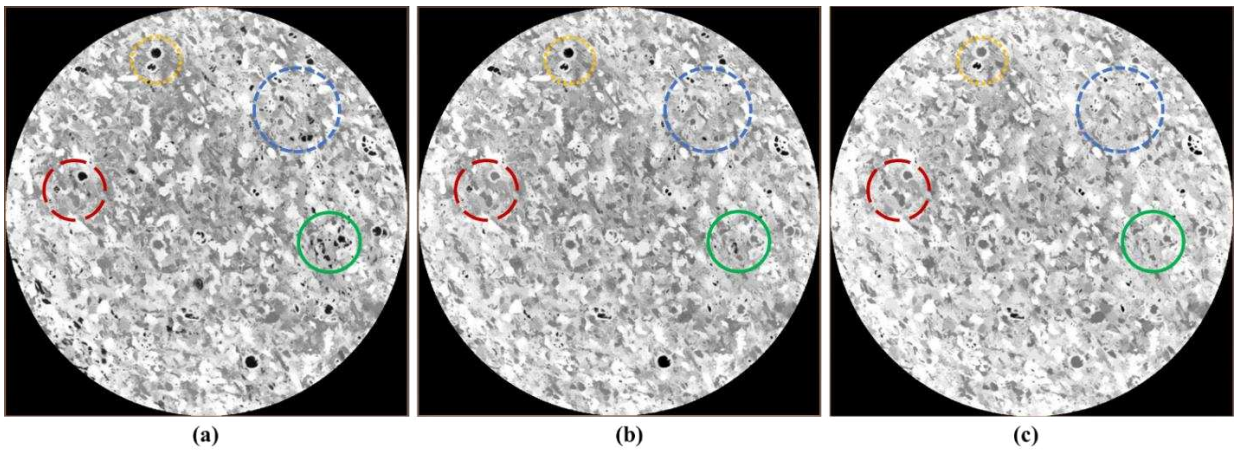

Figure 4.27: 2D cross-sections of registered images after the first (a), second (b), and third (c) oil injection in core 2.

To put numbers in perspective, the residual XG saturation after the third oil injection was compared in two different regions of each pore space. These regions have similar porosity and are located near and far from the inlet of the cores. It was found 2 and 0.14% of residual XG at 30.7

mm and 21.4 mm, respectively, in sample 1. In sample 2, the residual polymer was 5.46 and 0.05% at 31.23 and 8 mm, in this order.

The polymer retention at the inlet of cores 1 and 2 is illustrated in Figures 4.28 and 4.29, respectively. They are a set of 2D cross-sections of 3D registered images corresponding to the first slice of each sample. The reference state is represented from (a) to (c). The target state corresponds to the third drainage, and it is shown from (d) to (f). In the grayscale of the pore space (a and d), black intensity corresponds to pore, gray to micropore, and white to the grain. After XG and oil injections, black corresponds to XG and light gray to oil, while micropore and grain remain gray and white, respectively. In the extracted pore space (b and e), yellow represents XG and red tags oil. Lastly, in the total segmentation of porous media, light blue is the micropore, dark gray is grain, and yellow and red are still XG and oil, respectively.

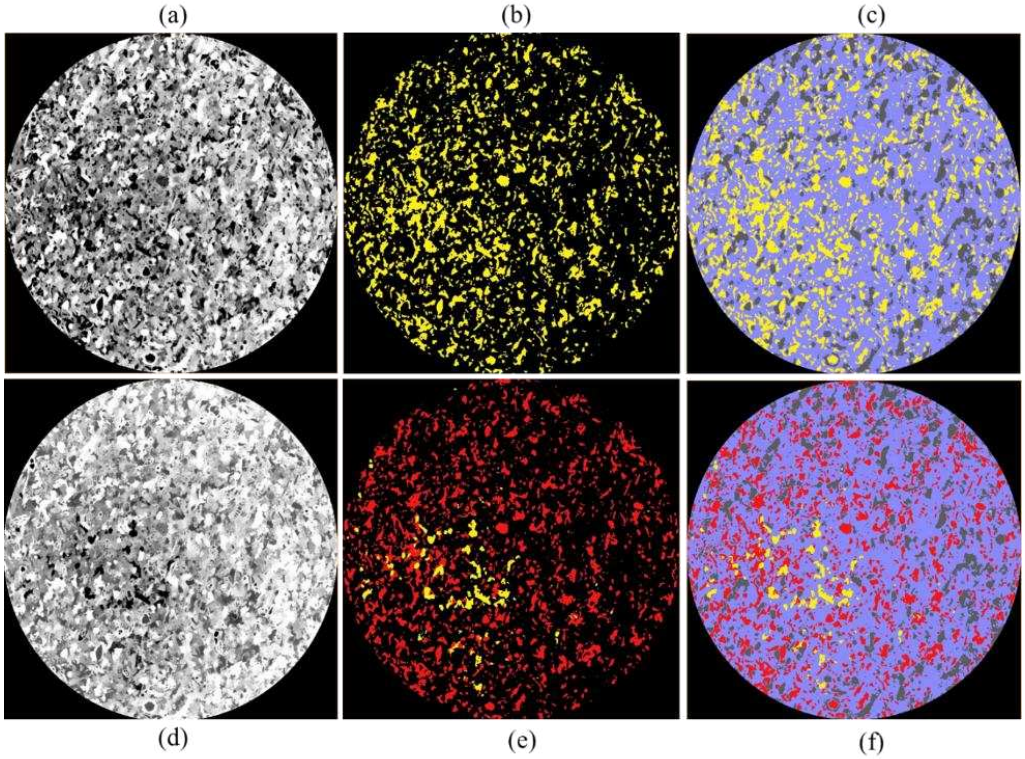

Figure 4.28: 2D cross-sections of 3D registered images of core 1 for the reference (a – c) and target (d – f) states. (a) and (d) is the grayscale image, (b) and (e) the resolved pore space where oil is in red and XG in yellow, and (c) and (f) is the final four label segmentation with the microporosity (light blue) and grain (in gray) regions.

The oil saturation profiles after different drainage stages showed both a similar trend to the core porosity profiles and the influence of the injected flow rate. As the oil flow rate increases, oil could invade narrow regions of the pore space, increasing the efficiency of oil-to-polymer displacements and thus the oil saturation and occupancy.

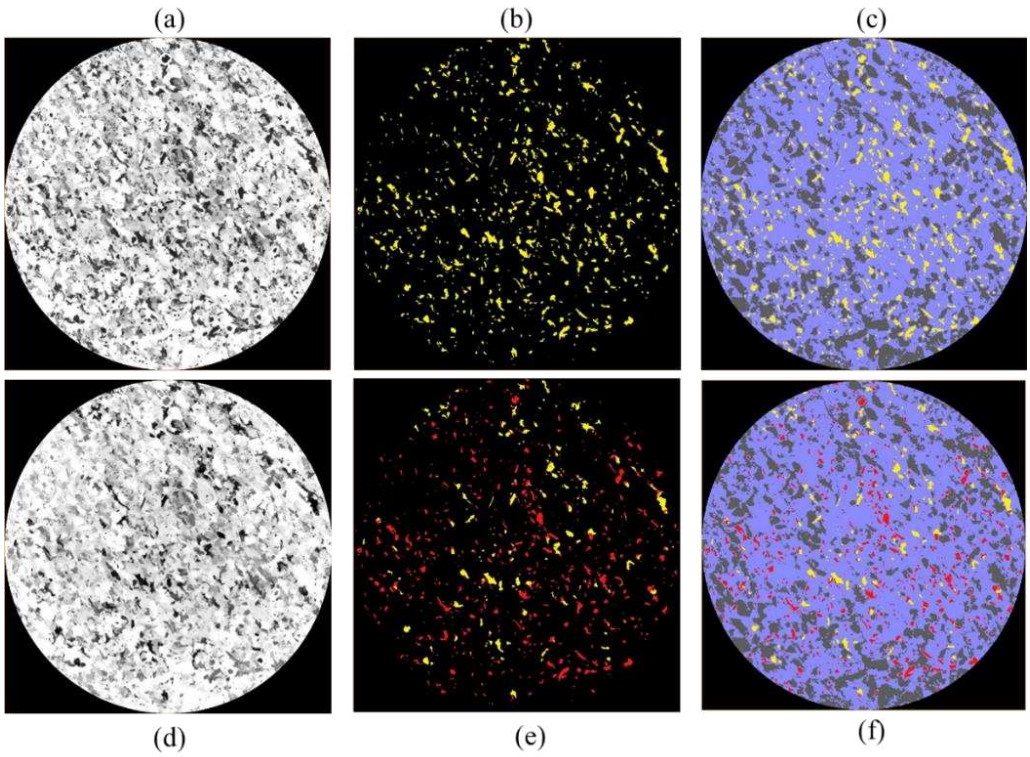

Figure 4.29: 2D cross-sections of 3D registered images of core 2 for the reference (a – c) and target (d – f) states. (a) and (d) is the grayscale image, (b) and (e) the resolved pore space where oil is in red and XG in yellow, and (c) and (f) is the final four label segmentation with the microporosity (light blue) and grain (in gray) regions.

4.2.2.2 Pore fluid occupancy, cluster, and globule size distributions

In this thesis, the term "cluster" refers to the XG and oil phases. "Globule" distinguishes different bodies separated based on their connectivity (in 3D). Figure 4.30 shows a sequence of 2D cross-sections of the oil phase in the pore space of core 1 after the second drainage, illustrating the concepts above.

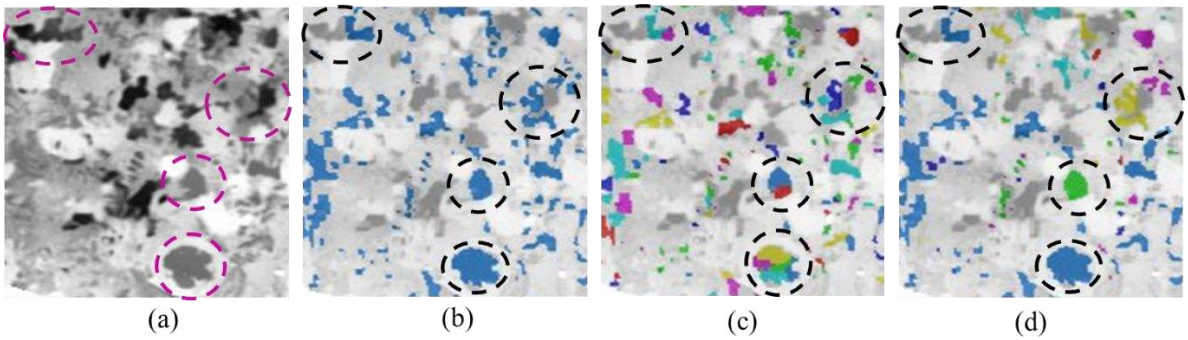

Figure 4.30: 2D cross-section of registered images in core 1 after the second drainage showing the (a) grayscale image, (b) oil phase, (c) oil clusters, and (d) oil globules.

(a) Pore fluid occupancy

This subsection analyzes the size distribution of pores occupied by XG and/or oil. The segmented pores were separated based on their concavity and convexity in 3D and then marked with XG or oil (one fluid at a time). Then, they were labeled and classified in ranges of size. The assignment of a pore that held a certain phase does not rely on the amount of phase. If both phases fill the same pore, this pore is accounted for in the histograms of pores occupied by XG and oil.

The pore size distributions of pores occupied by XG are illustrated in Figures 4.31 and 4.32 for experiments 1 and 2, respectively. As the distinction between XG and water in the images could not be made, the pore size distribution curve after XG injection represents the entire resolvable pore space. As the oil injections were carried out, the residual polymer was mostly placed into small and intermediate-sized pores. This can be seen from the shift to the left of size distributions of pores occupied by XG. The capillary pressure in the larger pores is smaller than in narrow ones, so the oil tends to fill the bigger pores first and then migrate toward narrow pore space portions. It is extensively accepted that due to the irregular pore shapes, the oil moves to the center of the pore while the wetting phase remains in small pores, thin throats, roughness, and crevices in a new equilibrium arrangement (Blunt, 2017).

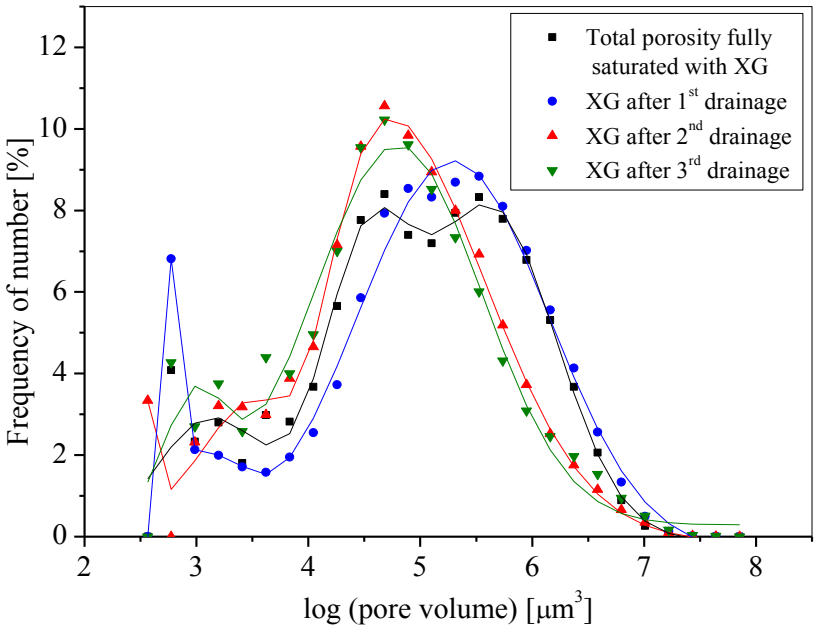

Figure 4.31: Pores occupied by XG 0.2% (m/m) at different stages of experiment 1.

In experiment 1, the highest frequency of the small pores with residual XG occurred after the first drainage. An average of 6.8% of the filled pores corresponded to the smallest pore size range (3.66 and 5.96×10^2 µm^3). In contrast, in experiment 2, the smallest pores constituted the highest percentage of pore occupied by the residual XG after all drainages. The third stage in core 2

resulted in the sharpest frequency of the smallest pores with the polymer. A mark of 18.9% of filled pores was ranged between $6.05x10^2$ and $1.02x10^3$ μm^3.

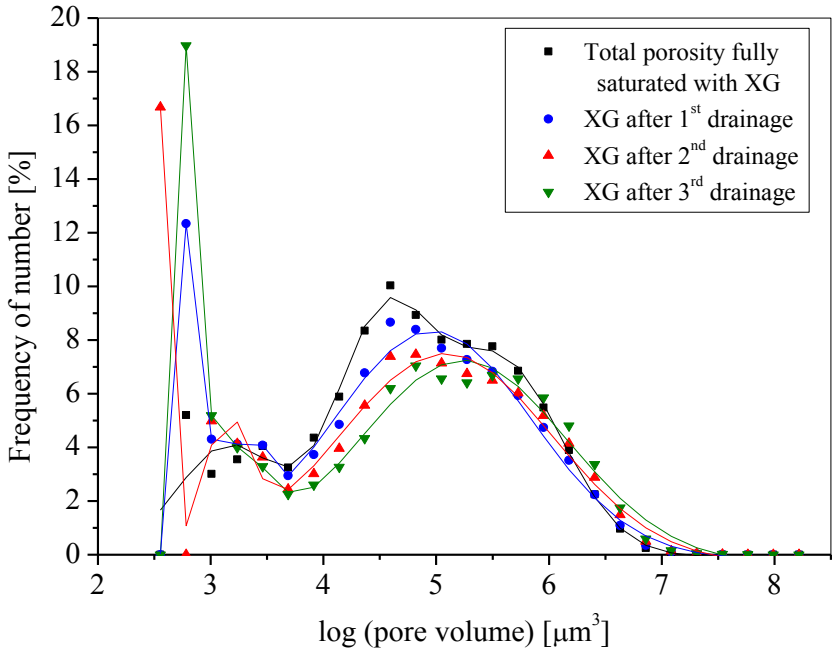

Figure 4.32: Pores occupied by XG 0.4% (m/m) at different stages of experiment 2.

The influence of the fracture in the lower half of core 1 and its impact on the fluid arrangement after oil injections is shown in Figure 4.33. It represents the last slice of this sample after each drainage stage. First, oil displaced XG from the fracture (large feature) and then from the small pores in the surrounding matrix.

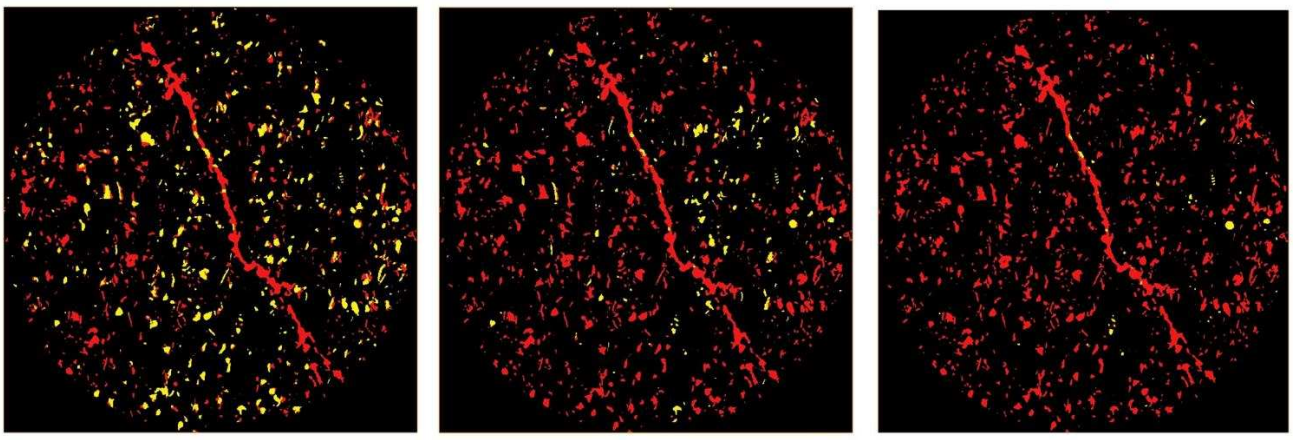

Figure 4.33: 2D cross sections of the last slice in core 1 after the (a) first, (b) second, and (c) third oil injection stages. XG and oil are tagged as yellow and red, respectively.

Table 4.17 lists the number of pores with polymer after each stage of oil injection in experiments 1 and 2. The number of pores holding XG decreased as the oil flow rate increased.

The non-wetting phase settled in the pores previously saturated with the polymer. After the second and third drainages, there were more pores containing XG in experiment 2 than 1. It was attributed to the trapped XG in thin pore-throats of core 2 that hinder the oil-to-polymer displacement.

Table 4.17: Number of pores occupied by XG at different stages of experiments 1 and 2.

	Core 1	Core 2
All pores	753,415	523,405
1st drainage	205,683	156,684
2nd drainage	82,233	99,781
3rd drainage	45,371	82,476

The histograms of oil-filled pores for both cores resemble their respective pore size distribution, but the dynamics of pore occupancy differ between them. Figures 4.34 and 4.35 show the size distributions of pores holding oil in experiments 1 and 2, respectively.

Most pores were filled with the non-wetting phase right after the first oil injection in experiment 1. It is because the number of pores with oil remained almost constant in all drainage stages (716,089 and 718,270 after the first and third oil injections, respectively). So, rather than the number of pores occupied by oil, the saturation of the pores was flow rate dependent.

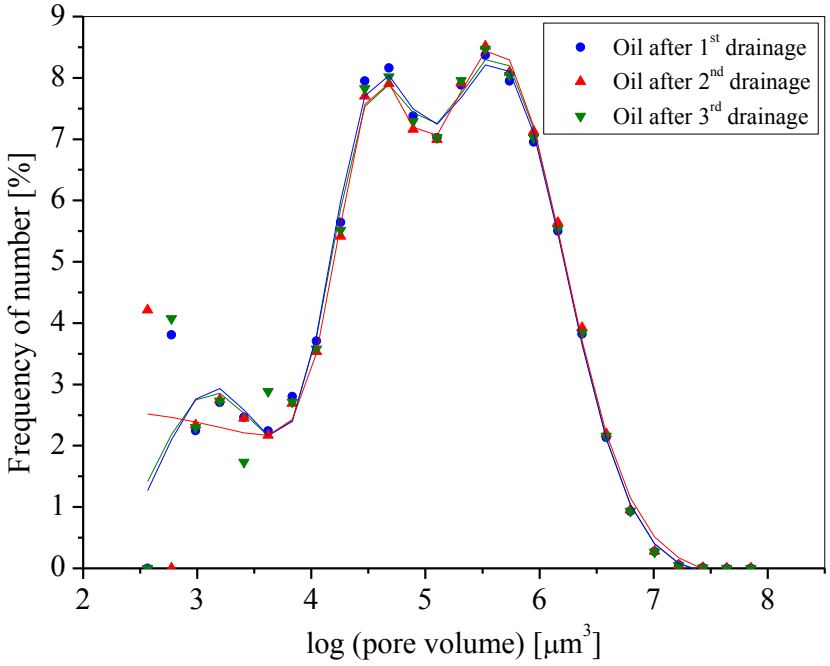

Figure 4.34: Pores occupied by oil at different stages of experiment 1.

In experiment 2, the saturation and the number of pores holding the oil phase were a function of the oil flow rate. In this case, the number of filled pores corresponding to a size range increased as the total number of filled pores increased. After the first and third oil injections, 427,075 and 505,378 pores were filled with oil, respectively.

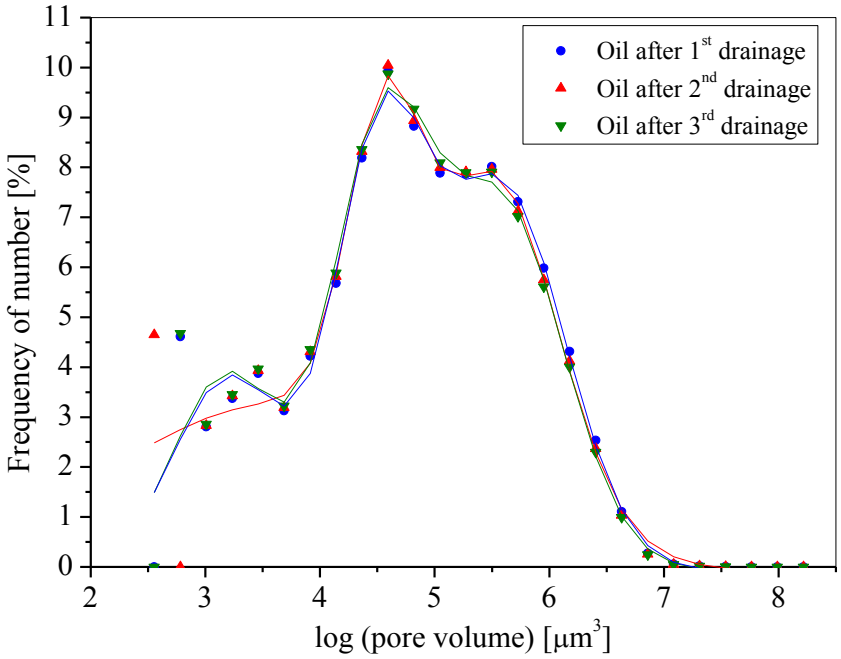

Figure 4.35: Pores occupied by oil at different stages of experiment 2.

(b) Cluster size distribution

For the analysis of cluster size distribution, the XG and oil phases were selected and separated based on their concavity and convexity geometry. They were then labeled and arranged in volume intervals.

The number of XG clusters after each experimental stage for both cores is listed in Table 4.18. The size distributions are represented in Figures 4.36 and 4.37 for experiments 1 and 2, respectively.

Table 4.18: Number of XG clusters at different stages of experiments 1 and 2.

	Core 1	Core 2
All pores	753,415	523,405
1st drainage	230,999	163,064
2nd drainage	80,798	108,420
3rd drainage	43,840	92,035

The number and size of the residual XG clusters decreased as a result of oil injection. The higher number of clusters to the number of pores occupied by them was verified for all drainage stages in sample 2 and for the first drainage in sample 1, meaning that some pores hold more than one cluster. Khishvand, Akbarabadi, and Piri (2016) reported a decrease in cluster sizes as a flow rate function. According to the authors, as the capillary number increases, the cluster size of the displaced phase decreases.

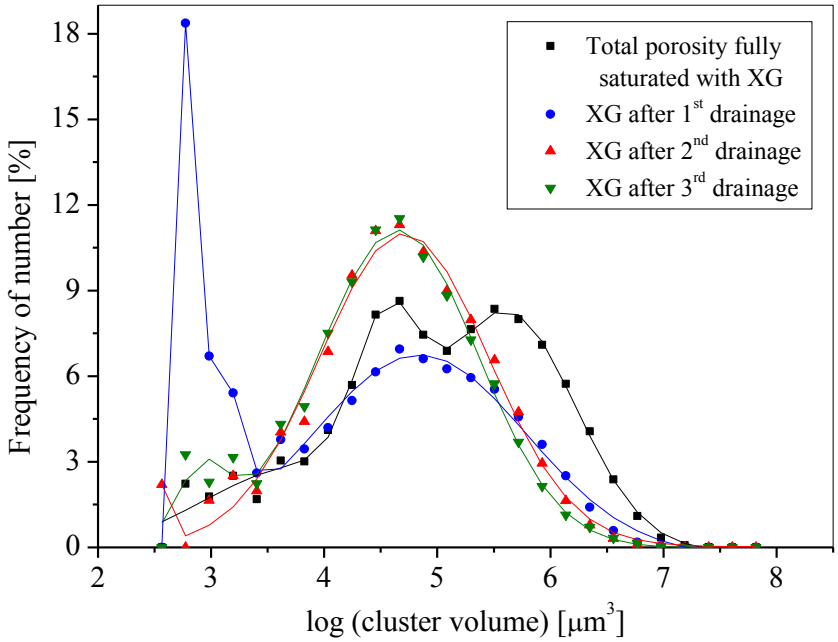

Figure 4.36: Size distribution of XG 0.2% (m/m) clusters at different stages of experiment 1.

The average size of residual XG clusters increased in core 1 after the second and third drainages. It was attributed to polymer coalescence. The high oil flow rates intensify the polymer displacement toward narrow features. Once in these regions, the displaced XG can re-connect with the neighboring cluster, resulting in larger clusters. After the first XG oil injection, 18.4% of clusters were ranged from 5.95 to 9.65×10^2 µm^3. The coalesced residual clusters, in turn, had an average size of 4.64 and 7.53×10^4 µm^3. Clusters of the displaced phase can coalesce with others, mainly when the displacing fluid flows at high flow rates mobilizing the displaced phase toward the outlet (Khishvand, Akbarabadi, and Piri, 2016).

In experiment 2, on the other hand, the decrease in the number of residual XG clusters was attributed to the reduction in polymer saturation. The low permeability of core 2, reduces the mobility of polymer clusters and, consequently, the growth of large clusters. The highest frequency of cluster size corresponded to the small ones. An average of 38.4% of the XG clusters was ranged from 6.06×10^2 to 1.02×10^3 µm^3 after the last oil injection.

Figures 4.38 and 4.39 illustrate a set of the 3D spatial distribution of XG at different stages of experiments 1 and 2, in this order. The images correspond to a sub-volume of 9.7 mm^3 extracted at 17.8 mm from the inlet of both cores. In the first sequence of images, yellow represents the XG. In the second sequence, the group of colors tags the polymer clusters.

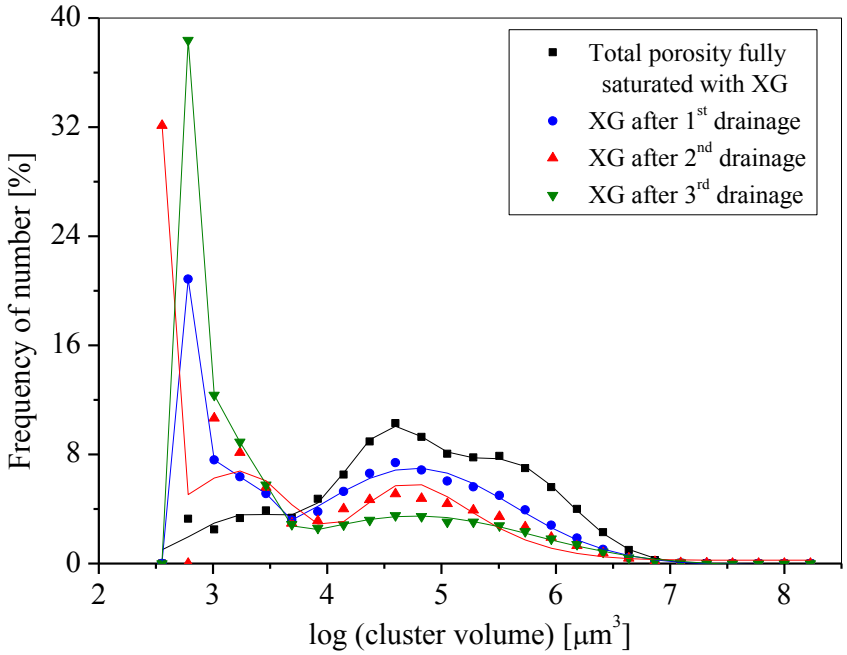

Figure 4.37: Size distribution of XG 0.4% (m/m) clusters at different stages of experiment 2.

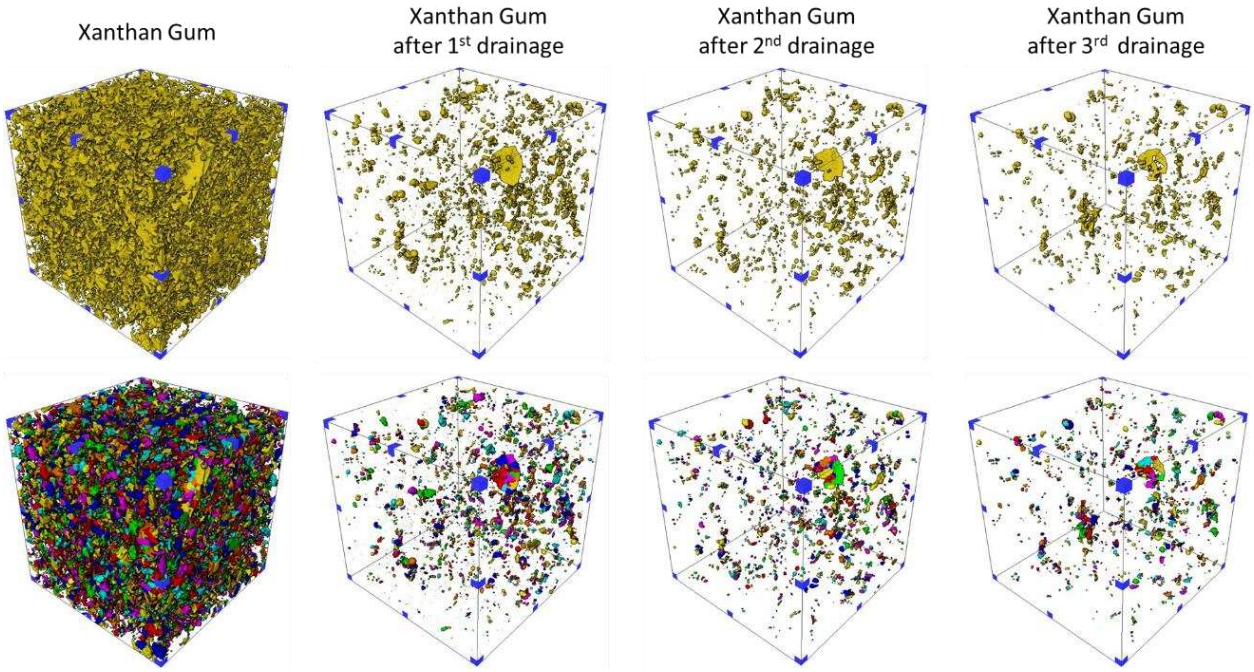

Figure 4.38: 3D spatial distribution of XG 0.2% (m/m) at different stages of experiment 1. XG phase (yellow) and XG clusters (a group of colors) are illustrated in the first and second rows, respectively.

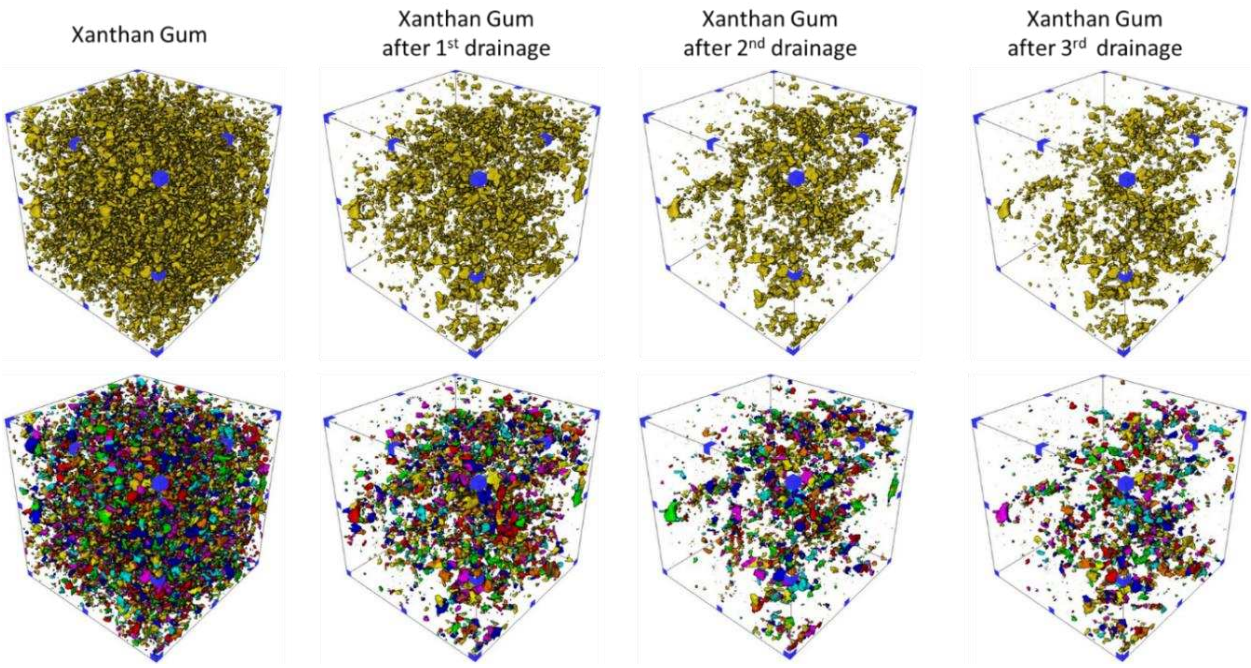

Figure 4.39: 3D spatial distribution of XG 0.4% (m/m) at different stages of experiment 2. XG phase (yellow) and XG clusters (a group of colors) are illustrated in the first and second rows, respectively.

A similar analysis was done for the oil phase. Core 1 had the highest residual XG saturation after the first oil injection. Once the oil injection was stopped, the stress was removed from the polymer in the pore space. It caused polymer rearrangement, disconnecting the oil phase and increasing the number of oil clusters. As the second and third oil injections occurred, less polymer rearrangement happened. Besides, the invading and the remaining oil could be re-connected, forming larger oil clusters. It was noticed by the decrease in the number of oil clusters from the first (821,190) to the last oil injection (720,576) at the same time that their size increased (Figure 4.40).

In experiment 2, the number of oil clusters increased as a function of oil saturation. The higher number of oil clusters to the pores filled with oil lets one assume that some pores were occupied by more than one cluster: 436,815 clusters and 427,075 pores after the first oil injection, and 524,625 and 505,378 clusters and pores after the last oil injection, respectively. The wetting and non-wetting phases might share the pore space in this sample. Finally, the histogram of the size distribution (Figure 4.41) shows a constant ratio between the increase in the number of oil clusters in a size range and the total number of oil clusters.

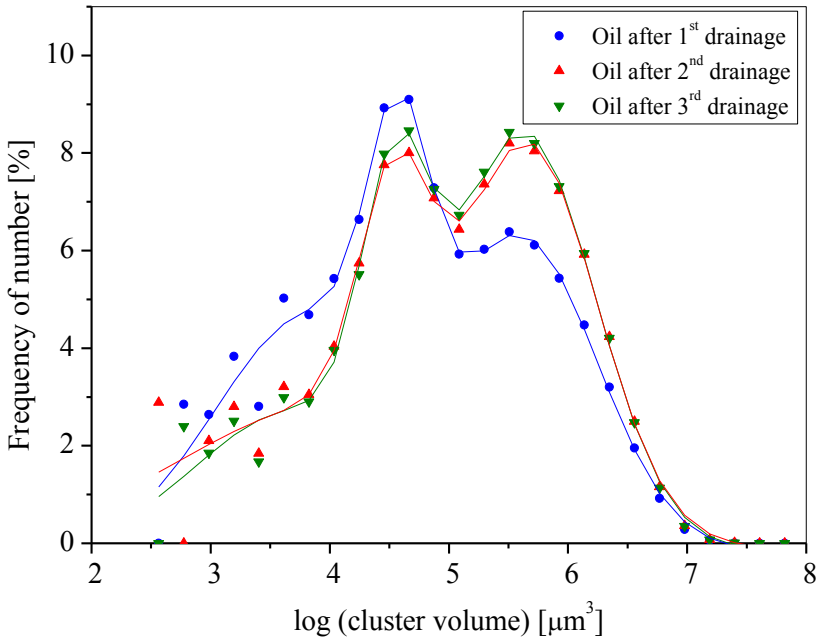

Figure 4.40: Size distribution of oil clusters at different stages of experiment 1.

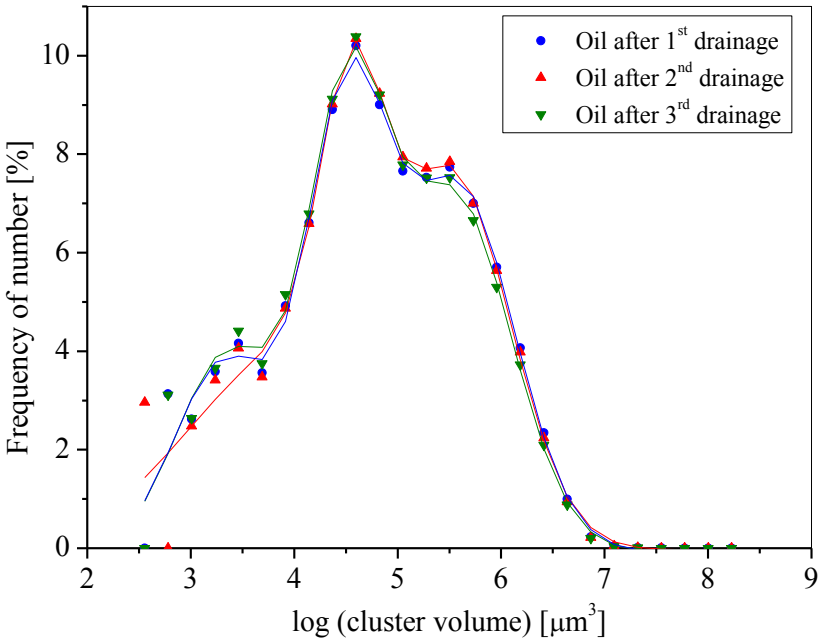

Figure 4.41: Size distribution of oil clusters at different stages of experiment 2.

(c) Globule size distribution

The globule concept refers to different disconnected objects of XG and oil phases. For this, the extracted XG and oil phases were separated based on their connectivity, labeled, and then classified in a range of bin sizes.

As the oil flow rate increased, the total number of XG globules decreased from the first to the last oil injection. In core 1 it decreased from 196,748 to 38,358, and in core 2 from 141,319 to 84,253. In experiment 1, the highest frequency (31.3%) and number (61,519) of XG globules occur after the first oil injection. It was supposed that most of these globules correspond to the small ones (ranged between $8.23x10^2$ and $1.85x10^3$ μm^3) placed in the porous matrix near the fracture. After the second and third drainages, because of polymer coalescence, larger globules were the most noticeable (an average of 18.6% of the number of globules ranged from $4.73x10^4$ to $1.06x10^5$ μm^3. Figure 4.42 shows the size distribution of XG globules at different stages of experiment 1.

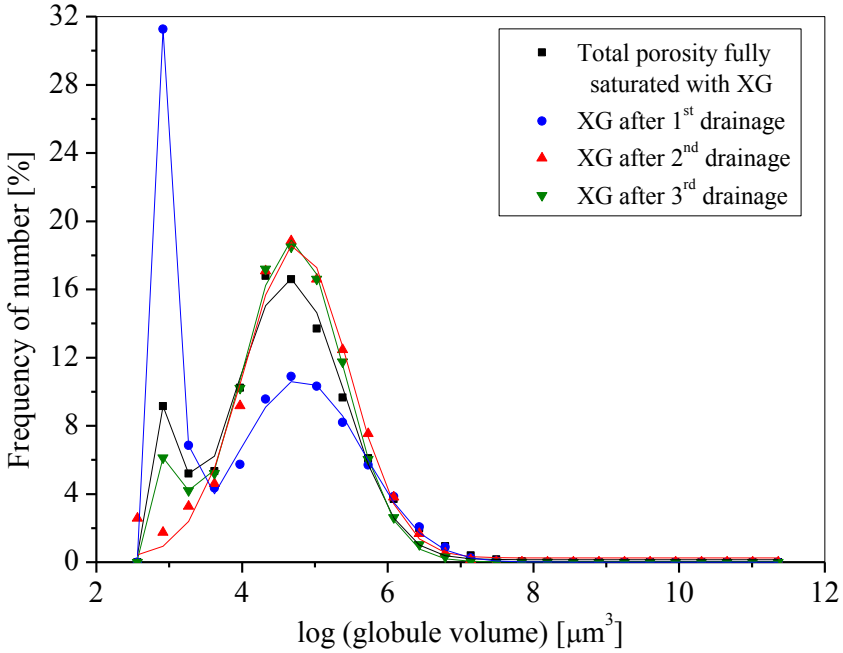

Figure 4.42: Size distribution of XG 0.2% (m/m) globules at different stages of experiment 1.

In experiment 2, the decrease in the number of XG globules was attributed to the reduction in the polymer saturation rather than coalescence. It is graphically reported by the sharp rise in the frequency of small globules after each oil injection, as Figure 4.43 presents. The smallest residual XG globules ranged between $6.99x10^2$ and $1.36x10^3$ μm^3, corresponding to 26.2 and 44.4% of total residual globules after the first and last drainage, respectively. A multiphase globule occupancy was also noticed in the last oil injection since the number of XG globules (84,253) was higher than the number of XG-filled pores (82,476).

Figures 4.44 and 4.45 represent the 3D spatial distributions of connected pore space and XG globules at different stages of oil injection in cores 1 and 2, respectively. A color represents each globule. The larger connected pore space in core 1 is seen from the upper half of the sample to the fracture, and it is depicted in blue color. On the other hand, no connected pore space was reported in core 2. It was attributed to the resolution of the images that might not be enough to resolve the thin pore-throats smaller than 7.13 µm. Besides, the retained polymer was noticed near the inlet face of both cores. Finally, the residual XG globules are mostly placed in the lower half of core 1.

They correspond to the globules in the matrix pores near the fracture, where the first oil-to-polymer displacement occurs.

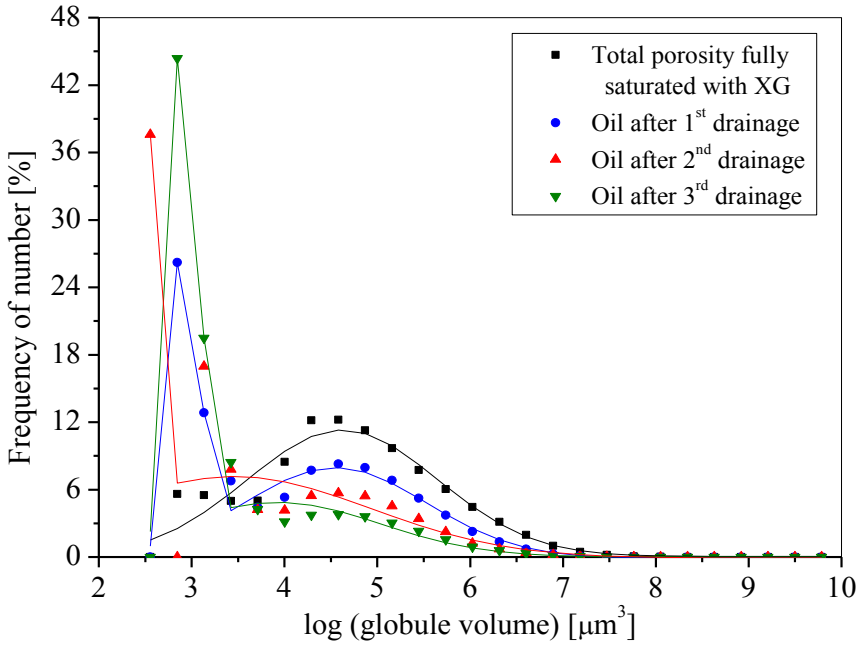

Figure 4.43: Size distribution of XG 0.4% (m/m) globules at different stages of experiment 2.

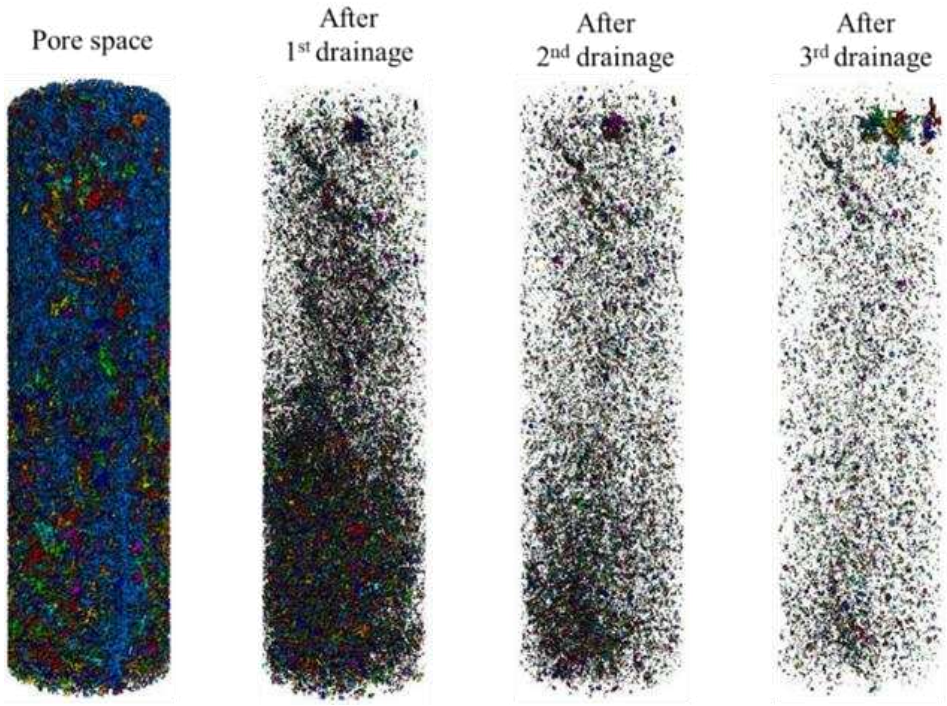

Figure 4.44: 3D spatial distributions of XG 0.2% (m/m) globules at different stages of experiment 1. Each color represents a globule.

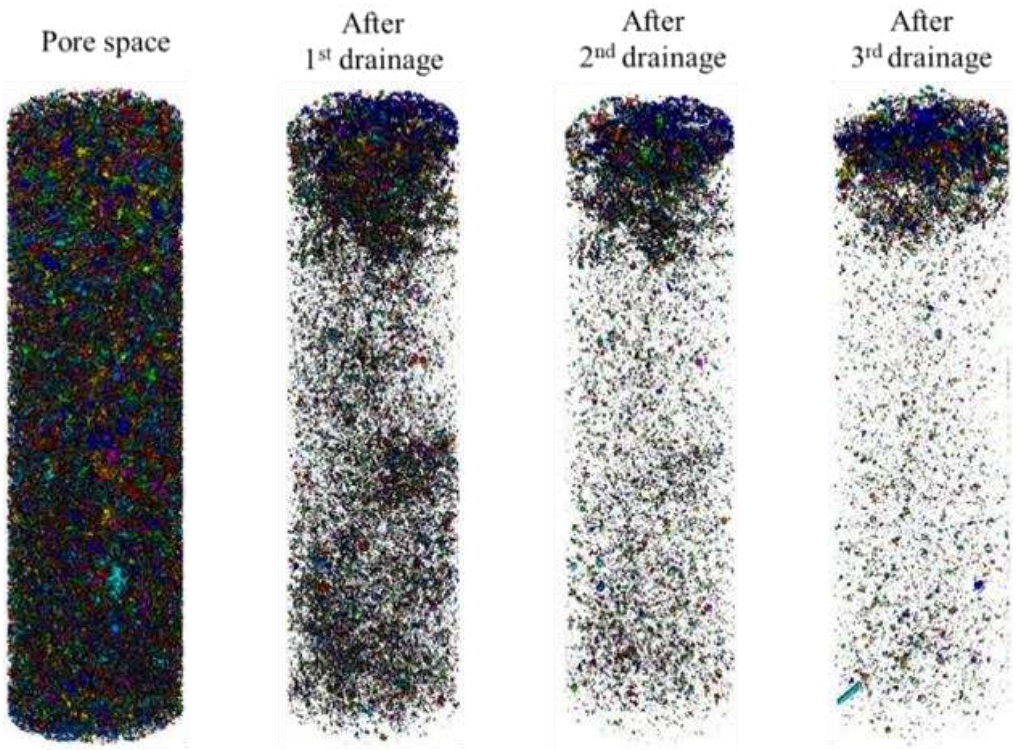

Figure 4.45: 3D spatial distributions of XG 0.4% (m/m) globules at different stages of experiment 2. Each color represents a globule.

The analysis of oil globules showed the difference in the fluid arrangement in the pore space of both cores. In core 1 the number of oil globules decreased from 376,471 in the first oil injection to 284,563 in the last one. In core 2, on the other hand, these numbers increased from the first (261,019) to the last (326,785) drainage stage.

It is worth mentioning that the disconnected oil clusters caused by the polymer rearrangement in the pore space once the stress of oil injection was removed are now reported as isolated oil globules. As the oil displaced most of the XG placed in the features with a lower threshold capillary, the oil saturation increased. It enabled the re-connection among the injected and the remaining oil, forming larger globules. It was noticed by the decrease in the number of globules and the increase in the frequency of larger globules in the histogram curves (Figure 4.46).

A different approach was verified in experiment 2. The number of oil globules raised after each drainage stage, and their size distribution remained almost constant. The residual XG trapped in the pore space hindered the connectivity of oil. Besides the low connected pore space, the higher consistency index of XG 0.4% (m/m) increased the viscous resistance of fluid flow. This results in the highest number and frequency of intermediate-sized oil globules (average of 2.88×10^5 μm^3) coexisting with the XG along the core height, as Figure 4.47 shows.

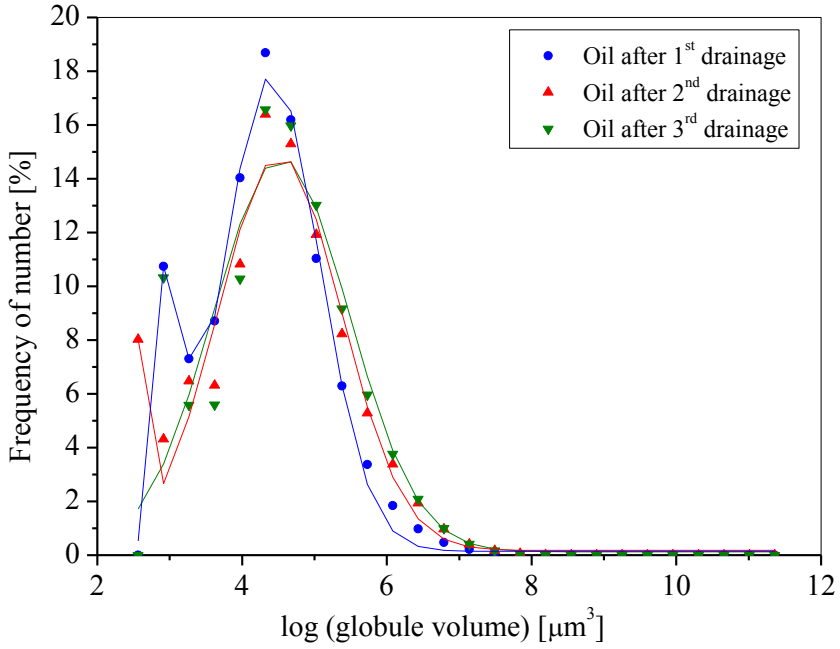

Figure 4.46: Size distribution of oil globules at different stages of experiment 1.

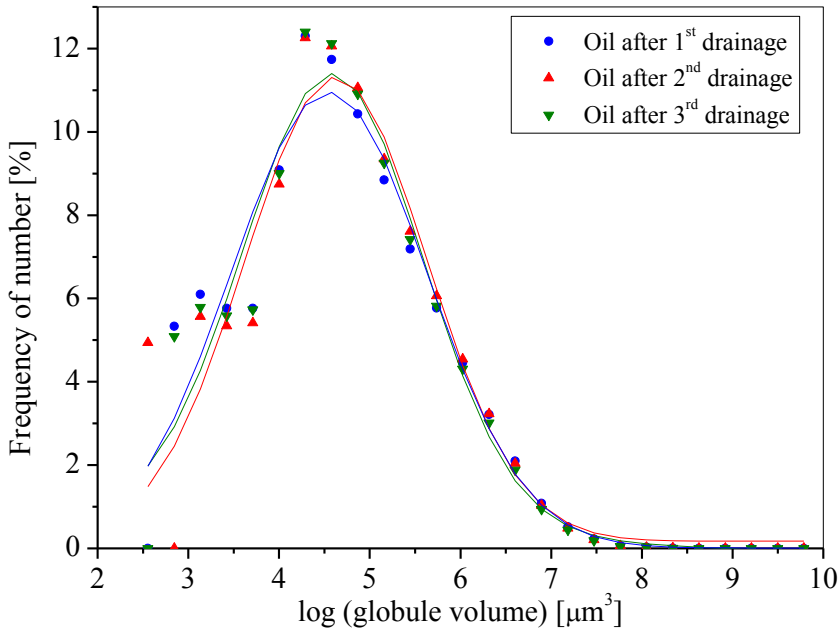

Figure 4.47: Size distribution of oil globules at different stages of experiment 2.

The 3D view of the spatial distribution of oil globules is represented in Figures 4.48 and 4.49 for core 1 and 2, respectively. Each globule is represented by a color. In core 1, a large oil globule (in blue) is seen from the upper half to the fracture, and small globules are mainly placed in the porous matrix near the fracture in the lower half of the sample. In core 2, no large oil globule is reported. Most small and intermediate-sized oil globules are spread and trapped along the sample.

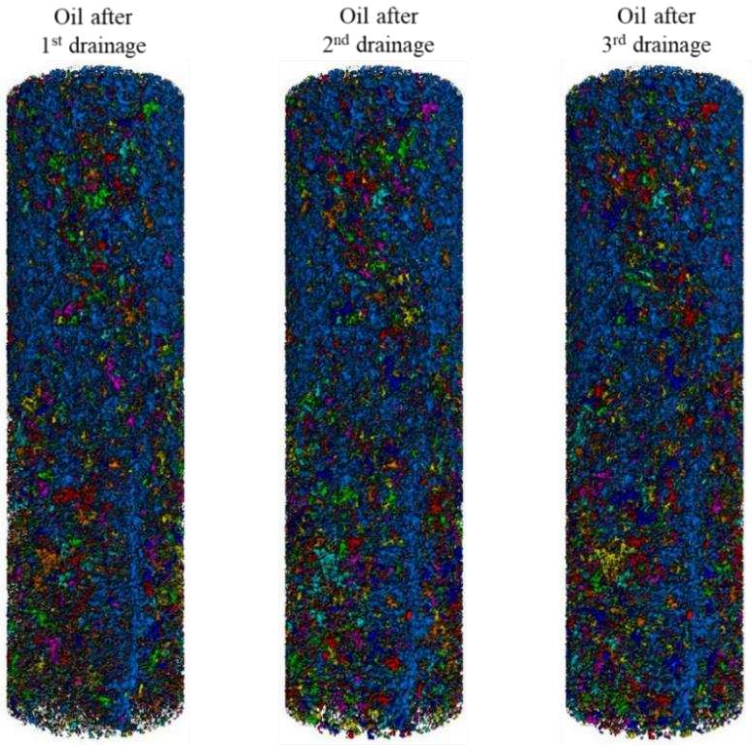

Figure 4.48: Oil globules at different stages of experiment 1.

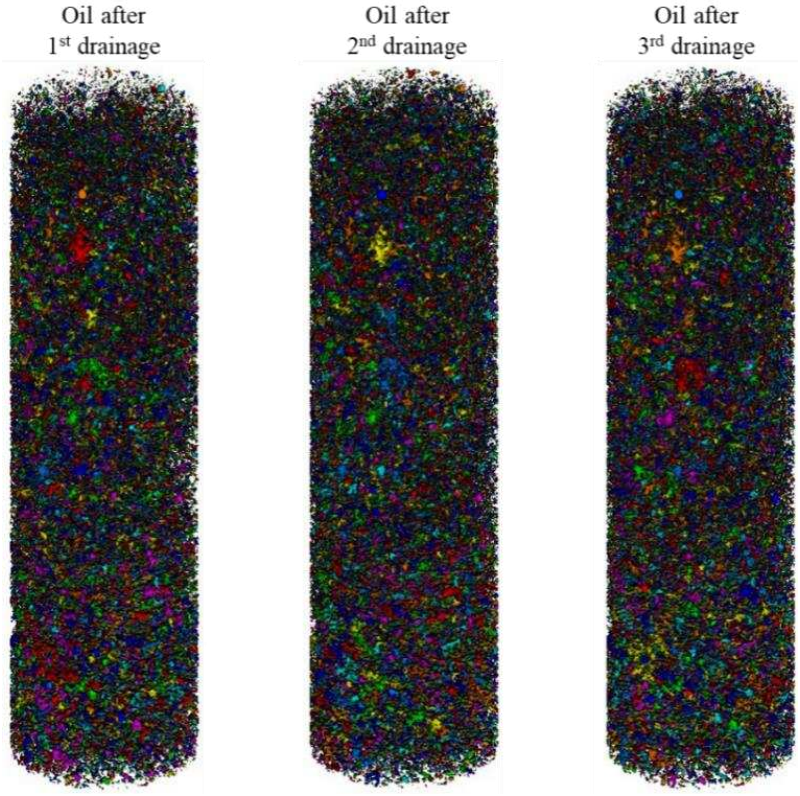

Figure 4.49: Oil globules at different stages of experiment 2.

Finally, axis connectivity for the pore space and oil phase were run in the direction of fluid injection. Figure 4.50 shows the connected pore space in the upper half and the fracture region of core 1 that became fully saturated with oil right after the first drainage stage. As the oil saturation increases, the oil ganglion increases, mainly in the lower half where the oil invaded the surrounding pore matrix. For core 2, on the other hand, no oil connectivity was reported due to the image resolution.

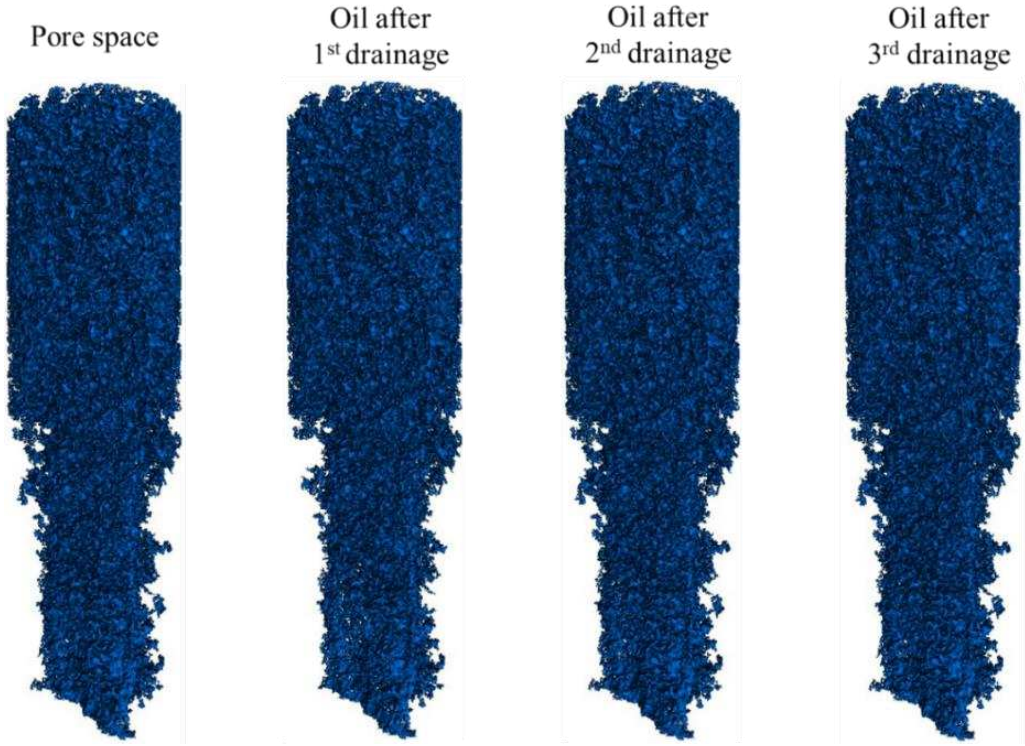

Figure 4.50: Connectivity of pore space and oil phase in the Z-direction at different stages of experiment 1.

4.2.3 Core flooding: Study 2B

This subsection evaluates the saturation profile, pore fluid occupancy, and size distribution of XG, water and oil clusters and globules after drainage and imbibition stages.

4.2.3.1 Saturation profiles

A multiphase saturation characterizes the initial experimental condition in this study line. In core 1, it corresponded to the last drainage stage of Study 2A, i.e., the core had a high saturation of oil and a low residual saturation of XG. In core 3, the sample also had a higher non-wetting phase saturation, and the wetting phase was water. The XG saturation in core 1 was lower than water in core 3. This is because the higher permeability of core 1 enabled the injection of oil at a higher flow rate, increasing the efficiency of oil-to-polymer displacement in this sample. In the end, it was compared the impact of the residual saturation of the wetting phase and the pore space characteristics in the cake formation.

Figures 4.51 and 4.52 illustrate the porosity profile and the saturation profiles of the wetting and non-wetting phases after each cycle of fluid injection in cores 1 and 3, respectively. Like Study 2A, the porosity profile of core 3 corresponds to the initial water saturation. Core 3 also presented a narrower range of porosity than core 1.

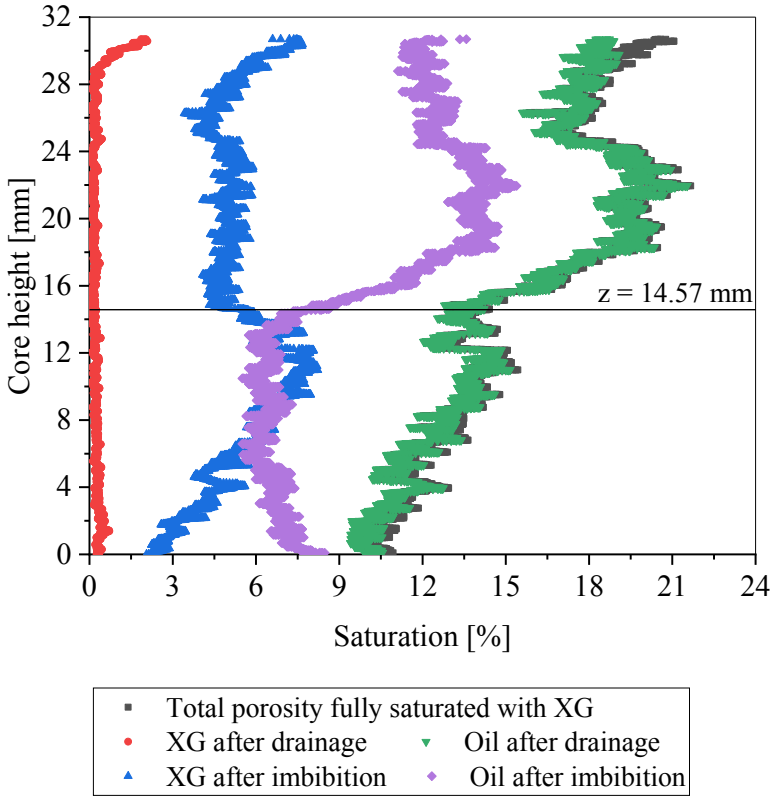

Figure 4.51: Porosity, XG, and oil saturation profiles at different stages of experiment 3.

The higher residual water saturation in core 3 before XG injection favored the imbibition mechanisms that enhanced the wetting saturation at this stage. The increase in wetting phase saturation by the imbibition mechanism is strongly dependent on the residual wetting phase in the pore space. Snap-off starts by swelling the remaining connected wetting layers, mainly located in the pore throats, and piston-like needs wetting phase connectivity, especially among the adjacent pores (Blunt, 2007). At the end of XG injection, core 3 remained mostly saturated with the polymer solution, while oil was the main phase in core 1.

The highest XG saturation was reported near the inlet of the core and at the beginning of the fracture in core 1. The retained polymer in the inlet face is a region highly saturated with the wetting phase, favoring the imbibition mechanisms. The fracture, in turn, is also a favorable region for XG-to-oil displacement due to its low frictional resistance.

Two distinct saturation regions of XG were noticed in core 3. In the upper half of the sample, the XG saturation was higher than the oil saturation, while the lower half showed the opposite

trend. One may infer a higher pore space connectivity in the upper half of this core. By putting numbers in perspective, two regions with similar initial water saturation and average porosity of 16% were compared. The average XG saturations for the upper and lower half were 11 and 6%, respectively. According to Blunt (2007), narrow throats holding thin wetting layers and few pore connectivity decrease the performance of snap-off and piston-like imbibition processes.

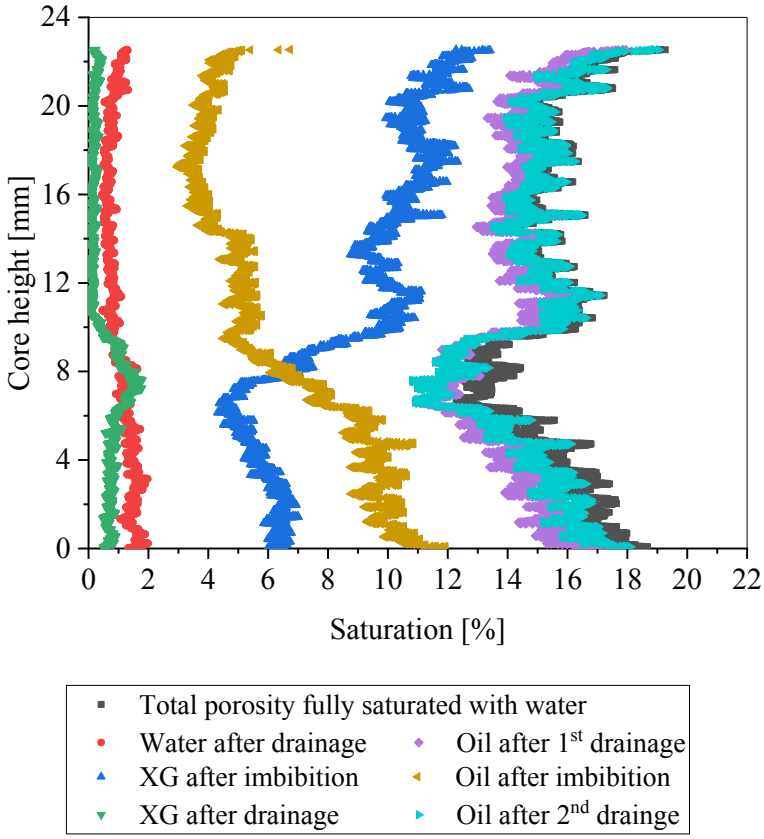

Figure 4.52: Porosity, water, XG, and oil saturation profiles at different stages of experiment 4.

After the second oil injection, the residual XG 0.2% (m/m) saturation profile corroborated with the inferred pore space connectivity of core 3. The lower half of the core presented higher residual XG saturation, mainly from z = 10 to 6 mm. Both Blunt (2017) and Dandekar (2013) say that the residual wetting phase is usually placed in small pores, narrow regions, and crevices after a drainage process.

The oil saturation profiles indicate that most pore spaces were fully saturated with oil after the drainage stages. It is because they presented a similar trend as the core porosity profiles. After polymer injection, the higher oil saturation was reported in the less connected region of core 3. Most of this saturation could be attributed to the trapped oil in the pore space, as discussed in section 4.2.3.2

Finally, Table 4.19 lists the average residual saturation of wetting and non-wetting phases after each stage of fluid injection in both cores.

Table 4.19: Residual wetting and non-wetting phases after oil and XG injections in cores 1 and 3.

After	Core 1		Core 3	
	Residual phase [%]			
	XG	Oil	*Water*/XG	Oil
1st drainage	1.768	98.232	*6.671*	93.329
Imbibition	35.144	64.856	58.485	41.515
2nd drainage	---	---	3.279	96.721

4.2.3.2 Pore fluid occupancy, cluster, and globule size distributions

(a) Pore fluid occupancy

Hereinafter, for core 1, the discussion about pore fluid occupancy and size distributions of oil and XG clusters and globules related to the first polymer injection and the oil injections is the same as in Study 2A. So, only the topics regarding the fluid arrangements from the second XG injection will be presented for this sample.

Figure 4.53 shows the size distribution of pores occupied by XG after both the oil and the second XG injections in core 1. A narrower range of size distribution was noticed at these stages. While the frequency of small and intermediate-sized pores with polymer increased after drainage, the opposite was reported after imbibition. In this later, the highest frequency of pore occupancy (13.64%) corresponded to large pores ranging from 5.47 to 8.91×10^5 μm^3. During imbibition, larger pores were first filled by the wetting phase as lower capillary pressure is needed to be overcome to invade them. Some intermediate-sized pores were also filled, and almost no small pores were not.

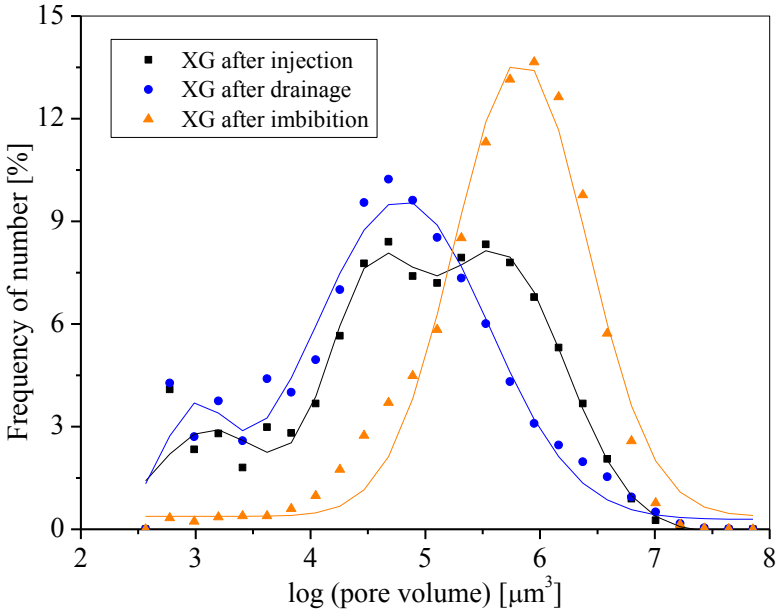

Figure 4.53: Pores occupied by XG 0.2% (m/m) after different injection stages in sample 1.

The polymer also filled the fracture in core 1 as its high connectivity enables an efficient polymer-to-oil displacement, as Figure 4.54 illustrates.

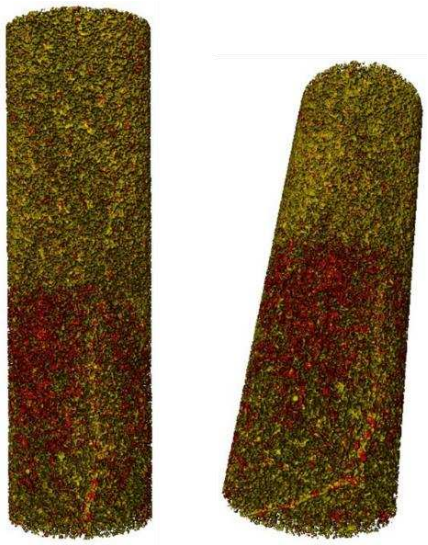

Figure 4.54: XG (yellow) and oil (red) arrangement in the pore space of core 1 after XG 0.2% (m/m) injection.

In core 3, Figure 4.55, although the water was mostly pushed to small pores later the first drainage, some residual saturation was noticed in intermediated and large-sized pores. It was attributed to the pore roughness and some possible thin throats connected to those pores.

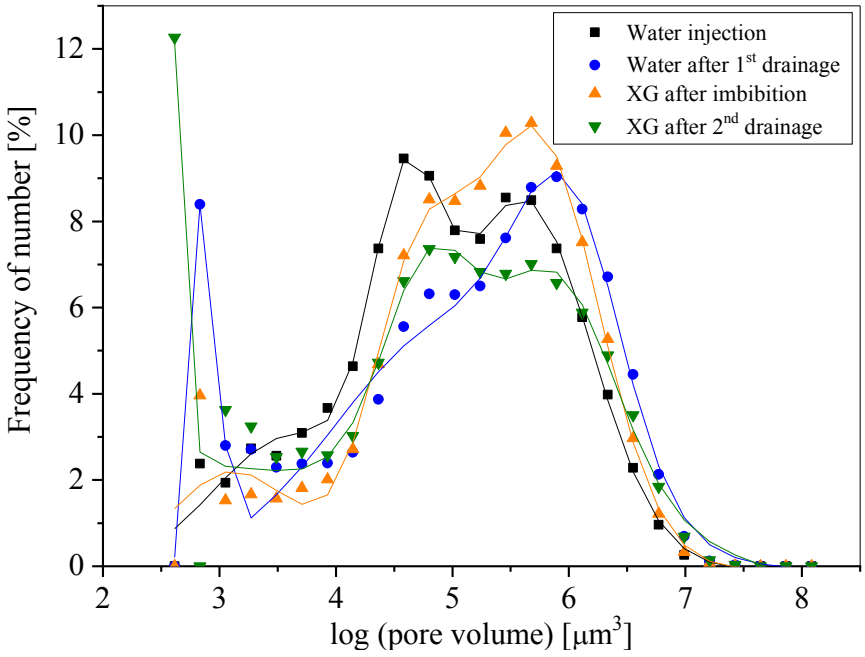

Figure 4.55: Pores occupied by XG 0.2% (m/m) and water after different injection stages in sample 3.

The number of pores filled by XG increased from 45,371 (after oil injection) to 228,079 (after imbibition). Most of these pores were the large ones. Lastly, the widest pore size distribution was observed after the second oil injection. Some XG were allocated into intermediate-sized pores, while most were into the smallest pores. An average of 12.27% of the pores filled by polymer had a size range from 4.12 to 6.80x10^2 µm^3 at this stage.

The pore fluid occupancy regarding the oil phase in the pore space was different in each core. As Table 4.20 lists, the number of pores occupied by oil after the XG injection increased in core 1 and decreased in 3. Core 1 presented higher oil saturation before XG injection, so more oil phase was prompt to be disconnected by the polymer rearrangement in the pore space once the stress caused by the injection was removed. The disconnected oil tends to be allocated in small pores, as Figure 4.56 shows for core 1.

Table 4.20: Number of pores occupied by oil after different injection stages in samples 1 and 3.

Oil after	Core 1	Core 3
1st drainage	718,270	594,645
Imbibition	742,205	570,067
2nd drainage	---	606,167

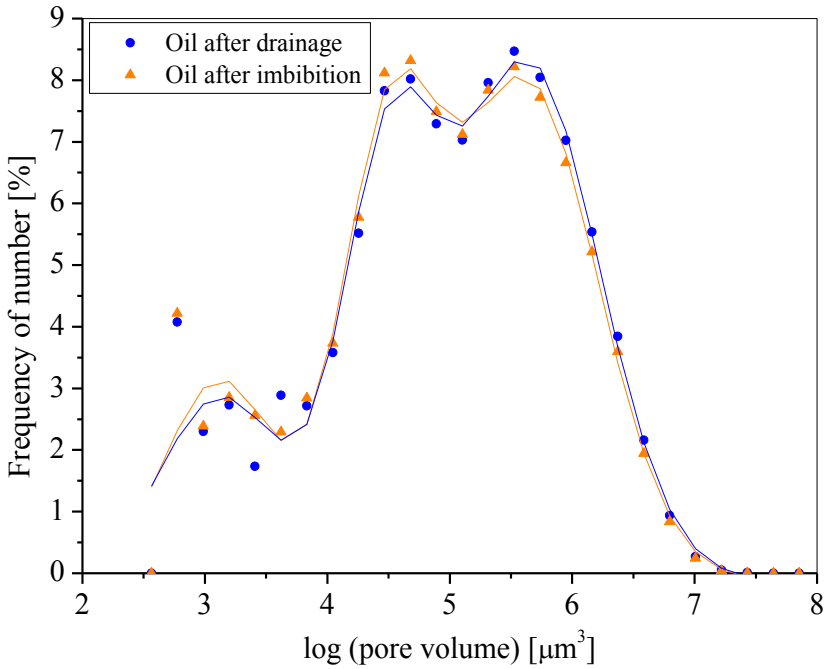

Figure 4.56: Pores occupied by oil after different injection stages in sample 1.

In core 3, in contrast, the trend of oil-filled pores kept constant and followed a similar behavior as the pore size distribution of this sample (Figure 4.57). It means that although the non-wetting phase saturation changed in the drainage and imbibition processes, the oil placement in the pore space was almost the same.

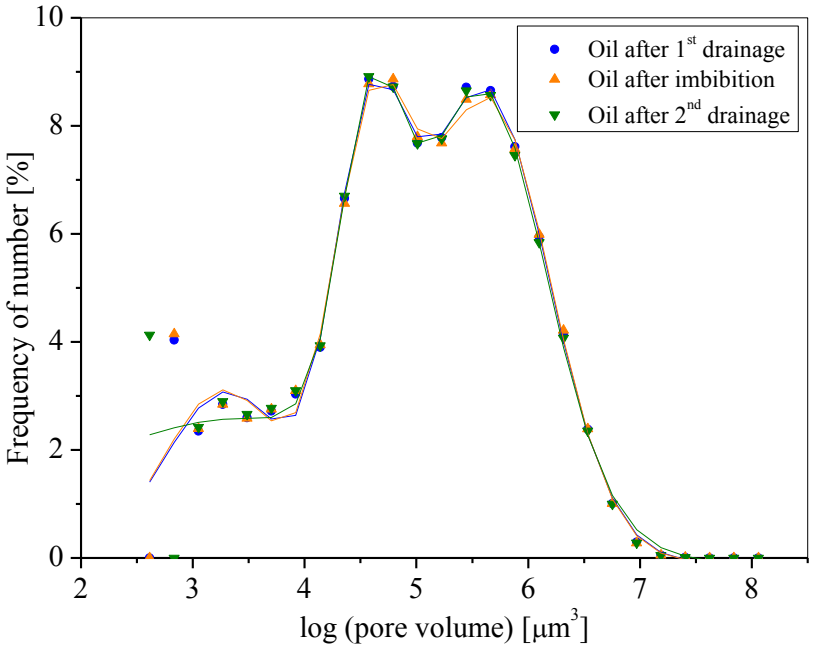

Figure 4.57: Pores occupied by oil after different injection stages in sample 3.

(b) Cluster size distribution

Figures 4.58 and 4.59 show the size distribution of the residual wetting clusters in cores 1 and 3, respectively. At the end of drainage, core 1 presented a lower number (43,840) and larger XG clusters, mostly allocated in intermediate-sized pores. Once again, the retained polymer near the inlet face of this sample was considered a large XG cluster.

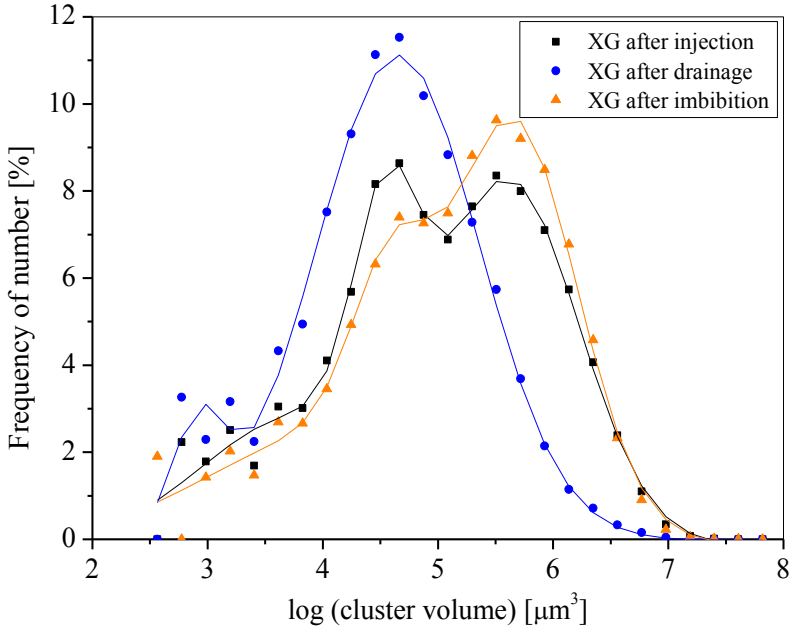

Figure 4.58: XG 0.2% (m/m) cluster size distribution after different injection stages in sample 1.

In core 3, on the other hand, the higher residual water saturation was reported as smaller clusters spread along the core. A multiple cluster occupancy occurred as the number of clusters (219,443) was higher than the number of water-filled pores (175,321). An average of 21.6% of the number of clusters was ranged from $6.82x10^2$ to $1.13x10^3$ μm^3.

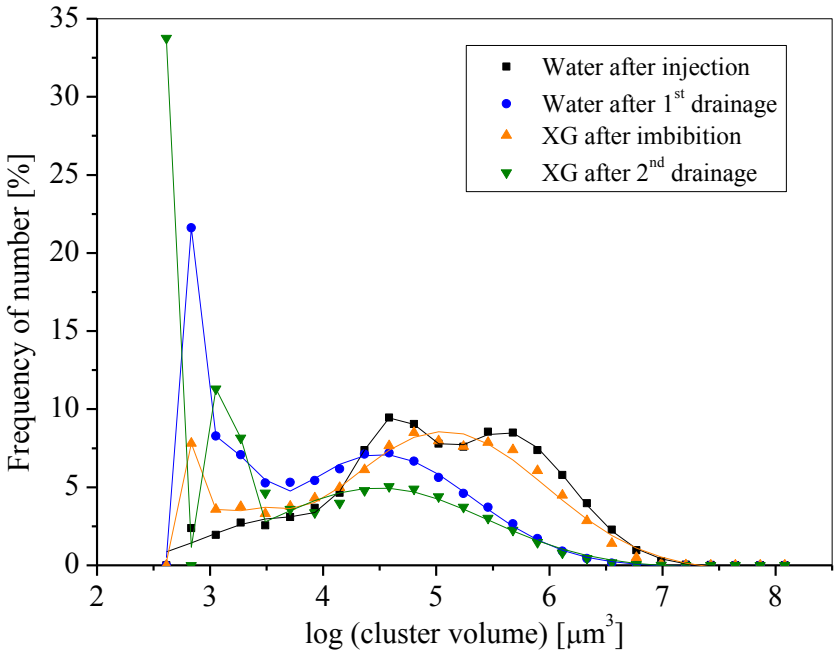

Figure 4.59: XG and water cluster size distribution after different injection stages sample 3.

Once the XG was injected, and the polymer saturation increased, both the number and volume of wetting clusters raised. It can be justified by the tendency of the polymer to occupy large pores and by the re-connections among the residual and the injected XG. While the highest frequency of large clusters was reported in core 1, an increase in the percentage of intermediate-sized and a significant decrease in small ones were verified in core 3.

A multiple cluster occupancy was again noticed at this stage for both cores. More polymer ganglions than the pores filled by XG were accounted for, suggesting that more than one cluster was allocated in the same pore. It was even more evident in core 3, as the higher number of total and small clusters were reported in this sample. This occurrence was attributed to the residual oil saturation that hindered the formation of large wetting clusters.

Lastly, the second drainage in core 3 resulted in the smallest wetting saturation and number of wetting clusters in this sample. Graphically, the broadest distribution of XG cluster volume was noticed, characterized by the highest percentage of small-sized clusters mostly disconnected and placed in small pores. 33.8% of the total residual clusters had an average volume of $5.47x10^2$ μm^3.

Table 4.21 lists the number of oil clusters after each displacement stage. After the first drainage, the oil saturation increased to 90% in both cores, forming larger oil clusters. Then, the injection of XG trapped most of the oil ganglions in the pore space, resulting in small-sized

clusters. For a water-wet rock sample, as the wetting phase saturation increases, its layers placed in the narrowest regions and throats occupy the center of the pore space where previous oil resided, pinning the non-wetting phase that can no longer move. The oil trapping can also occur inside the void spaces when the wetting phase fills the throats that surround the pore. In the case of a piston-like mechanism, the trapped oil can happen when the frontal advance provides a pincer movement letting some region of the pore space be surrounded by oil (Blunt, 2017).

Table 4.21: Number of oil clusters after different injection stages in samples 1 and 3.

Oil after	Core 1	Core 3
1st drainage	720,576	646,823
Imbibition	972,833	919,724
2nd drainage	---	619,199

The histogram curves of both cores outline the high frequency of small-sized oil ganglions shifted to the left side after polymer injection (Figures 4.60 and 4.61). The highest frequency of clusters (10.5%) corresponded to the smallest ones with an average volume of $4.24x10^2$ μm^3 in both cores. The wider frequency of small ganglions, in turn, was reported in core 3. Despite the lower number of oil-filled pores and the lower residual non-wetting saturation, thinner troats and a higher aspect ratio characterized core 3, hindering oil displacement.

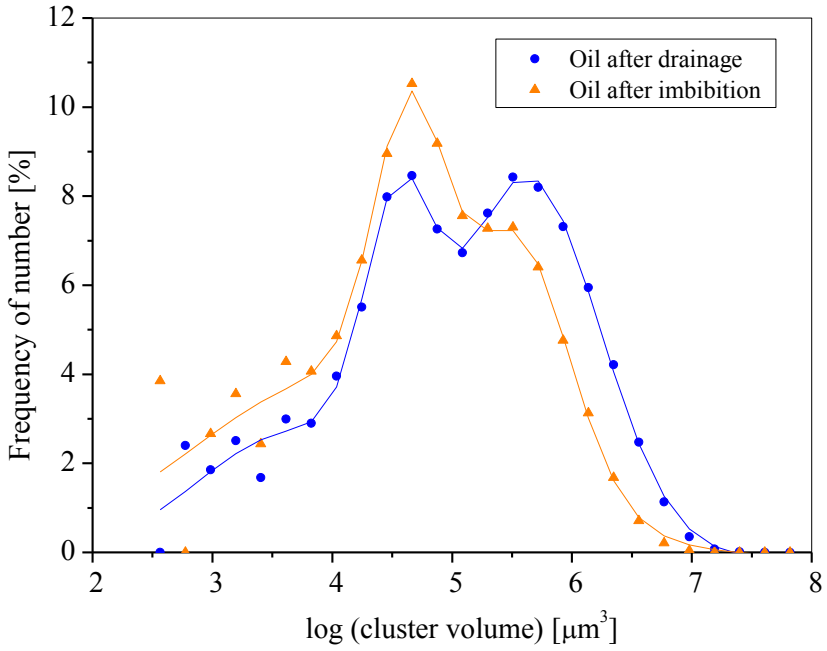

Figure 4.60: Oil cluster size distribution after different injection stages in sample 1.

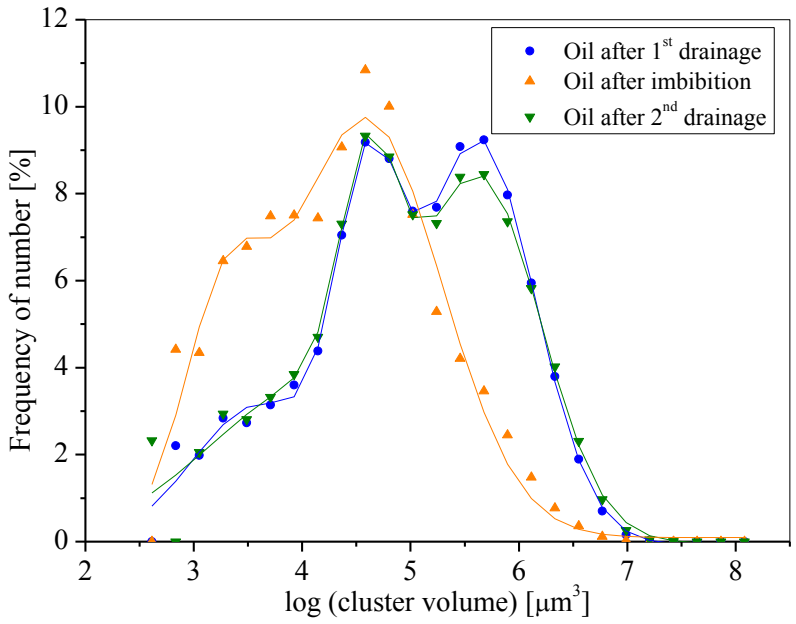

Figure 4.61: Oil cluster size distribution after different injection stages in sample 3.

The second oil injection in core 3 enabled the coalescence between the injected and the residual oil clusters as the non-wetting saturation in the pore space increased. It was seen as the number of oil clusters decreased while their size increased. The slight decrease in the frequency of large clusters compared to the first oil injection is due to the residual small wetting clusters placed in the narrow regions that impaired the formation of voluminous oil clusters.

Garing et al. (2017) reported a similar non-wetting phase re-connection and attributed it to the capillary re-equilibrium. Armstrong et al. (2016) stated that the oil ganglion coalesces and elongates in the flow direction as a function of capillary number.

Finally, Figures 4.62 and 4.63 show 3D images of the wetting and non-wetting phases and clusters before and after XG injection in both cores. In these stages, the higher wetting saturation is seen in core 3. The images correspond to a regular cube of 45.31 mm^3 extracted at 17.8 mm from the inlet of the cores. Water, XG, and oil phases are tagged as blue, yellow, and red colors, respectively. A different color identifies each cluster.

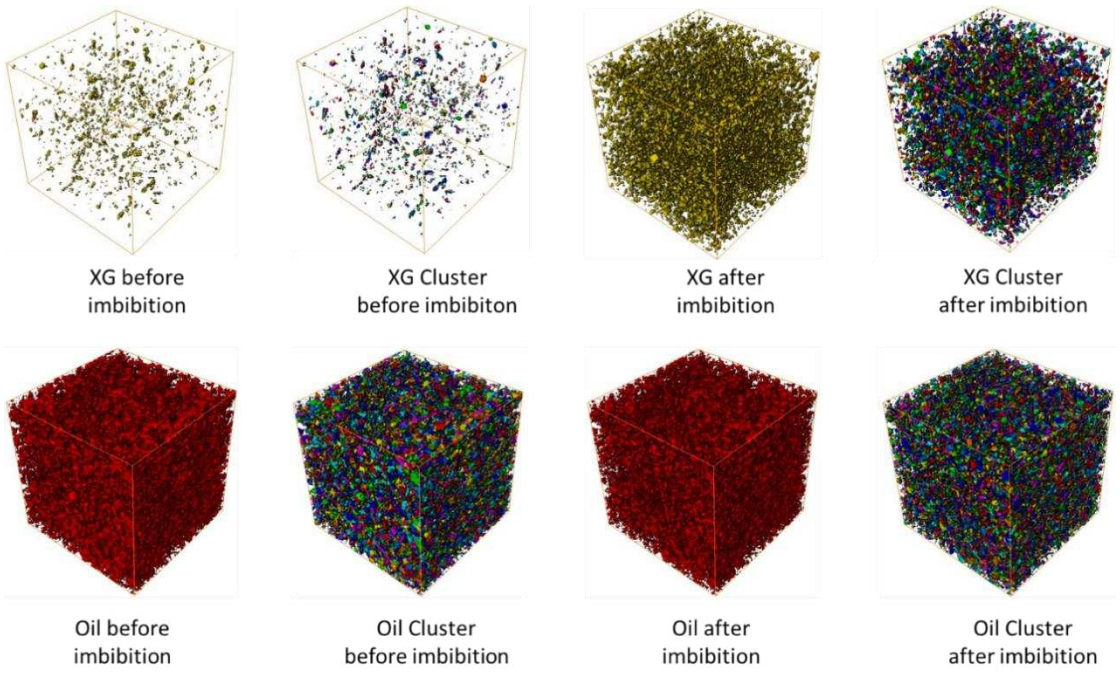

Figure 4.62: 3D images of wetting and non-wetting phases and their corresponding clusters before and after XG 0.2% (m/m) injection in core 1. XG is tagged as yellow, oil as red, and a different color depicts each cluster.

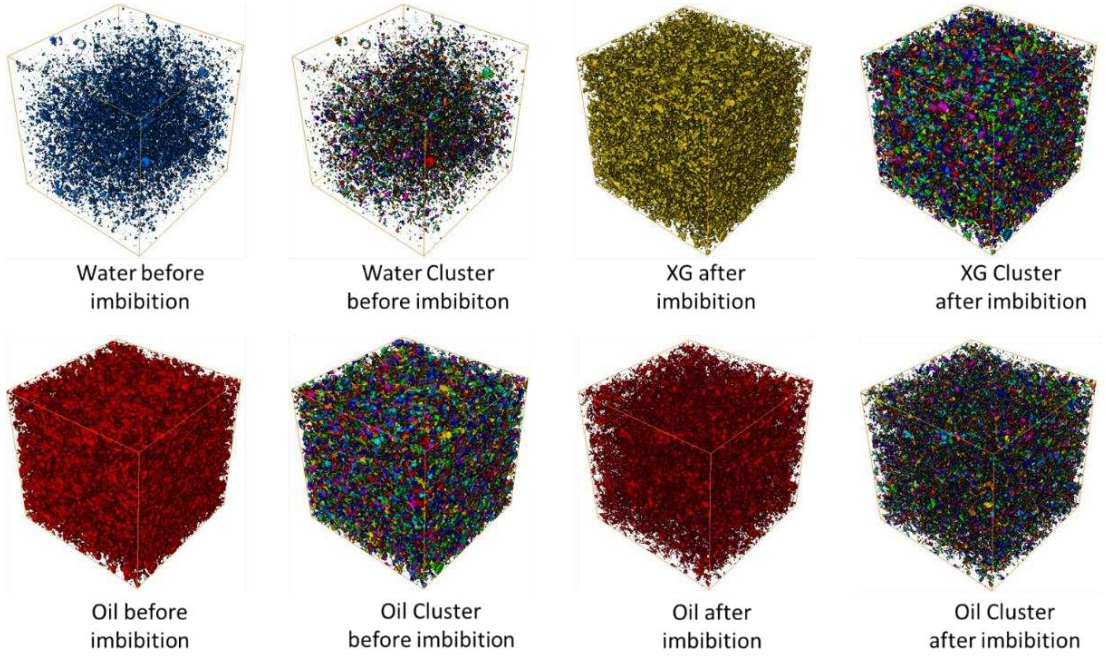

Figure 4.63: 3D images of wetting and non-wetting phases and their correspondent clusters before and after XG 0.2% (m/m) injection in core 3. Water is tagged as blue, XG as yellow, oil as red, and a different color depicts each cluster.

(c) Globule size distribution

The connected pore space in both samples presented a trend of similar size distribution, as shown in Figures 4.64 and 4.65 for core 1 and 3, respectively. Around 10% of connected pores have 10^2 µm^3 and 16.7% have 10^4 µm^3. After drainage, however, the profile of residual wetting globules differed in each core. Intermediate and small-sized globules predominated in cores 1 and 3, respectively.

The throat filling among pores favored the coalescence between the injected and residual XG, connecting the polymer phase and increasing the size of wetting globules after imbibition. This yielded the frequency of large-sized globules that occupied more than one pore—the number of globules was smaller than the number of pores occupied by them in both cores. In core 1, the formed globules were mostly allocated in large pores, and they were larger than the globules in core 3.

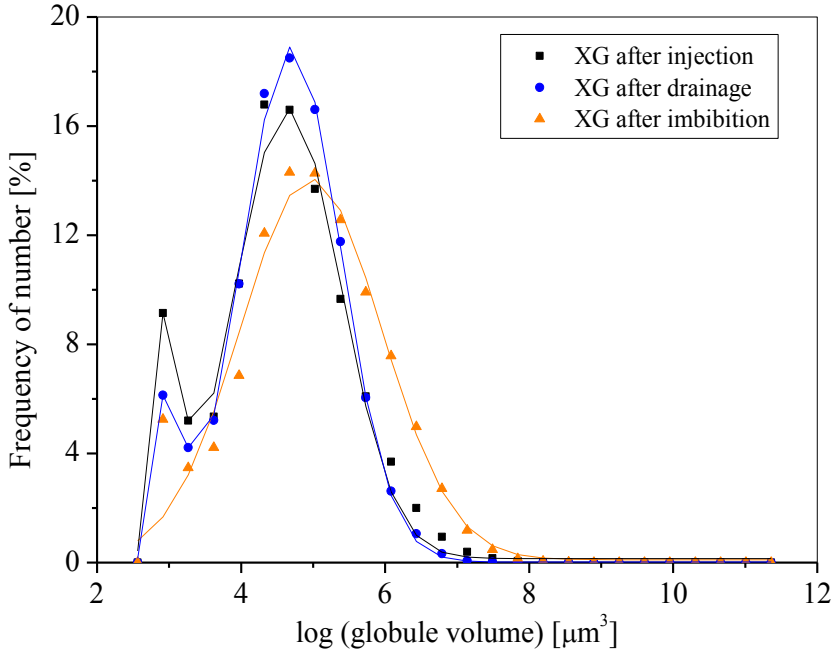

Figure 4.64: XG 0.2% (m/m) globule size distribution after different injection stages in sample 1.

In core 3, although the fraction of large wetting globules raised after polymer injection, most of them remained small. An average of 20% of the total residual XG globules was ranged from 9.14×10^2 to 2.03×10^3 µm^3. One may attribute that to the multiple oil entrapment in the narrow features of this sample, which hindered the wetting phase mobility and connectivity. The influence of oil entrapment in the XG connectivity was even more noticed after the oil injections when the highest frequency of smallest wetting globules was reported.

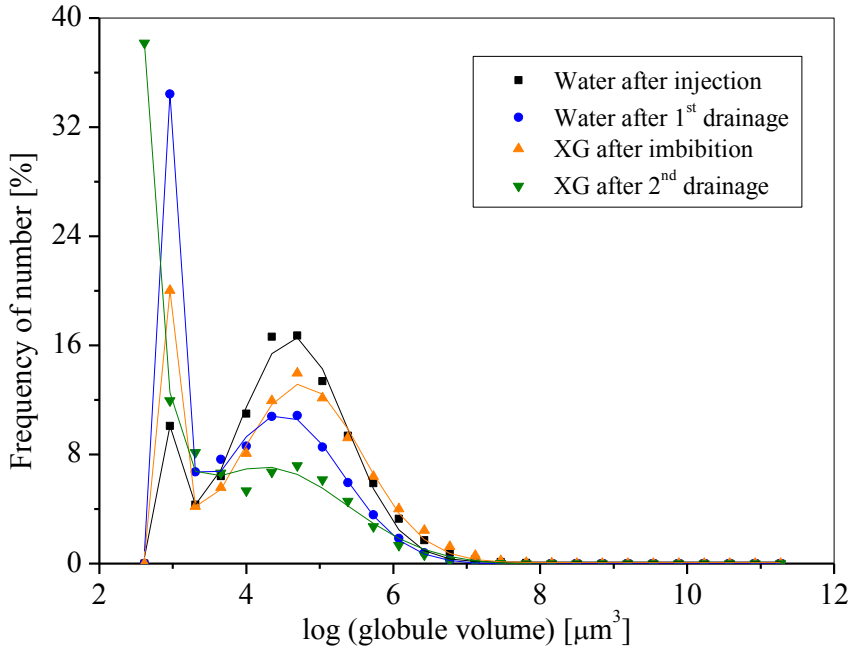

Figure 4.65: XG 0.2% (m/m) and water globule size distribution after different injection stages in sample 3.

Figure 4.66 illustrates the 3D spatial distribution of wetting globules. It shows the XG globules after polymer injection in core 1 and the water and XG globules after each fluid displacement in core 3. The disconnected XG globules after polymer injection due to the residual oil phase is noticed along both cores. Besides, it highlights the less connected region in the lower half of core 3 that remained filled with small wetting globules after the second oil injection. A color tags each globule.

After the first oil injection, the increase in oil saturation in almost all pores enabled the non-wetting connectivity in both cores. It was confirmed by the lower number of oil globules than oil-filled pores. The intermediate-sized globules are explained by the oil settle in well-connected regions. The small globules, in turn, might be placed in pores also saturated with the wetting phase and/or in poorly connected areas. Figures 4.67 and 4.68 illustrate the size distribution of oil globules at this stage: 10% have a size between $8x10^2$ and $2x10^3$ μm^3, and 16.6% were ranged from 2.1 to $4.9x10^4$ μm^3.

As the XG invaded the pore spaces, the polymer disconnected and trapped some oil globules. It increased the number of both the total and small residual oil globules. This latter was graphically seen by the narrowing of the size distribution of the residual oil globules toward the small volumes. The intermediate-sized globules can be explained by the regions that mainly remained saturated with oil at this stage.

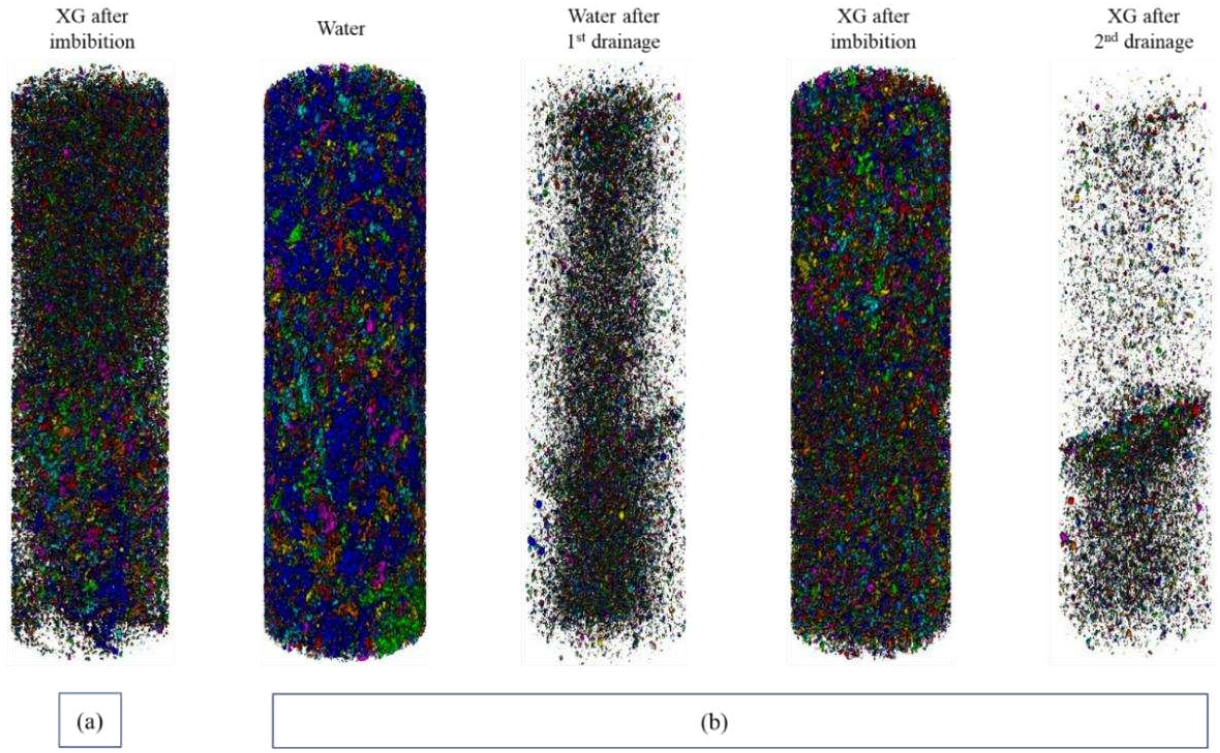

Figure 4.66: 3D spatial distribution of wetting globules: (a) XG after XG injection in sample 1; and (b) Water and XG after different injection stages in sample 3.

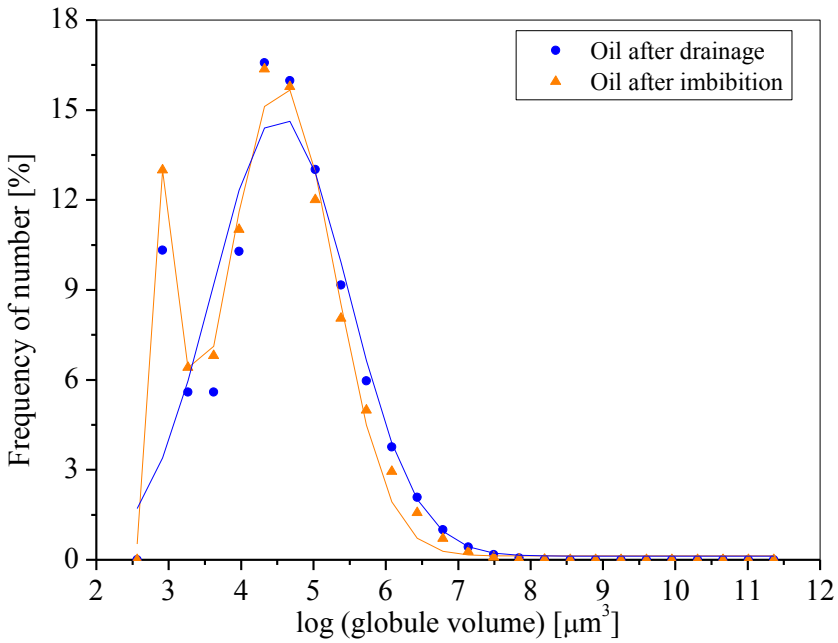

Figure 4.67: Oil globule size distribution after different injection stages in sample 1.

The second drainage in core 3 favored the oil globule growth again since the non-wetting phase mostly saturated the pore space. The number of oil globules decreased by more than a half to the previous stage (from 557,201 to 242,737) while their percentage with 10^4 and 10^5 order volumes increased. The fraction of the smallest globules was attributed to the small ones being placed in the less connected zone, where the residual polymer still occupies.

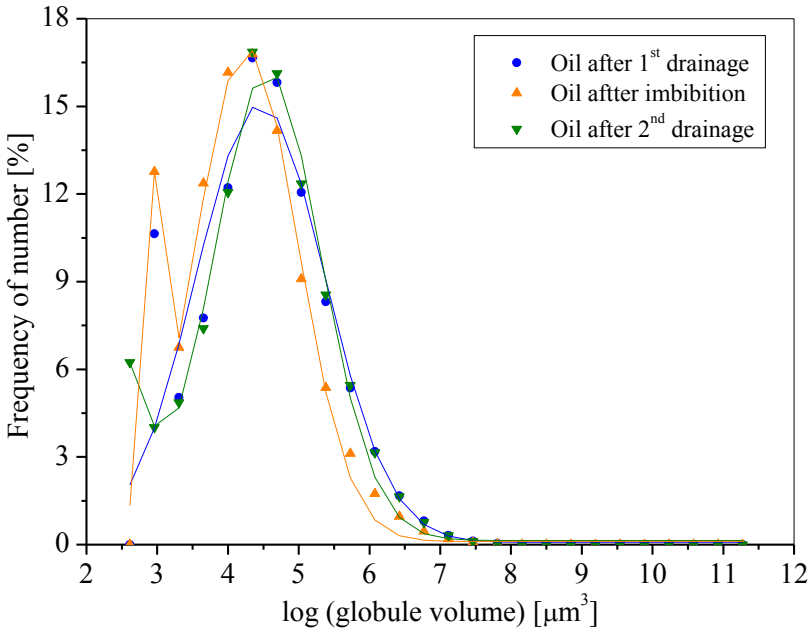

Figure 4.68: Oil globule size distribution after different injection stages in sample 3.

The 3D representations of oil globules are illustrated in Figure 4.69 for samples 1 and 3. Again, each globule is identified by a color.

Later the XG injection, the largest oil globules are seen at the top half and fracture regions of core 1 where most of the connected pores are placed. In core 3, they are mostly settled at the bottom half of the sample. After the second oil injection, larger oil globules are reported in the upper and lower half of core 3.

Finally, the connected phases in each core are reported in Figure 4.70. In core 1, it was seen only oil connectivity after the polymer injection. Its profile, in turn, resembles the connected pore space of this sample (Figure 4.50). In core 3, only oil connectivity after the first oil injection was noticed. After this stage, the residual polymer and oil phases hindered the formation of largely connected globules and, so, no connected phase was seen. In the weakly connected region in the lower half of core 3, neither polymer nor oil connectivities were verified.

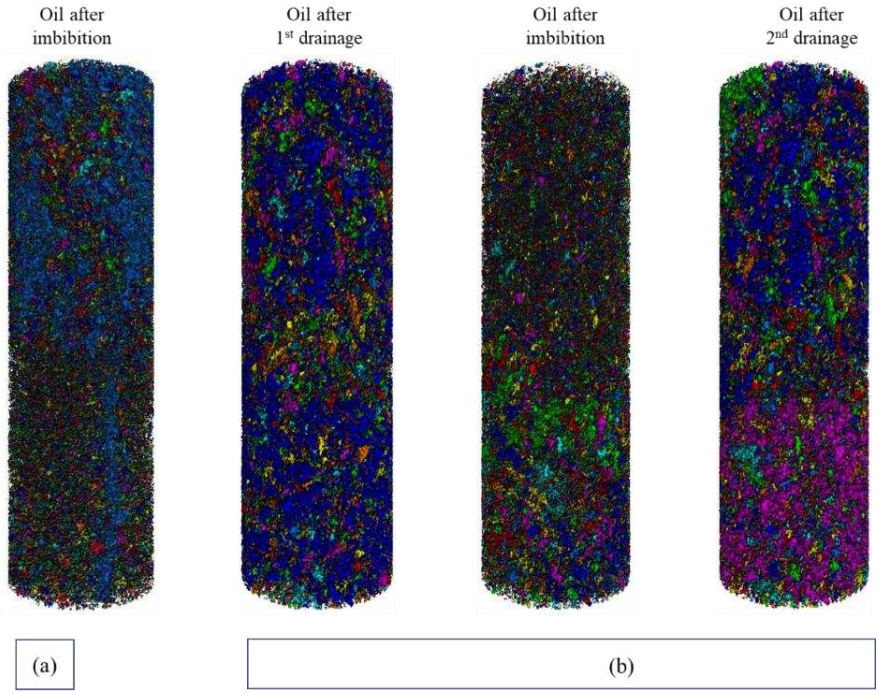

Figure 4.69: 3D spatial distribution of non-wetting globules: (a) Oil after XG injection in sample 1; and (b) Oil after different injection stages in sample 3.

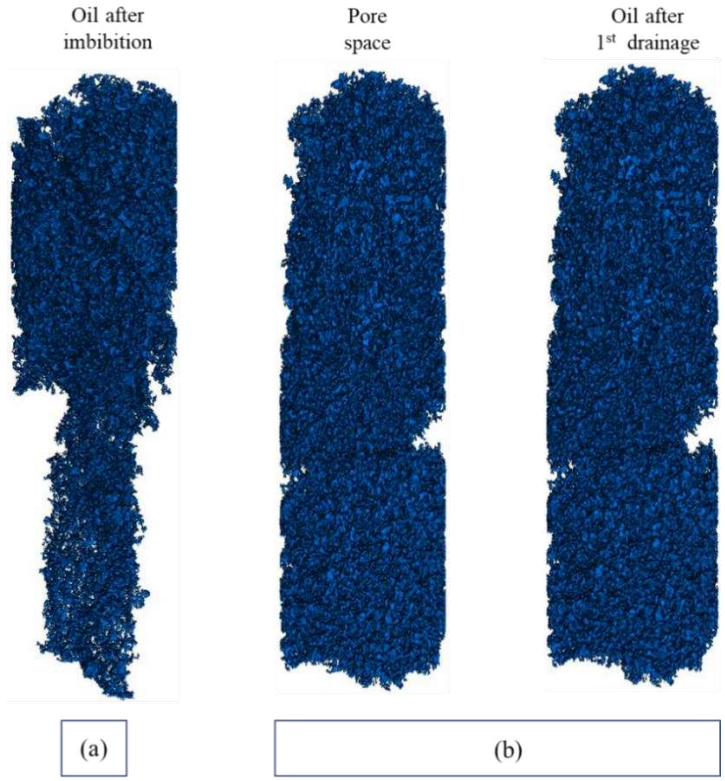

Figure 4.70: Connectivity phase in the Z-direction of: (a) oil phase after XG injection in core 1; and (b) pore space and oil after the first drainage in core 3.

5. Conclusions

This section summarizes the main findings regarding the flow of non-Newtonian solutions and suspensions through porous media. Two approaches (Study 1 and 2) were successfully designed and performed to investigate the interplayed effect of fluid rheology and pore space characteristics on inner and external cake formation in overbalanced drilling operations.

In Study 1A, XG 0.2 and 0.4% (m/m) flow through 50 and 120 μm ceramic filters was analyzed as a function of pressure drop using HTHP filter press. The goal was to evaluate the change in medium permeability by polymer retention and the effect of viscous and inertial forces during polymeric flow, resembling the inner filter cake formation. In Study 1B, the influence of polymer concentration on $CaCO_3$ 5% (v/v) suspensions flowing through 50 and 120 μm ceramic filters as a function of pressure drop was also analyzed. For this, a model to estimate cake and medium permeabilities as a function of the pressure drop was proposed. The goals were to evaluate the properties of external cakes and the change in membrane permeability by polymer and solid clogging in the formation of inner cakes. In Study 2A, XG 0.2 and 0.4% (m/m) were injected in miniature carbonate core plugs to reproduce the formation of inner cakes. Then different mineral oil flow rates were performed, and pore fluid occupancy was imaged using a Heliscan micro-CT system. A novel methodology was proposed to eliminate the partial volume effect and account for the porosity from micropores. The goal was to analyze the impact of oil flow rate on polymer (cake) displacement once the well is put in operation. In Study 2B, XG 0.2 % (m/m) was injected in similar carbonate cores as in Study 2A with different initial saturation conditions. The aim was to investigate the impact of both wetting and non-wetting fluid saturation in the formation of inner filter cakes.

In Study 1A, Darcy's law better characterized the XG flow. The inertial effect became more noticeable at higher pressure drops and larger pores. Polymer retention, mainly by adsorption and mechanical entrapment, was noticed by decreasing membrane permeability and the filtrate consistency index. At lower pressure drops, medium permeability seemed to be more influenced by XG concentration than by the pore size. The ceramic filter of 120 μm still presented higher permeability than the 50 μm under this condition. As the pressure gradient increased, the difference between medium permeability rates shortened, and at the highest pressure, there was no significant difference between them.

In Study 1B, the proposed model showed good behavior to estimate medium and external cake permeabilities after the suspension flow. Medium permeability decreased as the pressure drop increased. However, this trend was less sensitive in the range of high pressures for the different experimental conditions (concentration of XG and permeability of ceramic filters). The rheology of the suspensions played an important role in changing the permeability of membranes. The lower the polymer concentration, the lower the permeability of both 50 and 120 μm filters. It was attributed to the pore body and throat clogging by $CaCO_3$ during the flow of less flow resistant

suspensions. The medium permeability decreased more because of the clogging effect of solids than because of XG solutions only.

Cake permeability for both polymer concentrations decreased as a function of pressure drop. The suspension rheology also played an important role in cake formation. Cakes formed by suspensions of XG 0.4% (m/m) presented higher permeability and porosity values. They were also influenced by the average pore size of the ceramic filter. The latter, however, did not influence the cake formed by the suspension of XG 0.2% (m/m). Also, cake permeability was less variable in the range of high pressures.

The specific cake resistance increased with the pressure drops for all $CaCO_3$ suspensions and ceramic filters, indicating cake compressibility. The highest and widest range of values of specific cake resistance was noticed for the cake formed by XG 0.2% (m/m)_120 μm. The values of specific cake resistance were also smaller than the values of medium resistance for all experimental conditions.

The rheological characterization of the filtrate showed that the consistency and behavior indexes decreased and increased in relation to the rheological parameters of the suspension before filtration, respectively.

In Study 2A, the proposed methodology to eliminate the partial volume effect was successfully applied. As different cycles of oil flow rate were performed, the number of pores occupied by XG in the centers decreased. The polymer was pushed to small pores, while oil resided in the large and intermediated regions. In core 1, the fracture region was filled by oil first since a lower threshold capillary pressure was required for XG 0.2% (m/m) displacement. Polymer retention in the inlet face of cores 1 and 2 was noticed. This effect was higher in core 2 since the more concentrated solution was injected in the less permeable core. The retained polymers were characterized as intermediate-sized and large globules trapped in the pore space.

In core 1, the well-connected pores favored phase mobility. The coalescence of residual polymer clusters and globules after the second and third drainage stages was reported due to the mobilization of trapped XG 0.2% (m/m) ganglia. As oil saturation increased, the size and frequency of larger oil clusters and globules also increased. In the lower half of the sample, the fracture was first filled by oil, and as the flow rate raised, more matrix pores were invaded. In contrast, in core 2, both XG 0.4% (m/m) and oil showed lower mobility, resulting in a multiphase cluster and globule occupancy along the core height.

In Study 2B, the efficiency of XG 0.2% (m/m)-to-oil displacement was influenced by the initial saturation condition of the core and the pore space characteristics. Higher initial wetting saturation favored XG saturation after its injection, mainly in the well-connected regions. While the increase in the XG saturation mostly occurred in wetting zones, oil invasion occupied most of the pores right after its first injection. Besides, there was an increase in the frequency of small oil clusters in cores 1 and 3 after XG injection. The invaded XG disconnected most of the previous oil clusters

that became trapped in the pore space. It was more noticeable in core 3 due to its smaller pores and higher aspect ratio. Neither wetting nor non-wetting phase connectivity was reported at the end of imbibition in this sample.

Finally, based on the experimental findings, both the mud rheology and the petrophysics characteristics of the reservoir play an important role in the inner and the external cake formation. The fluid rearrangement in the pore space is influenced by the initial fluid saturation and the flow rate of the displacing phase. The drilling mud and oil mobility are more prone to occur in reservoirs characterized by large and well-connected pores. High viscous muds tend to damage a lower portion of the reservoir, although the pores in the invaded zone, mainly the low connected ones, may be clogged. Thus, an appropriate viscosified drilling fluid should be used in overbalanced drilling operations to decrease the fluid loss and, subsequently, formation damage.

✓ Proposal for future research: (i) evaluate the influence of pressure drop above $14x10^5$ Pa in the flow of non-Newtonian suspensions; (ii) evaluate the influence of temperature in filtration of non-Newtonian suspensions; (iii) estimate the compressibility index for cakes formed from non-Newtonian suspensions; (iv) perform in-situ polymer and oil injections, and (v) estimate the core permeability after polymer injection using pore network extraction and models.

6. References

Agi, A., Junin, R., Gbonhinbor, J., Onyekonwu, M., 2018, Natural polymer flow behavior in porous media for enhanced oil recovery applications: a review, Journal of Petroleum Exploration and Production Technology, v. 8, p. 1349-1362, Doi: 10.1007/s13202-018-0434-7

Al-Hajri, S., Mahmood, S.M., Adbulelah, H., Akbari, S., 2018, An Overview on Polymer Retention in Porous Media, Energies, v. 11, Doi: 10.3390/en11102751

Andersoon, L., 2018, Defining a Novel Pore-Body to Pore-Throat "Morphological Aspect Ratio" that Scales with Residual Non-Wetting Phase Capillary Trapping in Porous Media, Advances in Water Resources, Doi: 10.1016/j.advwatres.2018.10.009

Armstrong, R.T., McClure, J.E., Berril, M.A., Rücker, M., Schlüter, S., Berg., S., 2016, Beyond Darcy's law: The role of phase topology and ganglion dynamics for two-fluid flow, Physical Review E, v. 94, 043113, Doi: 10.1103/PhysRevE.94.043113

Arshadi, M., Zolfaghari, A., Piri, M., Al-Mustasheri, G.A., Sayed, M., 2017, The effect of deformation on two-phase flow through proppant-packed fractured shale samples: A micro-scale experimental investigation, Advances in Water Resources, v. 105, p. 108-131, Doi 10.1016/j.advwatres.2017.04.022

Arshadi, M., Khishvand, M., Aghaei, A., Piri, M., Al-Muntasheri, G.A., 2018, Pore-Scale Experimental Investigation of Two-Phase Flow Through Fractured Porous Media, Water Resources Research, v. 54, p. 3602-3631, Doi: 10.1029/2018WR022540

Asme Shale Shaker Committee, 2005, Drilling Fluids Processing Handbook, first edition, Gulf Professional Publishing

Azar, J. J., Samuel, G. R., 2007, Drilling Engineering, 2 ed., Oklahoma, Ed. Pennwell

Balhoff, M., Wheeler, M.F., 2009, A Predictive Pore-Scale Model for Non-Darcy Flow in Porous Media, Annual Technical Conference and Exhibition of the Society of Petroleum Engineers, California, USA

Berg, S., Armstrong, R.T., Georgiadis, A., Ott, H., Schwing, A., Neiteler, R., Brussee, N., Makurat, A., Rucker, M., Leu, L., Wolf, M., Khan, F., Enzmann, F., Kersten, M., 2015, Onset of Oil Mobilization and Non-wetting Phase Cluster Size Distribution, Petrophysics, v. 56, p. 15-22

Blunt, M.J., 2017, Multiphase Flow in Permeable Media: A Pore-Space Perspective, first edition, Cambridge University Press

Brown, J.G., 1975, X-rays and their applications, Plenum Published Corporation, New York, Doi: 10.1007/978-1-4613-4398-1

Calabrez, N.D., 2013, “Filtração e invasão de fluidos de perfuração: estudo comparativo, caracterização da torta e modelagem”, thesis, Federeal University Rural of Rio de Janeiro, Seropédica/RJ

Castro, A. R.; Radilla, G., 2017, Non-Darcian flow of shear-thinning fluids through packed beads: Experiments and predictions using Forchheimer´s law and Ergun’s equation, Advances in Water Resources, v. 100, p. 35-47, 2017, Doi: 10.1016/j.advwatres.2016.12.009

Chesser, B.G., Clark, D.E., Wise, W.V., 1994, Dynamic and Static Filtrate-Loss Techniques for Monitoring Filter-Cake Quality Improves Drilling-Fluid Performance, SPE Annual Technical Conference and Exhibition, New Orleans, USA

Chhabra, R.P., Richardson, J.F., 2008, Non-Newtonian Flow and Applied Rheology: Engineering Apllications, second edition, Butterworth-Heinemann

Chinellato, G.F., Belila, A.M.P., Basso, M., Souza, J.P.P., Vidal, A.C., 2020, A taphofacies interpretation of shell concentrations and their relationship with petrophysics: A case study of Barremian-Aptian coquinas in the Itapema Formation, Santos Basin-Brazil, Marine and Petroleum Geology, v. 116, Doi: 10.1016/j.marpetgeo.2020.104317

Civan, F., 2007, Reservoir Formation Damage: fundamentals, modeling, assessment, and mitigation, second edition, Gulf Professional Publishing

Cnudde, V., Boone, M.N., 2013, High-resolution X-ray computed tomography in geosciences: A review of the current technology and applications, Earth-Science Reviews, v. 123, p. 1-17, Doi: 10.1016/j.earscirev.2013.04.003

Cosentino, L., 2001, Integrated Reservoir Studies, Editions Technip, Paris

Cruz, C.C.C., Boy, G.S., Pires, A.P., 2011, “Análise dos Efeitos dos Modelos de Forchheimer Quadrático e Cúbico no Comportamento da Pressão de Poços de Petróleo“, “6° Congresso Brasiliero de Pesquisa e Desenvolvimento em Petróleo e Gás”, Statal Univeristy of Norte Fluminense Darcy Ribeiro

Damasceno, J.J.R., 1985, “Análise do Desempenho de Filtros sedimentadores”, thesis, Federal Univeristy of Rio de Janeiro, Rio de Janeiro/RJ

Dandekar, A.Y., 2013, Petroleum Reservoir Rock and Fluid Properties, second edition, CRC Press Taylor & Francis Group

Dang, T.Q.C., Chen, Z., Nguyen, T.B.N, Bae, W., 2014, Investigation of Isotherm Polymer Adsorption in Porous Media, Petroleum Science and Technology, v. 32, p. 1626-1640, Doi: 10.1080/10916466.2010.547910

Dewan, J.T., Chenevert, M.E., 2001, A model for filtration of water-based mud during drilling: determinations of filter cake parameters, Petrophysics, v. 42, p. 237-250

Dodge, Y., 2008, The Concise Encyclopedia of Statistic, Springer

Ezeakacha, C.P., Salehi, S., 2017, Experimental and statistical investigation of drilling fluids loss in porous media-part 1, Journal of Natural Gas Science and Engineering, Doi: 10.1016/j.jngse.2017.12.024

Fattah, K.A., Lashin, A., 2016, Investigation of mud density and weighting materials effect on drilling fluid filter cake properties and formation damage, Journal of African Earth Science, v. 117, p. 345-357, Doi: 10.1016/j.jafrearsci.2016.02.003

Fehlberg, E., 1968, Classical Fifth-, Sixth-, Seventh-, and Eighth-Order Runge-Kutta Formulas with Stepsize Control, NASA Technical Report 287

Ferraz, A.S.F.S., 2014, "Efeito da distribuição granulométrica de partículas sólidas e de polímeros aniônicos na formação da torta de filtração e no volume de filtrado", thesis, Federeal University Rural of Rio de Janeiro, Seropédica/RJ

Ferreira, V.H.S., 2019, Key Parameters on the flow of polymer solutions through porous medium – experimental and modeling studies, Mechanical and Geoscience Department, Statal University of Campinas, Brazil

Ferreira, C. D., 2010, "Novo Método para Estimativa do Gradiente de Fratura Para Poços de Petróleo", Department of Science and Petroleum Engineering, University of Rio Grande do Norte, Natal

Ferreira, A.S., Massarani, G., 2005, Physico-mathematical modeling of crossflow filtration, Chemical Engineering Journal, v. 111, p. 199-204, Doi: 10.1016/j.cej.2005.02.002

García-Ochoa, F., Santos, V.E., Casa, J.A., Gómez, E., 2000, Xanthan Gum: production, recovery, and properties, Biotechnology Advances, v. 18, p. 549-579, Doi: 10.1016/S0734-9750(00)00050-1

Garing, C., Voltolini, M., Ajo-Franklin, J.B., Benson, S.M., 2017, Pores-scale Evolution of trapped CO2 at early stages following imbibition using micro-CT imaging, Energy Procedia, v. 114, p. 4872-4878, Doi: 10.1016/j.egypro.2017.03.1628

Geankoplis, C.J., 1993, Transport Process and Unit Operations, third edition, PTR Prentice Hall, USA

Georgiousdakis, M., Plevris, V., A Comparative Study of Differential Evolution Variants in Constrained Structural Optimization, Frontiers in Bult Environment, v. 6, Doi: 10.3389/fbuil.2020.00102

Goldemberg, J., Schaeffer, R., Szklo, A., Lucchesi, R., 2014, Energy Policy, v. 64, p. 58-70, Doi: 10.1016/j.enpol.2013.05.064

Guo, C., Wang, X., Wang, H., He, S., Liu, H., Zhu, P., 2018, Effect of pore structure on displacement efficiency and oil-cluster morphology by using micro computed tomography (μCT) technique, Fuel, v. 230, p. 430-439, Doi: 10.1016./j.fuel.2018.05.058

Huang, H., Ayoub, J., 2006, Applicability of the Forchheimer Equation for Non-Darcy Flow in Porous Media, Annual Technical Conference and Exhibition of the Society of Petroleum Engineers, San Antonio, USA

Huh, C., Lange, E.A., Cannella, W.J., 1990, Polymer Retention in Porous Media, SPE/DOE Seventh Symposium on Enhanced Oil Recovery, Oklahoma, USA

International Energy Agency, 2020, iea.org, access on 10/2020

Iscan, A.G., Civan, F., Kok, M.V., 2007, Alteration of permeability by drilling fluid invasion and flow reserval, Journal of Petroleum Science and Engineering, v. 58, p. 227-244, Doi: 10.1016/j.petrol.2007.01.002

Ketcham, R.A., Carlson, W.D., 2001, Acquisition, optimization and interpretation of X-ray computed tomographic imagery: applications to the geosciences, Computers & Geosciences, v. 27, p. 381-400, Doi: 10.1016/S0098-3004(00)00116-3

Khishvand, M., Akbarabadi, M., Piri, M., 2016, Micro-scale experimental investigation of the effect of flow rate on trapping in sandstone and carbonate rock samples, Advances in Water Resources, Doi: 10.1016/j.advwatres.2016.05.012

Kundu, P., Kumar, V., Mishra, I.M., 2016, Experimental and numerical investigations of fluid flow hydrodynamics in porous media: Characterization of Dracy and non-Darcy flow regimes, Powder Technology, Doi: 10.1016/j.potec.2016.09.037

Li, S.; George, J.; Purdy, C., 2012, Pore-Pressure and Wellbore-Stability Prediction to Increase Drilling Efficiency, Journal of Petroleum Technology. p. 98-101, 2012 Doi: 10.2118/144717-JPT

Liu, X., Civan, F., 1995, Formation Damage by Fines Migration Including Effects of Filter Cake, Pore Compressibility, and Non-Darcy Flow – A Modeling Approach to Scaling From Core to Field, SPE International Symposium on Oilfield Chemistry, Texas, USA

Machado, A.C., Teles, A.P., Pepin, A., Bize-Forest, N., Lima, I., Lopes, R.T., 2016, Porous media investigation before and after hydrochloric acid injection on a pre-salt carbonate coquinas samples, Applied Radiation and Isotopes, v. 110, p. 160-163, Doi: 10.1016/j.apradiso.2016.01.005

Machado, J.C.V, 2002, “Reologia e escoamento de fluidos: ênfase na indústria do petróleo”, first edition, Interciência

Madlener, K., Frey, B., Ciezki, H.K., 2009, Generalized Reynolds Number For Non-Newtonian Fluids, Progress in Propulsion Physics, p. 237-250, Doi: 10.1051/eucass/200901237

Magioni, A.Q., 2015, “Determinação de propriedades de tortas de filtração sólido-líquido em altas pressões“, thesis, Federal University of Uberlândia, Uberlândia/MG

Manichand, R.N., Seright, R.S., 2014, Field vs. Laboratory Polymer-Retention Values for a Polymer Flood in the Tambaredjo Field, SPE Improved Oil Recovery Symposium, Tulsa, USA

Massarani, G., 2002, “Fluidodinâmica em Sistemas Particulados”, 2 ed., Rio de Janeiro, E-Papers Serviços Editoriais

Melo, O.K. C., 2008, “Avaliação e Modelagem Reológica de Fluidos de Perfuração Base Água”, Federal University of Rio Grande do Norte, Natal/ RN

Metzner, A.B., Reed, J.C., 1955, Flow of Non-Newtonian Fluids – Correlation of the Laminar, Transition, and Turbulent-flow Regions, A.I.Ch.E Journal, p. 434-440, Doi: 10.1002/aic.690010409

Moreira, B.A., 2014, “Estudo da sedimentação em suspensões de fluidos com características reológicas pseudolásticas“, dissertation, Federal University of Uberlândia, Uberlândia/MG

Muñoz, B., García-Verdugo, J., San-Martín, E., 2015, Quantifying the geopolitical dimension of energy risks, A tool for energy modeling and planning, Energy, p. 1-22, Doi: 10.1016/j.energy.2015.01.058

Nguyen, V.H., Sheppard, A.P., Knackstedt, M.A., Pinczewski, W.V., 2006, The effect of displacement rate on imbibition relative permeability and residual saturation, Journal of Petroleum Science and Engineering, v. 52, p. 54-70, Doi: 10.1016/j.petrol.2006.03.020

Ni, L., 2001, Modelling and Simulation of Cake Formation in Cake Filtration Process, dissertation, University of New South Wales

Oliveira Junior, H., 2014, “Cálculo da tensão nos sólidos para o espessamento e filtração de carbonato de cálcio em suspensões de fluidos newtonianos e pseudoplásticos”, thesis, Federal University of Uberlândia, Uberlândia/MG

Perry, R.H., Green, D.W., Maloney, J.O., 1997, Peery’s Chemical Engineers’ Handbook, 7th edition, McGraw-Hill

Petri, D.F.S., Queiroz, J.C., 2010, Identification of lift-off mechanism failure for salt drill-in drilling fluid containing polymer filter cake through adsorption/desorption studies, v. 70, p. 89-98, Doi: 10.1016/j.petrol.2009.10.002

Petrobras, 2011, “Manual de fluidos”. Ed. Petrobras, Rio de Janeiro

Qin, Z., Arshadi, M., Piri, M., 2019, Micro-scale experimental investigations of multiphase flow in oil-wet carbonates. I. In situ wettability and low-salinity waterflooding, Fuel, v. 257, 116014, DOI: 10.1016/j.fuel.2019.116014

Ramézani, H., Akkal, R., Cohaut, N., Khodja, M., Ahmed-Zaid, T., Bergaya, F., 2015, On the filtrate drilling fluid formation and near well-bore damage along the petroleum well, Journal of Petroleum Science and Engineering, v. 135, p. 299-313, Doi: 10.1016/j.petrol.2015.09.022

Richardson, J.F., Harker, J.H., 2002, Chemical Engineering – Particle Technology and Separation Process, v. 2, fifth edition, Butterworth Heinemann

Roopa, B.S., Bhattacharya, S., 2009, Characterization and modeling of time-independent and time-dependent flow behavior of sodium alginate dispersions, International Journal of Food Science & Technology, v. 44, p. 2583-2589, Doi: 10.1111/j.1365-2621.2009.02088.x

Rosa, A. J.; Carvalho, R. S; Xavier, J. A. D., 2006, "Engenharia de Reservatórios de Petróleo", 1 ed., Rio de Janeiro, Ed. Interciência

Rücker, M., Berg, S., Armstrong, R.T., Georgiadis, A., Ott, H., Schwing, A., Neiteler, R., Brussee, N., Makurat, A., Leu, L., Wolf, M., Khan, F., Enzmann, F., Kersten, M., 2015, From connected pathway flow to ganglion dynamics, Geophysical Research Letters, p. 3888-3894, Doi: 10.1002/2015GL064007

Salehi, S., Ghalambor, A., Saleh, F.K., Jabbari, H., Hussmann, S., 2015, Study of Filtrate and Mud Cake Charcterization in HTHP: Implications for Formation Damage Control, SPE European Formation Damage Conference and Exhibition, Budapest, Hungary

Santos, N.B.C, Zolfaghari, A., Damasceno, J.J.R., Arouca, F.O., Negahban, S., Dahaghi, A.K., 2021, V. 207, 109269, Doi: 10.1016/j.petrol.2021.109269

Santos, N.B.C., Fagundes, F.M., Arouca, F.O., Damasceno, J.J.R., 2018, Sedimentation of solids in drilling fluids used in oil well drilling operations, Journal of Petroleum Science and Engineering, v. 162, p. 137-142, Doi: 10.1016/j.petrol.2017.12.026

Sazali, R.A., Roslan, M.S., Jarrahian, K., 2019, Adsorption study of acrylamide-tertiary-butyl sulfonate (ATBS)/ acrylamide copolymer in polymer flooding enhanced oil recovery (EOR) process, Journal of Physics: Conference Series, v. 1349, Doi: 10.1088/1742-6596/1349/1/012125

Schroeder, C., Torres-Verdín, 2019, Experimental Investigation of Mud-Filtrate Invasion Using Rapid Micro-CT Imaging, SPWLA 60th Annual Logging Symposium, Texas, USA, Doi: 10.30632/T60ALS-2019_EEEEE

Schön, J.H., 2011, Physical properties of rocks- a workbook, Handbook of Petroleum Exploration and Production, Elsevier

Shamsi, F., Norouzi-Apourvari, S., Jafari, S., 209, Image-based simulation of formation damage during suspension injection in homogeneous and heterogeneous porous media: The impact of pore-scale characteristics on macroscopic properties, Journal of Petroleum Science and Engineering, Doi: 10.1016/j.petrol.2019.106786

Silva, T., Massarani, G., 1979, "Escoamento de Fluidos Não Newtonianos em Sistemas Particulados", Revista Brasileira de Física, v. 9, p. 535-547

Simpson, J.P., 1974, Drilling fluid filtration under stimulated downhole conditions

Singh, K., Bultreys, T., Raeini, A.Q., Shams, M., Blunt, M.J., 2019, Imbibition in porous media: correlations of displacement events with pore-throat geometry and the identification of a new type of pore snap-off, EarthArXiv, Doi: 10.31223/osf.io/62gfr

Skalle, P., 2011, Drilling Fluid Engineering, forth edition

Skjetne, E., 1995, High-velocity flow in porous media, dissertation, Norwegian University of Science and Technology

Sochi, T., 2010, Non-Newtonian flow in porous media, Polymer, v. 51, p. 5007-5023, Doi: 10.1016/j.polymer.2010.07.047

Sorbie, K.S., 1991, Polymer-Improved Oil Recovery, first edition, Springer Science+Business Media, LLC

Souza, G., Souto, H.P.A., 2015, "Comparação dos modelos de Darcy, Forchheimer e Barree e Conway na simulação de reservatórios de gás", REUCP, v.9, p. 54-59, ISSN 2318-0692

Storn, R., Price, K., 1995, Differential Evolution: A Simple and Efficient Adaptive Scheme for Global Optimization over Continuous Spaces, International Computer Science Institute, v. 12, p. 1-16

Storn, R., Price, K., Lampinen, J.A., 2005, Diferential Evolution – A Practical Approach to Global Optimization, Springer – Natural Computing Series

Takhanov, D., 2011, Forchheimer Model for Non-Darcy Flow in Porous Media and Fractures, Department of Earth Science and Engineering, Imperial College London

Tarantino, A., Mancuso, C., 2005, Unsaturated Soils: Advances in Testing, Modeling, and Engineering Applications, A.A. Balkema Publishers

Teles, A.P., Lima, I, Lopes, R.T., 2016, Rock porosity quantification by dual-energy X-ray computed microtomography, Micron, v. 86, p. 72-78, Doi: 10.1016/j.micron.2016.02.004

Thomas, J. E., 2001, "Fundamentos da Engenharia de Petróleo", 2 ed., Rio de Janeiro, Ed. Interciência

Valentín, M.B., Bom, C.R., Compan, A.L.M., Correia, M.D., Jesus, C.M., Souza, A.L., Albuquerque, M.P., Albuquerque, M.P., Faria, E.L., 2018, Estimation of permeability and effective porosity logs using deep autoencoders in borehole image logs from the brazillian pre-salt carbonate, Journal of Petroleum Science and Engineering, Doi: 10.1016/j.petrol.2018.06.038

Vanderplaats, G. N., 2001, “Numerical Optimization Techniques for Engineering Design, Vanderplaats Research and Development, 3rd edition, 449 pages, ISBN-13: 978-0944956014

Zang, P., Lee, Y.I., Zhang, J., 2019, A review of high-resolution X-ray computed tomography applied to petroleum geology and a case study, Micron, v. 124, Doi: 10.1016/j.micron.2019.102702

Zang, G., Seright, R.S., 2015, Hydrodynamic Retention and Rheology of EOR Polymers in Porous Media, SPE Annual Technical Conference and Exhibition, The Woodlands, USA

Zhao, X., Qiu, Z., Sun, B., Liu, S., Xing, X., Wang, M., 2019, Formation damage mechanisms associated with drilling and completion fluids for deepwater reservoirs, Journal of Petroleum Science and Engineering, v. 173, p. 112-121, Doi: 10.1016/j.petrol.2018.09.098

Zolfaghari, A., Piri, M., 2017a, Pore-Scale Network Modeling of Three-Phase Flow Based on Thermodynamically Consistent Threshold Capillary Pressures. I. Cusp Formation and Collapse, Transport in Porous Media, v. 116, p. 1093-1137, Doi: 10.1007/s11242-016-0814-8

Waldmann, A. T. A., 2005, “Mecanismos que governam a efetividade de agentes obturantes no controle da invasão de fluidos de perfuração na rocha reservatório de petróleo”, thesis, PUC-RIO, Rio de Janeiro/RJ

Appendix

A.1

The following setups were applied to solve the inverse optimization problem through the Differential Evolution algorithm:

(i) Domain of the function: $0 \leq K_c \leq 1$ m^2 and $0 \leq K_m \leq 1$ m^2;

(ii) Parameters of the Differential Evolution algorithm (Storn et al., 2005): 25 individuals in the population, 500 generations; disturbance rate and crossover probability equal to 0.8. For this dataset, the total number of evaluations of the objective function was 25+25x500;

(iii) The algorithm used random seeds to start the random number generator, and it was performed 10 times to obtain the average values of permeability and standard deviation;

(iv) Integration method: Runge-Kutta-Fehlberg (Fehlberg, 1968);

(v) The external Penalty Method (Vanderplaats, 2001) was used to handle the inequality constraints of the optimization problem.

A.2

Table A.1: Reynolds number (Re_i).

	Re_i							
Pressure	XG 0.2_50 µm		XG 0.2_120 µm		XG 0.4_50 µm		XG 0.4_120 µm	
x10^5 [Pa]	Darcy	Forchheimer	Darcy	Forchheimer	Darcy	Forchheimer	Darcy	Forchheimer
2	0.25	0.24	2.70	2.18	0.009	0.009	1.51	1.18
4	1.34	1.09	9.10	6.73	0.48	0.42	3.95	3.01
6	2.89	2.07	17.99	12.52	1.37	1.03	9.74	6.88
8	4.27	3.08	25.25	17.59	2.58	1.75	19.67	12.04
10	7.07	4.56	39.61	26.92	4.58	2.78	28.92	17.13
12	9.98	6.18	51.06	32.87	6.10	3.51	37.48	21.77
14	12.20	7.21	62.77	40.79	8.79	4.54	46.22	26.98

Table A.2: Reynolds number (Re_k).

	Re_k							
Pressure	XG 0.2_50 µm		XG 0.2_120 µm		XG 0.4_50 µm		XG 0.4_120 µm	
x10^5 [Pa]	Darcy	Forchheimer	Darcy	Forchheimer	Darcy	Forchheimer	Darcy	Forchheimer
2	0.001	0.001	0.001	0.001	0.00003	0.00003	0.002	0.002
4	0.003	0.003	0.003	0.004	0.001	0.001	0.003	0.004
6	0.005	0.005	0.005	0.008	0.003	0.003	0.006	0.006
8	0.006	0.006	0.006	0.009	0.004	0.005	0.009	0.010
10	0.008	0.008	0.008	0.013	0.006	0.007	0.011	0.013
12	0.010	0.010	0.010	0.015	0.008	0.009	0.013	0.015
14	0.012	0.012	0.012	0.017	0.010	0.011	0.014	0.016

Table A.3: Reynolds number (Re_{gen}).

	Re_{gen}			
Pressure x10^5 [Pa]	XG 0.2_50 µm	XG 0.2_120 µm	XG 0.4_50 µm	XG 0.4_120 µm
2	0.013	0.053	0.00034	0.023
4	0.053	0.126	0.016	0.045
6	0.100	0.204	0.038	0.078
8	0.128	0.265	0.062	0.134
10	0.187	0.350	0.092	0.174
12	0.235	0.438	0.114	0.208
14	0.282	0.495	0.147	0.236

A.3

Table A.4: Thickness and porosity of the external cake of XG 0.2 and 0.4% (m/m) through the membranes of 50 and 120 µm.

ΔP (x10^5) [Pa]	l_c [mm]				ε_c [-]			
	XG 0.2 50 µm	XG 0.2 120µm	XG 0.4 50 µm	XG 0.4 120 µm	XG 0.2 50 µm	XG 0.2 120 µm	XG 0.4 50 µm	XG 0.4 120 µm
2	2.4 ± 0.3	1.9 ± 0.7	2.7 ± 0.3	2.2 ± 0.6	0.72 ± 0.05	0.73 ± 0.2	0.8 ± 0.1	0.88 ± 0.01
4	3.1 ± 0.2	1.9 ± 0.3	2.2 ± 0.3	2.2 ± 0.3	0.62 ± 0.05	0.697 ± 0.002	0.75 ± 0.01	0.85 ± 0.01
6	3.21 ± 0.05	2.0 ± 0.3	2.5 ± 0.2	2.3 ± 0.2	0.57 ± 0.04	0.705 ± 0.007	0.7 ± 0.0	0.84 ± 0.02
8	3.83 ± 0.06	2.1 ± 0.3	2.7 ± 0.1	3.1 ± 0.3	0.61 ± 0.02	0.69 ± 0.02	0.76 ± 0.03	0.845 ± 0.007
10	3.6 ± 0.3	2.22 ± 0.08	2.8 ± 0.5	2.2 ± 0.7	0.59 ± 0.03	0.657 ± 0.002	0.69 ± 0.08	0.83 ± 0.03
12	3.3 ± 0.2	1.80 ± 0.09	2.9 ± 0.6	2.2 ± 0.5	0.558 ± 0.007	0.71 ± 0.3	0.72 ± 0.07	0.759 ± 0.001
14	3.8 ± 0.3	2.38 ± 0.06	3.3 ± 0.2	3.1 ± 0.7	0.56 ± 0.04	0.657 ± 0.009	0.68 ± 0.06	0.82 ± 0.04

Table A.5: Specific mass of the filtrate of XG 0.2 and 0.4% (m/m) and $CaCO_3$ through the membranes of 50 and 120 µm.

ΔP	ρ_{fil} (x10^3) [Kgm^3]			
(x10^5) [Pa]	XG 0.2_ 50 µm	XG 0.2_120µm	XG 0.4_50 µm	XG 0.4_120 µm
2	1.08 ± 0.07	1.03 ± 0.03	1.09 ± 0.05	0.97 ± 0.05
4	1.067 ± 0.006	1.037 ± 0.009	1.11 ± 0.04	1.03 ± 0.03
6	1.08 ± 0.05	1.06 ± 0.03	1.12 ± 0.03	1.04 ± 0.05
8	1.051 ± 0.007	1.05 ± 0.04	1.07 ± 0.08	1.00 ± 0.04
10	1.06 ± 0.02	1.03 ± 0.04	1.07 ± 0.04	1.02 ± 0.04
12	1.047 ± 0.003	1.1 ± 0.1	1.08 ± 0.04	0.97 ± 0.07
14	1.04 ± 0.01	1.02 ± 0.06	1.07 ± 0.01	1.01 ± 0.05

Table A.6: Experimental and estimated filtrate volume, medium and cake permeabilities, and objective function of XG 0.2% (m/m) and $CaCO_3$ through the membranes of 50 and 120 µm.

ΔP (x10^5) [Pa]	t [s]	XG 0.2% [m/m]							
		50 µm				120 µm			
		V (x10^{-5}) [m^6]	K_m (x10^{-15}) [m^2]	K_c (x10^{-15}) [m^2]	OF (x10^{-14}) [m^6]	V (x10^{-5}) [m^3]	K_m (x10^{-15}) [m^2]	K_c (x10^{-15}) [m^2]	OF (x10^{-14}) [m^6]
2	60	0.34	8.04	1.23	2.19	0.60	8.81	2.17	11.1
	300	0.77				0.92			
	600	1.07				1.19			
	900	1.28				1.36			
	1200	1.43				1.54			
	1500	1.55				1.68			
	1800	1.66				1.83			
4	60	0.83	4.91	1.04	4.69	0.52	2.89	1.20	12.6
	300	1.75				0.85			
	600	2.35				1.15			
	900	2.79				1.43			
	1200	3.12				1.66			
	1500	3.41				1.82			
	1800	3.67				1.97			
6	60	0.907	2.49	0.76	2.96	0.43	1.51	0.50	1.77
	300	1.95				0.83			
	600	2.69				1.16			
	900	3.21				1.41			
	1200	3.63				1.63			
	1500	3.99				1.82			
	1800	4.30				1.98			
8	60	1.08	2.11	0.55	19.1	0.48	1.10	0.32	3.70
	300	2.13				0.91			
	600	2.85				1.26			
	900	3.37				1.55			
	1200	3.80				1.76			
	1500	4.18				1.93			
	1800	4.5				2.10			
10	60	1.07	1.72	0.42	69.5	0.45	0.70	0.22	14.1
	300	2.21				0.92			
	600	2.91				1.30			
	900	3.47				1.59			
	1200	3.95				1.88			
	1500	4.35				2.05			
	1800	4.70				2.23			
12	60	1.06	0.97	0.30	41.2	0.62	0.65	0.22	5.37
	300	2.24				1.13			
	600	3.04				1.84			
	900	3.64				2.10			
	1200	4.15				2.33			
	1500	4.59				1.52			
	1800	4.97				2.51			
14	60	1.49	0.97	0.30	824	0.68	0.47	0.16	0.61
	300	2.86				1.21			
	600	3.85				1.67			
	900	4.55				2.01			
	1200	5.13				2.29			
	1500	5.64				2.54			
	1800	6.11				2.75			

Table A.7: Experimental and estimated filtrate volume, medium and cake permeabilities, and objective function of XG 0.4% (m/m) and $CaCO_3$ through the membranes of 50 and 120 µm.

		XG 0.4% [m/m]							
		50 µm				120 µm			
ΔP (x10^5) [Pa]	t [s]	V (x10^{-5}) [m^3]	K_m (x10^{-15}) [m^2]	K_c (x10^{-15}) [m^2]	OF (x10^{-14}) [m^6]	V (x10^{-5}) [m^3]	K_m (x10^{-15}) [m^2]	K_c (x10^{-15}) [m^2]	OF x(10^{-14}) [m^6]
2	60	0.57	64.5	9.15	16.8	0.75	63.9	16.2	9.85
	300	0.97				0.91			
	600	1.21				0.99			
	900	1.33				1.08			
	1200	1.44				1.15			
	1500	1.50				1.21			
	1800	1.54				1.28			
4	60	0.69	21.8	4.40	6.34	0.71	20.9	2.47	1.28
	300	1.22				0.90			
	600	1.53				1.04			
	900	1.70				1.13			
	1200	1.85				1.20			
	1500	1.95				1.27			
	1800	2.03				1.33			
6	60	0.74	10.3	1.68	15.9	0.7	11.5	2.47	4.89
	300	1.32				0.89			
	600	1.66				1.03			
	900	1.84				1.13			
	1200	1.98				1.22			
	1500	2.08				1.29			
	1800	2.16				1.35			
8	60	0.65	7.16	1.68	102	0.74	6.44	2.47	13.4
	300	1.25				0.96			
	600	1.61				1.11			
	900	1.85				1.25			
	1200	2.01				1.37			
	1500	2.17				1.47			
	1800	2.29				1.55			
10	60	0.80	4.34	1.27	2.36	0.81	4.56	2.37	8.79
	300	1.51				1.05			
	600	1.93				1.23			
	900	2.22				1.36			
	1200	2.42				1.49			
	1500	2.60				1.61			
	1800	2.73				1.7			
12	60	0.91	4.02	1.27	191	0.85	2.82	1.06	20.7
	300	1.73				1.14			
	600	2.24				1.35			
	900	2.57				1.49			
	1200	2.82				1.63			
	1500	3.04				1.77			
	1800	3.23				1.89			
14	60	1.10	3.31	1.27	2.86	1.28	2.81	1.06	2100
	300	2.03				1.60			
	600	2.58				1.82			
	900	2.95				1.96			
	1200	3.23				2.10			
	1500	3.46				2.21			
	1800	3.66				2.32			